National Library of Canada
Canadian Theses Service
Ottawa, Canada
K1A 0N4

Bibliothèque nationale du Canada
Services des thèses canadiennes

CANADIAN THESES

THÈSES CANADIENNES

NOTICE

The quality of this microfiche is heavily dependent upon the quality of the original thesis submitted for microfilming. Every effort has been made to ensure the highest quality of reproduction possible.

If pages are missing, contact the university which granted the degree.

Some pages may have indistinct print especially if the original pages were typed with a poor typewriter ribbon or if the university sent us an inferior photocopy.

Previously copyrighted materials (journal articles, published tests, etc.) are not filmed.

Reproduction in full or in part of this film is governed by the Canadian Copyright Act, R.S.C. 1970, c. C-30. Please read the authorization forms which accompany this thesis.

AVIS

La qualité de cette microfiche dépend grandement de la qualité de la thèse soumise au microfilmage. Nous avons tout fait pour assurer une qualité supérieure de reproduction.

S'il manque des pages, veuillez communiquer avec l'université qui a conféré le grade.

La qualité d'impression de certaines pages peut laisser à désirer, surtout si les pages originales ont été dactylographiées à l'aide d'un ruban usé ou si l'université nous a fait parvenir une photocopie de qualité inférieure.

Les documents qui font déjà l'objet d'un droit d'auteur (articles de revue, examens publiés, etc.) ne sont pas microfilmés.

La reproduction, même partielle, de ce microfilm est soumise à la Loi canadienne sur le droit d'auteur, SRC 1970, c. C-30. Veuillez prendre connaissance des formules d'autorisation qui accompagnent cette thèse.

THIS DISSERTATION
HAS BEEN MICROFILMED
EXACTLY AS RECEIVED

LA THÈSE A ÉTÉ
MICROFILMÉE TELLE QUE
NOUS L'AVONS REÇUE

NL 339 (r. 86/01)

Canada

245

0-315-26976-6

National Library of Canada | Bibliothèque nationale du Canada

Canadian Theses Division | Division des thèses canadiennes

Ottawa, Canada
K1A 0N4

PERMISSION TO MICROFILM — AUTORISATION DE MICROFILMER

- Please print or type — Écrire en lettres moulées ou dactylographier

Full Name of Author — Nom complet de l'auteur
REYAD ILAYAN TAWFIQ SAWAFTA

Date of Birth — Date de naissance
23-5-1958

Country of Birth — Lieu de naissance
JORDAN

Permanent Address — Résidence fixe
ZAHRET NABLUS SWEETS
AL-HASHIMI STREET
IRBID - JORDAN

Title of Thesis — Titre de la thèse
COMPARISON OF CONVENTIONAL AND UNCONVENTIONAL POTENTIAL MODELS FOR PROTON INELASTIC SCATTERING

University — Université
UNIV. OF ALBERTA

Degree for which thesis was presented — Grade pour lequel cette thèse fut présentée
Master of Science

Year this degree conferred — Année d'obtention de ce grade
1984

Name of Supervisor — Nom du directeur de thèse
Helmy Sherif

Permission is hereby granted to the NATIONAL LIBRARY OF CANADA to microfilm this thesis and to lend or sell copies of the film.

The author reserves other publication rights, and neither the thesis nor extensive extracts from it may be printed or otherwise reproduced without the author's written permission.

L'autorisation est, par la présente, accordée à la BIBLIOTHÈQUE NATIONALE DU CANADA de microfilmer cette thèse et de prêter ou de vendre des exemplaires du film.

L'auteur se réserve les autres droits de publication; ni la thèse ni de longs extraits de celle-ci ne doivent être imprimés ou autrement reproduits sans l'autorisation écrite de l'auteur.

Date
7th, Nov., 1983

Signature
R. Sawafta

NL-91 (4/77)

THE UNIVERSITY OF ALBERTA

COMPARISON OF CONVENTIONAL AND UNCONVENTIONAL POTENTIAL MODELS FOR PROTON INELASTIC SCATTERING

by

© Reyad Ilayan Tawfiq Sawafta

A THESIS
SUBMITTED TO THE FACULTY OF GRADUATE STUDIES AND RESEARCH
IN PARTIAL FULFILMENT OF THE REQUIREMENTS FOR THE DEGREE
OF MASTER OF SCIENCE

DEPARTMENT OF PHYSICS

EDMONTON, ALBERTA
SPRING 1984

THE UNIVERSITY OF ALBERTA

RELEASE FORM

NAME OF AUTHOR Reyad Ilayan Tawfiq Sawafta

TITLE OF THESIS COMPARISON OF CONVENTIONAL AND UNCONVENTIONAL POTENTIAL MODELS FOR PROTON INELASTIC SCATTERING

DEGREE FOR WHICH THESIS WAS PRESENTED: MASTER OF SCIENCE

YEAR THIS DEGREE GRANTED: SPRING 1984

Permission is hereby granted to THE UNIVERSITY OF ALBERTA LIBRARY to reproduce single copies of this thesis and to lend or sell such copies for private, scholarly or scientific research purposes only.

The author reserves other publication rights, and neither the thesis nor extensive extracts from it may be printed or otherwise reproduced without the author's written permission.

(SIGNED) R. Sawafta

PERMANENT ADDRESS:

Zahret Nablus Sweets
AL-Hashimi Street
Irbid - Jordan

DATED 27th, October, 1983

THE UNIVERSITY OF ALBERTA

FACULTY OF GRADUATE STUDIES AND RESEARCH

The undersigned certify that they have read, and recommend to the Faculty of Graduate Studies and Research, for acceptance, a thesis entitled COMPARISON OF CONVENTIONAL AND UNCONVENTIONAL POTENTIAL MODELS FOR PROTON INELASTIC SCATTERING submitted by Reyad Ilayan Tawfiq Sawafta in partial fulfilment of the requirements for the degree of MASTER OF SCIENCE.

Helmy S. Sherif
Supervisor

P. Kitching

M. Razavy

Date 27th October 1983

THIS WORK IS DEDICATED TO

MY PARENTS

ABSTRACT

This thesis is a theoretical study of conventional and unconventional potential models for proton inelastic scattering. The unconventional potential results from a reduction of the Dirac equation, with scalar and vector complex nuclear potentials, to a Schrödinger-type equation. At intermediate energies the potential is found to have an unconventional shape, namely the Wine Bottle Shape. This potential is generalized to an extended optical potential appropriate for a treatment of inelastic excitations of collective states. The generalized potential is found to have a deformed spin dependent interaction of the full Thomas form. Comparisons are made between predictions for inelastic scattering observables calculated using this potential and those based on a non-relativistic Schrödinger equation based optical potential of the Standard form. Results of these comparisons for both cross-section and analyzing power will be discussed.

The effects of using the deformed spin-orbit interactions, the deformed Coulomb interaction, relativistic versus non-relativistic kinematics and equal deformation parameters (β) versus equal deformation lengths (βR) are investigated.

The main conclusion of this work is that the unconventional potential (Dirac model) predictions for proton inelastic scattering cross-section and polarization, for some low-lying collective states, are either comparable or superior to those of the conventional potential (Standard model). We have found that the deformation length βR, determined from a comparison of experimental and calculated cross-sections, decreases with increasing projectile energy.

ACKNOWLEDGEMENTS

I would like to express my gratitude and appreciation to my supervisor Dr. Helmy Sherif for not only suggesting this project but also for helping in every possible way throughout the course of this work. Thanks to Helmy for being so patient with me especially during the early stages of this work, where he did not only teach me physics, but also shared with me his computer knowledge.

I am also grateful to E.D. Cooper and J. Johanson for their assistance through their cooperation by giving me their unpublished optical model parameters to do the relativistic calculations.

I would also like to thank my fellow graduate students; M. London, G. Lotz, K. Michaelian and J. Thekkumthala for sharing their time and knowledge with me. Special thanks also to summer student J. Bowman for providing a computer program to plot the figures.

I would also like to thank the University of Alberta for their financial support during the course of this work.

Special thanks also to my friends O. Othman, H. El-Sharkawi and their families for their encouragement and support.

Last, but by no means least, I would like to thank Ms. G. Jolicoeur for undertaking the typing of this thesis.

Table of Contents

Chapter Page

I. INTRODUCTION.. 1

II. THE OPTICAL POTENTIAL MODEL.. 4

1. Formal Theory of the Optical Potential Model........... 4

2. The Phenomenological Optical Model..................... 8

III. THE NON-RELATIVISTIC EXTENDED OPTICAL MODEL (THE STANDARD MODEL).. 12

IV. DIRAC PHENOMENOLOGY FOR PROTON ELASTIC SCATTERING........... 24

V. RELATIVISTIC INELASTIC SCATTERING (THE DIRAC MODEL)......... 30

VI. ELASTIC SCATTERING FITS... 37

1. ^{12}C... 40

2. ^{24}Mg.. 40

3. ^{40}Ca.. 45

4. Potential Equivalence...................................... 45

VII. INELASTIC SCATTERING... 53

1. The Effect of Using Equal Deformation Length............ 63

2. The Effect of Kinematics................................ 63

3. The Effect of Coulomb Deformation....................... 68

4. ^{12}C(p,p')^{12}C* 2^+ State (Ex = 4.43 MeV) at Ep = 200 MeV..... 68

5. ^{24}Mg(p,p')^{24}Mg* 2^+ State (Ex = 1.37 MeV) at Ep = 155 MeV... 68

6. ^{32}S(p,p')^{32}S* 2^+ State (Ex = 2.24 MeV) at Ep = 155 MeV..... 69

7. ^{40}Ca(p,p')^{40}Ca* 3^- State (Ex = 3.73 MeV) at Ep = 181 MeV.... 69

8. ^{40}Ca(p,p')^{40}Ca* 2^+ State (Ex = 18 MeV) at 181 MeV.......... 74

9. ^{40}Ca(p,p')^{40}Ca* 3^- State (Ex = 3.73 MeV) at Ep = 300 MeV.... 77

10. ^{40}Ca(p,p')^{40}Ca* 3^- State (Ex = 3.73 MeV) at Ep = 500 MeV.... 77

11. ^{208}Pb(p,p')^{208}Pb* 3^- State (Ex = 2.61 MeV) at Ep = 200 MeV... 77

VIII. CONCLUSION.. 91

REFERENCES.. 93

LIST OF FIGURES

Figure 1 Coordinate system.

Figure 2 Cross-section for $P + {}^{12}c$ elastic scattering at Ep = 200 MeV.

Figure 3 Polarization for $P + {}^{12}c$ elastic scattering at Ep = 200 MeV.

Figure 4 Cross-section for $P + {}^{24}Mg$ elastic scattering at Ep = 155 MeV.

Figure 5 Polarization for $P + {}^{24}Mg$ elastic scattering at Ep = 155 MeV.

Figure 6 Cross-section for $P + {}^{40}Ca$ elastic scattering at Ep = 181 MeV.

Figure 7 Polarization for $P + {}^{40}Ca$ elastic scattering at Ep = 181 MeV.

Figure 8 The real part of the central potential for $P + {}^{40}Ca$ at Ep = 181 MeV.

Figure 9 The imaginary part of the central potentail for $P + {}^{40}Ca$ at Ep = 181 MeV.

Figure 10 The real part of the spin-orbit potential for $P + {}^{40}Ca$ at Ep = 181 MeV.

Figure 11 The imaginary part of the spin-orbit potential for $P + {}^{40}Ca$ at Ep = 181 MeV.

Figure 12 The real part of the central radial form factor for $P + {}^{40}Ca$ at Ep = 181 MeV.

Figure 13 The imaginary part of the central radial form factor for $P + {}^{40}Ca$ at Ep = 181 MeV.

Figure 14 The real part of spin-robit 1 form factor for $P + {}^{40}Ca$ at Ep = 181 MeV.

Figure 15 The imaginary part of spin-orbit 1 form factor for $P + {}^{40}Ca$ at Ep = 181 MeV.

Figure 16 The real part of spin-oribt 2 form factor for $P + {}^{40}Ca$ at Ep = 181 MeV.

Figure 17 The imaginary part of spin-orbit 2 form factor for $P + {}^{40}Ca$ at Ep = 181 MeV.

Figure 18 The effect of the deformed spin-oribt term on the calculated cross-section, "The Dirac Model".

Figure 19 The effect of the deformed spin-orbit term on the calculated cross-section, "The Standard Model'.

Figure 20 Cross-Section for $P + {}^{12}C$ inelastic scattering (2^+ state; Ex = 4.43 MeV) at Ep = 200 MeV.

Figure 21 Polarization for $P + {}^{12}C$ inelastic scattering (2^+ state; Ex = 4.43 MeV) at Ep = 200 MeV.

Figure 22 Cross-section for $P + {}^{23}Mg$ inelastic scattering (2^+ state; Ex = 1.37 MeV) at Ep = 155 MeV.

Figure 23 Polarization for $P + {}^{24}Mg$ inelastic scattering (2^+ state; Ex = 1.37 MeV) at Ep = 155 MeV.

Figure 24 Cross-section for $P + {}^{32}S$ inelastic scattering (2^+ state; Ex = 2.24 MeV) at Ep = 155 MeV.

Figure 25 Polarization for $P + {}^{32}S$ inelastic scattering (2^+ state; Ex = 2.24 MeV) at Ep = 155 MeV.

Figure 26 Cross-section for $P + {}^{40}Ca$ inelastic scattering (3^- state; Ex = 3.73 MeV) at Ep = 181 MeV.

Figure 27 Polarization for $P + {}^{40}Ca$ inelastic scattering (3^- state; Ex = 3.73 MeV) at Ep = 181 MeV.

Figure 28 Cross-section for $P + {}^{40}Ca$ inelastic scattering (2^+ state; Ex = 18 MeV) at Ep = 181 MeV.

Figure 29 Polarization for $P + {}^{40}$Ca inelastic scattering (2^+ state; ~~Ex = 18 MeV) at Ep = 181 MeV.~~

Figure 30 Cross-section for $P + {}^{40}$Ca inelastic scattering (3^- state; Ex = 3.73 MeV) at Ep = 300 MeV.

Figure 31 Polarization for $P + {}^{40}$Ca inelastic scattering (3^- state; Ex = 3.73 MeV) at Ep = 300 MeV.

Figure 32 Cross-section for $P + {}^{40}$Ca inelastic scattering (3^- state; Ex = 3.73 MeV[at Ep = 500 MeV.

Figure 33 Polarization for $P + {}^{40}$Ca inelastic scattering (3^- state; Ex = 3.73 MeV) at Ep = 500 MeV.

Figure 34 Cross-Section for $P + {}^{208}$Pb inelastic scattering (3^- state; Ex = 2.61 MeV) at Ep = 200 MeV.

Figure 35 Polarization for $P + {}^{208}$Pb inelastic scattering (3^- state; Ex = 2.61 MeV) at Ep = 200 MeV).

Figure 36 The effect of the deformed spin-orbit term on the calculated cross-section for $P + {}^{208}$Pb inelastic scattering (3^- state; Ex = 2.61 MeV) at Ep = 200 MeV.

Figure 37 The effect of the deformed Coulomb potential on the calculated cross-section for $P + {}^{208}$Pb inelastic scattering (3^- state; Ex = 2.61 MeV) at Ep = 200 MeV.

LIST OF TABLES

Table I The standard optical model parameters.

Table II The Dirac optical model parameters for ^{40}Ca at Ep = 181 MeV.

Table III The values of βR for inelastic proton scattering from ^{208}Pb (3^- state; Ex = 2.61 MeV).

Table IV The values of βR for inelastic proton scattering from ^{40}Ca (3^- state; Ex = 3.73 MeV).

I. INTRODUCTION

One of the most important concerns in nuclear physics is to understand the structure of the nucleus as well as the mechanisms of nuclear reactions. In practice one can find the properties of nuclei by appropriate scattering and reaction measurements. However, the interaction of nuclear projectiles with nuclei is a complicated many-body problem. Because of this complexity one often relies on simplified models to describe the phenomena.

One of these phenomenological approaches is the optical model potential based on Schrödinger equation with Woods-Saxon form factors, which seeks to describe the interaction of, say, a nucleon with a target nucleus by means of a complex potential. This model has been successful in describing proton elastic scattering at low energies and few hundred MeV energies. We will call this approach "The Standard Model" throughout this work.

In recent years, another optical model potential based on the Dirac equation has been constructed from a Lorentz scalar term and a time-like Lorentz vector term. It has been found that this model is successful in describing the proton elastic scattering at intermediate energies (Ar81, Ar82, Co81). One of the interesting results of this model is the discovery of the "wine bottle shaped" real central potential. It is found that when one reduces the Dirac potential to "Schrödinger equivalent potentials" that the real central potential turns repulsive in the interior at energies between 100-200 MeV with attraction in the outer region (Ja79, Ja80). It becomes progressively more repulsive as the energy increases. This is in contrast with the standard

Woods-Saxon potentials where the real central potential weakens but remains totally attractive as the energy increases, then turn repulsive at some energy. (In this work, we will call the latter optical model approach "The Dirac Model".)

The parameters of both potentials can be treated completely phenomenologically and thus determined from the data, or the number of free parameters can be reduced by invoking nuclear structure information on charge and matter density.

Both potentials have been generalized to describe the inelastic scattering processes leading to the excitation of collective surface modes of target nuclei. In this generalization the normal spherical potential is extended by including terms that explicitly contain dynamical nuclear coordinates describing the displacement of the nuclear surface. This is usually achieved by letting, $R \rightarrow R + \alpha(\hat{r})$, where R is the radius parameter of a typical spherical optical potential $\alpha(\hat{r})$ is the displacement of the nuclear surface in the direction $\hat{r}$. All parts of the potential are then deformed and expanded in powers of $\alpha(\hat{r})$ and only terms to first order in $\alpha(\hat{r})$ are retained (B164). The calculations of the inelastic scattering cross-section and polarization are done in the framework of the distorted wave Born approximation.

In a recent work Satchler (Sa83) has studied the inelastic cross-section for low-lying collective states in ^{40}Ca and ^{208}Pb for proton energies near 200 MeV. His study was based on extending two spin independent optical potentials, that provide the same elastic scattering cross-section, to describe the inelastic scattering section. One of these potentials is a potential of standard Woods-Saxon shape, while the other is of a wine bottle bottom shape generated through the addition of a derivative term to the potential. Satchler did not include spin-orbit interactions in his analysis of inelastic scattering.

In the present work we will carry out a similar investigation of the consequences of the unconventional shape of the nuclear optical potential at intermediate energies for proton inelastic scattering. Our approach is based on comparing the calculations resulting from both the standard and the Dirac models. Our investigation differs from that of Satchler in one additional respect, namely, that the spin-orbit effects are fully taken into account.

In chapter II, we describe the standard optical potential model for proton elastic scattering. In chapter III, we describe the extended standard optical model for proton inelastic scattering. In chapter IV, we describe the Dirac optical model for proton elastic scattering. In chapter V, we describe the extended Dirac optical model for proton inelastic scattering. In chapter VI, fits to elastic scattering data from both models and comparisons of the conventional and the unconventional potentials will be shown. In chapter VII, theoretical predictions of the present work for inelastic scattering are compared to experimental data, and to Satchler's predictions when possible. A conclusion is given in chapter VIII.

II. THE OPTICAL POTENTIAL MODEL

If a nucleon enters a nuclear field of a target nucleus, it will interact with the target in its path and will be either absorbed or emerge on the other side after some considerable buffeting. At each encounter it may change its direction and spin state, and several such collisions may take place as the incident particle crosses the nucleus. The interaction of a single nucleon with a nucleus is a complicated many-body problem. The optical model replaces the many-body interaction by a complex nucleon-nucleus potential. In optical model phenomenology the potential is written in terms of certain model parameters which are determined from comparison with experimental data. A formal theory is needed to relate these model parameters to the properties of the many-body system.

II.1 Formal Theory of the Optical Model Potential:

We will summarise here the formal theory of the optical model developed by Feshbach (Fe58) as it was described by Jackson (Ja70).

If we consider a nucleon interacting with a nucleus, the total Hamiltonian of the system could be written as

$$H = H_o + H(\xi) + V(\vec{r},\xi) \qquad \text{(II.1)}$$

where H_o is the kinetic energy operator of the relative motion of projectile and target, $H(\xi)$ is the internal Hamiltonian of the target nucleus which has co-ordinates ξ, and V is the interaction potential between the projectile and the target nucleons. The Schrödinger equation we have to solve here is

$$H\Psi(\vec{r},\xi) = E\Psi(\vec{r},\xi) \qquad \text{(II.2)}$$

where $\Psi(\vec{r},\xi)$ is the total wavefunction of the projectile-target system. The target states $\Phi_\lambda(\xi)$ are solutions of the equation

$$H(\xi)\Phi_\lambda(\xi) = \varepsilon_\lambda\Phi_\lambda(\xi) \tag{II.3}$$

where ε_λ is the energy eigen value of the target Hamiltonian $H(\xi)$ which is assumed to be hermetian. The states $\Phi_\lambda(\xi)$ are completely antisymmetric and form a complete orthogonal set with the ground state denoted by $\Phi_o(\xi)$. The total wavefunction Ψ may be written as an expansion in Φ_λ

$$\Psi(\vec{r},\xi) = \sum_\lambda \psi_\lambda(\vec{r})\Phi_\lambda(\xi) \tag{II.4}$$

where $\psi_\lambda(\vec{r})$ describes the motion of the projectile relative to the target.

The elastic channel in the above expansion is represented by $\psi_o(\vec{r})\Phi_o(\xi)$. If we define P as an elastic channel projection operator:

$$P\Psi(\vec{r},\xi) = \psi_o(\vec{r})\Phi_o(\xi). \tag{II.5}$$

and if we introduce another projection operator Q such that it projects out all states except the elastic channel, we have

$$\begin{aligned} P + Q &= 1 \\ P^2 &= P \\ Q^2 &= Q \\ PQ = QP &= 0 \end{aligned} \tag{II.6}$$

then one can write the following

$$\begin{aligned} Q\Psi(\vec{r},\xi) &= (1-P)\Psi(\vec{r},\xi) \\ &= \Psi(\vec{r},\xi) - P\Psi(\vec{r},\xi) \\ &= \Psi(\vec{r},\xi) - \psi_o(\vec{r})\Phi_o(\xi) \quad . \end{aligned} \tag{II.7}$$

We can construct these projection operators as follows

5

$$P = |\Phi_o(\xi)><\Phi_o(\xi)| \qquad \text{(II.8)}$$

and

$$Q = \sum_{\lambda\neq 0} |\Phi_\lambda><\Phi_\lambda| \quad . \qquad \text{(II.9)}$$

Equation (II.2) can now be rewritten as

$$(E - H)(P + Q)\Psi = 0 \qquad \text{(II.10)}$$

if we multiply on the left by P, we get

$$(E - PHP)P\Psi = (PHQ)Q\Psi \qquad \text{(II.11)}$$

on the other hand, multiplication by Q yields

$$(E - QHQ)Q\Psi = (QHP)P\Psi \qquad \text{(II.12)}$$

where we have used the properties of the projection operators as given by equation (II.6). We can rewrite equation (II.12) as follows

$$Q\Psi = \frac{1}{E - QHQ} QHP\ P\Psi \ . \qquad \text{(II.13)}$$

If there are open non-elastic channels it is necessary to replace E-QHQ in equation (II.13) by $E - QHQ + i\varepsilon$, in order to ensure that $Q\Psi$ has only outgoing waves in these channels. If we substitute equation (II.13) into equation (II.11) we get the following equation for $P\Psi$

$$(E - PHP - PHQ\frac{1}{E - QHQ} QHP)P\Psi = 0 \ . \qquad \text{(II.14)}$$

Since we are interested only in elastic scattering we have to reduce equation (II.14) to an equation for $\psi_o(\vec{r})$. This can be done by multiplying from the left by $<\Phi_o|$ and integrating over the target co-ordinate ξ. Then one can write equation (II.14) as follows

$$<\Phi_o|E|P\Psi> - <\Phi_o|PHP|P\Psi> - <\Phi_o|PHQ\frac{1}{E - QHQ} QHP|P\Psi> = 0 \qquad \text{(II.15)}$$

and hence

$$E\psi_o(\vec{r}) - H_o\psi_o(\vec{r}) - \varepsilon_o\psi_o(\vec{r}) - \langle\Phi_o|V(\vec{r},\xi)|\Phi_o\rangle\psi_o(\vec{r})$$

$$- \langle\Phi_o|PHQ\,\frac{1}{E-QHQ}\,QHP|\Phi_o\rangle\psi_o(\vec{r}) = 0 \qquad \text{(II.16)}$$

the last term can be reduced as follows:

$$\begin{aligned}\langle\Phi_o|PHQ &= \sum_{\lambda\neq 0}\langle\Phi_o|PH|\Phi_\lambda\rangle\langle\Phi_\lambda| \\ &= \sum_{\lambda\neq 0}\langle\Phi_o|H_o + H(\xi) + V(\vec{r},\xi)|\Phi_\lambda\rangle\langle\Phi_\lambda| \\ &= \sum_{\lambda\neq 0}\langle\Phi_o|V(\vec{r},\xi)|\Phi_\lambda\rangle\langle\Phi_\lambda| \\ &= \langle\Phi_o|V(\vec{r},\xi)Q \qquad \text{(II.17)}\end{aligned}$$

where the first two terms drop out because of orthogonality, since

$$\langle\Phi_o|H_o|\Phi_\lambda\rangle = H_o\langle\Phi_o|\Phi_\lambda\rangle \text{ and } \langle\Phi_o|H(\xi)|\Phi_\lambda\rangle = E_\lambda\langle\Phi_o|\Phi_\lambda\rangle \qquad \text{(II.18)}$$

if we assume that ε_o, the energy of the ground state, is zero, and if we substitute equation (II.17) into equation (II.16), we can write the latter as follows

$$[E - H_o - \langle\Phi_o|V|\Phi_o\rangle - \langle\Phi_o|VQ\,\frac{1}{E-QHQ}\,QV|\Phi_o\rangle]\psi_o(\vec{r}) = 0 \qquad \text{(II.19)}$$

so we can formally define a generalized optical potential as follows

$$U(r) = \langle\Phi_o|V|\Phi_o\rangle + \langle\Phi_o|VQ\,\frac{1}{E-QHQ}\,QV|\Phi_o\rangle \qquad \text{(II.20)}$$

then we can write equation (II.19) as

$$(E - H_o - U(r))\psi_o(\vec{r}) = 0 \quad . \qquad \text{(II.21)}$$

The leading term in equation (II.20), $\langle\Phi_o|V|\Phi_o\rangle$, yields the real parts of the potential, and hence one can approximate U as

$$U = \langle\Phi_o|V|\Phi_o\rangle \qquad \text{(II.22)}$$

where

$$V \equiv V(\vec{r},\xi) = \sum_{i=1}^{A} v_i(\vec{r}-\vec{r}_i) \tag{II.23}$$

then one can write equation (II.22) as

$$\begin{aligned} U &= \langle\Phi_o|\sum_i v_i(\vec{r}-\vec{r}_i)|\Phi_o\rangle \\ &= \int dr'\, v(\vec{r}-\vec{r}')\,\langle\Phi_o|\sum_i \delta(\vec{r}_i-\vec{r}')|\Phi_o\rangle\ . \end{aligned} \tag{II.24}$$

But by definition

$$\rho(\vec{r}') = \langle\Phi_o|\sum_i \delta(\vec{r}_i-\vec{r}')|\Phi_o\rangle \tag{II.25}$$

where ρ is the matter distribution density, and for short range v one may use the δ-interaction and get the following

$$U = \text{const}\ \rho(\vec{r})\ . \tag{II.26}$$

Thus the potential follows the density in this approximation, and hence one is justified in using the Woods-Saxon functions at least at low energies.

This model could be extended to describe the inelastic scattering. This is usually done by deforming the optical potential. Since the potential follows the density, one can take the spherical density and then deform the surface. This will be discussed in Chapter III.

II.2 The Phenomenological Optical Model

This approach makes the optical model one of the simplest and most successful of nuclear models. The phenomenological optical potential which is used usually to describe nucleon-nucleus elastic scattering has the following form

$$U(r) = V_c(r) - V_o F_o - i(W - 4W_D \frac{d}{dr})F_i$$

$$+ \left(\frac{h}{m_\pi c}\right)^2 [V_{SO} \frac{1}{r} \frac{d}{dr} F_{SO} + iW_{SOI} \frac{1}{r} \frac{d}{dr} F_{SOI}]\vec{\sigma}\cdot\vec{L} \qquad \text{(II.27)}$$

where

$$F_x = [1 + \exp\left(\frac{r - R_x}{a_x}\right)]^{-1} \qquad \text{(II.28)}$$

is the Woods-Saxon function and $R_x = r_x A^{1/3}$, in general the radius and the diffuseness parameters r_x and a_x are different for different parts of the potential. $V_c(r)$ denotes the Coulomb potential due to a uniformly charged sphere of radius R_c and charge Ze, which is necessary for proton scattering to take account of the interaction of the incident proton with the charge distribution due to the protons in the nucleus. It has the form

$$V_c(r) = \frac{Ze^2}{2R_c} \left(3 - (\frac{r}{R_c})^2\right) \qquad r \leq R_c$$

$$= \frac{Ze^2}{r} \qquad r \geq R_c \qquad \text{(II.29)}$$

The quantity V_o denotes the depth of the real central potential, W denotes that of the volume part of the central imaginary potential, W_D denotes that of the surface peaked imaginary potential, and the spin-orbit term is of the Thomas form with V_{SO} as the strength of its real part, and W_{SO} that of the imaginary part. The spin-orbit potential is necessary for particles with non-zero spin because it is needed to explain the elastic polarization of the scattered particles, and also it was found that it improves the calculated cross-section at backward angles (Sh68).

A phenomenological optical potential with suitably adjusted parameters, is able to give a good overall account of the experimental data on elastic scattering. There are thirteen different parameters in the potential, they could be varied in search for a fit to the experimental data. In practice one usually is restricted to a lesser number of parameters to be in search, this depends on the proton incident energy. At low energies, W_{SO} is usually zero, and at intermediate energies, W_D is zero, so in each case we exclude three parameters from the search. These optical model parameters are generally smooth and slowly varying functions of energy and atomic weight of the target (Na81).

The final parameters are determined usually by minimum values of the total Chi-square, and sometimes by putting a constraint on the search to give a reasonable reaction cross-section. The total Chi-square is given by

$$\chi^2 = \chi_\sigma^2 + \chi_p^2 \qquad \text{(II.30)}$$

where σ and p, denote cross-section and polarization respectively, and

$$\chi_\sigma^2 = \sum_{i=1}^{N_\sigma} \left[\frac{\sigma_{ex}(\theta i)-\sigma_{th}(\theta i)}{\Delta\sigma_{ex}(\theta i)}\right]^2 \qquad \text{(II.31)}$$

where $\sigma_{ex}(\theta i)$, $\sigma_{th}(\theta i)$ and $\Delta\sigma_{ex}(\theta i)$ are respectively the experimental theoretical and experimental error values for the cross-section at a center of mass angle θi. A similar expression holds for χ_p^2, the χ^2 associated with the polarization data.

The optical model has been useful in interpreting nuclear scattering at low and intermediate energies. In particular, the occurrence of giant resonances, the total elastic scattering cross-section, the total reaction cross-section, polarization, and the angular distribution of elastically scattered protons, neutrons, deuterons, α-particles, ^{3}He, ^{3}H and heavy ions, can be understood in terms of the optical model. The model is useful also in describing the inelastic scattering and various rearrangement collisions involving transfer of one, two or more particles. In general the model is used extensively in studying nucleon-nucleus scattering, light ions scattering, heavy ions scattering and other scattering processes. Because of these facts one can say that the optical model has produced a considerable amount of information about nuclear structure (Ho63).

We have used the optical model in describing the proton nucleus elastic scattering from different target nuclei at various energies. The results will be analyzed and discussed in chapter VI.

III. THE NON-RELATIVISTIC EXTENDED OPTICAL MODEL "THE STANDARD MODEL"

If a nucleus is bombarded with a proton many things can happen. The most common occurrences are the following: the proton can elastically scatter from the nucleus leaving the latter in its ground state; the proton can give up some of its kinetic energy leaving the nucleus in a bound, excited state; or else the proton can break the nucleus if it has high kinetic energy. In this chapter we will discuss the direct proton nucleus inelastic scattering where the proton leaves the nucleus in an excited state. We will consider only the excitations of the low lying collective states namely the vibrational and rotational states. The discussion will be represented in the framework of the distorted wave Born approximation.

Consider the total Hamiltonian for a nucleon interacting with a target

$$H = H_o + H(\xi) + V(\vec{r},\xi) \qquad \text{(III.1)}$$

where H_o is the K.E. of relative motion, $H(\xi)$ is the target Hamiltonian, and V is the interaction potential of the incident nucleon with the target and it could be written in the following fashion

$$V = \sum_{j=1}^{A} v_j \qquad \text{(III.2)}$$

where A is the target mass number, and v_j is the interaction of the projectile with the jth nucleon in the target.

If we take Ψ as the total wavefunction of the target projectile system such that

$$(H - E)\Psi = 0. \qquad \text{(III.3)}$$

Then the exact transition matrix for an inelastic process from an initial state i to a final state f is given by

$$T_{fi} = \langle \phi(\vec{k}_f)\Phi_f|V|\Psi_i^{(+)}\rangle \tag{III.4}$$

where V is the interaction potential in the outoing channel, the subscript (+) refers to outgoing boundary conditions, Φ_f is the wavefunction of the target in the final state, and

$$\phi_f(\vec{k}_f) = e^{i\vec{k}_f\cdot\vec{r}}\,\eta \tag{III.5}$$

where η is the nucleon spin function, and $\vec{k}_f$ is the wave vector of relative motion in the final state (Ja70). Let us introduce a spherical optical potential U_o in an artificial way:

$$T_{fi} = \langle \phi(\vec{k}_f)\Phi_f|(V-U_o) + U_o|\Psi_i^{(+)}\rangle \ . \tag{III.6}$$

The optical model distorted waves are defined by

$$(H_o + U_o - E)\chi = 0. \tag{III.7}$$

Using the Gell-mann-Goldberger relation for scattering from two potentials, we get the exact T-matrix

$$T_{fi} = \langle \chi_f^{(-)}\Phi_f|V-U_o|\Psi_i^{(+)}\rangle + \langle \chi_f^{(-)}\Phi_f|U_o|\Phi_i\phi(\vec{k}_i)\rangle \ . \tag{III.8}$$

Because U_o is spherical

$$\langle \Phi_f|U_o|\Phi_i\rangle = 0 \qquad \text{if } i \neq f \ . \tag{III.9}$$

Then for inelastic scattering

$$T_{fi} = \langle \chi_f^{(-)}\Phi_f|V-U_o|\Psi_i^{(+)}\rangle \tag{III.10}$$

which is still exact. We do not know $\Psi_i^{(+)}$, so we have to use approximate methods, for example, the distorted wave Born approximation (DWBA). It is assumed that the dominant part of Ψ_i represents elastic scattering. This is supported by the observation that in most cases, elastic scattering is the dominant process. If U_o is the optical potential that describes the elastic scattering of the projectile on the target then we may write

$$\Psi_i^{(+)} \approx \Phi_i \chi_i^{(+)} . \tag{III.11}$$

Where this is expected to be a good approximation in the asymptotic region but may be bad in the interior (Ja70). The right hand side of equation (III.11) is also the leading term in a Born series expansion

$$T_{fi} = \langle \chi_f^{(-)} \Phi_f | V - U_o | \Phi_i \chi_i^{(+)} \rangle . \tag{III.12}$$

We would like to apply this expression to the inelastic scattering leading to the excitation of collective states. The collective model of the nucleus allows for a very simple excitation of the nucleus through a change in the collective state of the system. The states most strongly excited by inelastic scattering are those recognized as involving collective motion of some kind, vibrational or rotational. They usually have the highest cross-sections, this is because of the strong overlap between the initial and final states of the nucleus. The excitation of these states is most commonly represented by means of a macroscopic model (the extended optical model). The first matrix element on the right hand side of equation (III.12) may be approximated as

$$\langle \Phi_f | V | \Phi_i \rangle = \langle \Phi_f | U_D(\vec{r}) | \Phi_i \rangle \tag{III.13}$$

where $U_D(\vec{r})$ is the deformed optical potential. This can also be written as

$$U_D(\vec{r}) = U_o(r) + \Delta U(\vec{r}) \qquad \text{(III.14)}$$

where $U_o(r)$ is the usual spherical optical potential and ΔU is the non-spherical part of U_D. It is clear from equation (III.12) that ΔU now becomes the transition operator for the excitation of the state Φ_f. We can rewrite the T-matrix element (equation (III.12)) for a single excitation of 2^I-pole collective surface mode of an even target nucleus as (Au65 and Sa65):

$$T_{fi} = \langle \chi^{(-)}(\vec{k}_f,\vec{r})\,|\langle IM|\Delta U|00\rangle|\,\chi^{(+)}(\vec{k}_i,\vec{r})\rangle \qquad \text{(III.15)}$$

where $|00\rangle$ describes the ground state with spin parity 0^+. $|IM\rangle$ describes a collective excited state with spin I and projection M. The parity of the state is given by

$$\pi_f = (-)^I. \qquad \text{(III.16)}$$

In this chapter there is necessarily a lot of algebra. Not all the steps are included, however, the interested reader may find some of the missing details in the thesis of Sherif (Sh68). It must be noted that because of the spin-orbit interaction in equation (II.1), the χ's are matirces in the particle spin space. For example

$$\chi^{(+)}(\vec{k}_i,\vec{r}) = \sum_{\mu_i'} |\tfrac{1}{2}\,\mu_i'\rangle \chi^{(+)}_{\mu_i'\mu_i}(\vec{k}_i,\vec{r}) \qquad \text{(III.17)}$$

where μ_i is the spin projection of the incident particle and $|\frac{1}{2}\,\mu_i'\rangle$ is the spin eigenfunction. The quantization axis is taken to be along the incident beam direction. Terms with $\mu_i' \neq \mu_i$ allow the possibility of spin flip during the elastic scattering. The same thing holds for $\chi^{(-)}$. One can write the matrix element as

$$T_{fi} = \sum_{\mu_f'\mu_f} \langle \chi^{(-)}_{\mu_f'\mu_f}(\vec{k}_f,\vec{r})\,|\langle \tfrac{1}{2}\,\mu_f'|\langle IM|\Delta U|00\rangle|\tfrac{1}{2}\,\mu_i'\rangle|\,\chi^{(+)}_{\mu_i'\mu_i}(\vec{k}_i,\vec{r})\rangle \qquad \text{(III.18)}$$

where μ_f is the spin projection of the scattered particle. The X's are distorted waves in the relative coordinate of the projectile and the target. They are solutions of the Schrödinger equation, with appropriate boundary conditions, for a spherical optical model potential.

The interaction potential ΔU is capable of connecting the ground state to the collective states, and usually is obtained by deforming the optical potential $U_o(r)$. This could be achieved by taking the density function $f(r,R_x,a_x)$ (see equation (II.28)) and allowing its radial parametrs to depend on the nuclear orientation such that

$$R' \rightarrow R + \alpha(\hat{r}) \qquad \text{(III.19)}$$

where R is the radius parameter of a typical spherical optical potential, and $\alpha(\hat{r})$ is the displacement of the nuclear surface in the direction $\hat{r}$ and may be given the multipole expansion (Au65):

$$\alpha(\hat{r}) = \sum_{L,M} \xi_{L,M} Y_L^{*M}(\hat{r}) \qquad \text{(III.20)}$$

where $\xi_{L,M}$ is the dynamical coordinate which describes the surface displacement. If we expand $f(r,R+\alpha(\hat{r}),a)$ and keep terms to first order in $\alpha(\hat{r})$ (B164), we get

$$f(r,R+\alpha(\hat{r}),a) \approx f(r,R,a) + \alpha(\hat{r}) \frac{\partial f}{\partial R} . \qquad \text{(III.21)}$$

It is convenient to write

$$\Delta U = \Delta U_C + \Delta U_r + \Delta U_i + \Delta U_{SO} \qquad \text{(III.22)}$$

referring to Coulomb, real, imaginary and spin dependent parts, respectively. The contribution to ΔU in terms of the optical potential parts are (see equation (II.27))

$$\Delta U_r = -V_o \alpha_o(\hat{r}) \frac{\partial}{\partial R_o} f(r,R_o,a_o) \qquad \text{(III.23)}$$

$$\Delta U_i = -\alpha_i(\hat{r})(W - 4a_i W_D \frac{\partial}{\partial r}) \frac{\partial}{\partial R_i} f(r,R_i,a_i) \qquad \text{(III.24)}$$

$$\Delta U_{SO} = \left(\frac{h}{m_{\pi}c}\right)^2 [V_{SO}\vec{\sigma}\cdot \vec{\nabla}\left(\vec{\alpha}_{SO}(\hat{r}) \frac{\partial f(r,R_{SO},a_{SO})}{\partial R_{SO}}\right) \times \frac{1}{i} \vec{\nabla}$$

$$+ iW_{SO}\vec{\sigma}\cdot \vec{\nabla}\left(\vec{\alpha}_{SOI}(\hat{r}) \frac{\partial f(r,R_{SOI},a_{SOI})}{\partial R_{SOI}}\right) \times \frac{1}{i} \vec{\nabla}] \qquad \text{(III.25)}$$

where ΔU_{SO} comes from the deformation of the spin dependent potential, it is of the full Thomas form (Sh69), and it could be split into two parts as follows

$$\Delta U_{SO} = U_{s,def(1)} + U_{s,def(2)} \qquad \text{(III.26)}$$

where

$$U_{s,def(1)} = \left(\frac{\hbar}{m_{\pi}c}\right)^2 [V_{SO}\alpha_{SO}(\hat{r}) \frac{1}{r}\frac{\partial}{\partial r}\left(\frac{\partial f}{\partial R_{SO}}\right)$$

$$+ iW_{SOI}\alpha_{SOI}(\hat{r}) \frac{1}{r}\frac{\partial}{\partial r}\left(\frac{\partial f}{\partial R_{SOI}}\right)]\, \vec{\sigma} \cdot \vec{L} \qquad \text{(III.27)}$$

$$U_{s,def(2)} = \left(\frac{\hbar}{m_{\pi}c}\right)^2 [V_{SO} \frac{\partial f}{\partial R_{SO}} \vec{\sigma}\cdot[\vec{\nabla}(\alpha_{SO}(\hat{r})) \times \frac{1}{i} \vec{\nabla}]$$

$$+ iW_{SOI} \frac{\partial f}{\partial R_{SOI}} \vec{\sigma}\cdot[\vec{\nabla}(\alpha_{SOI}(\hat{r})) \times \frac{1}{i} \vec{\nabla}] \;. \qquad \text{(III.28)}$$

It is found that the contribution to the deformed potential due to ΔU_{SO} is important in this calculation. It improves the calculated cross-sections at backward angles, and also it is necessary to produce the inelastic polarization (Sh69). The Coulomb contribution to ΔU is given by

$$\langle IM|\Delta U_c|00\rangle = \frac{3ZZ'e^2}{R_c^2} \frac{C(I)}{(2I+1)} Y_I^{*M}(\hat{r})\begin{cases}(r/R_c)^I & r < R_c\\ (R_c/r)^{I+1} & r \geq R_c\end{cases} \qquad \text{(III.29)}$$

where Z and Z' refer to the atomic numbers of projectile and target respectively, and the spherical charge distribution is deformed by letting $R_c \to R_c + \alpha_c(\hat{r})$, but maintaining the uniformity of the distribution. The contribution from the inner region $(r < R_c)$ to equation (III.29) is found to be very small.

The nuclear structure information is contained in the matrix element

$$\langle \Phi_f | \Delta U | \Phi_i \rangle . \qquad \text{(III.30)}$$

If we consider the exictation of a rotational level in an even-even nucleus, i.e. $(J_i^{\pi} = 0^+)$, then the wave functions are given by

$$\Phi_i \equiv |00\rangle = \left(\frac{1}{8\pi^2}\right)^{1/2} \psi_{int} D^0_{00}(\varepsilon) \qquad \text{(III.31)}$$

$$\Phi_f \equiv |IM\rangle = \left(\frac{2I+1}{8\pi^2}\right)^{1/2} \psi_{int} D^I_{0M}(\varepsilon) \qquad \text{(III.32)}$$

where D is a rotation matrix, ε denotes the orientation of the body axes w.r.t. the space fixed axes and ψ_{int} is the intrinsic wavefunction. Invoking axial symmetry one can rewrite equation (III.20) in the following fashion

$$\alpha_o = R_o \sum_L a_{LO} Y_L^0(\theta',\phi') \qquad \text{(III.33)}$$

where a_{LO} is real and normally written as β_L, where β_L is called the deformation parameter and (θ',ϕ') refer to body fixed system. Then in the space fixed system one can write

$$Y_L^0(\theta',\phi') = \sum_M D^L_{0M}(\varepsilon) Y_L^{*M}(\hat{r}) \qquad \text{(III.34)}$$

and

$$<\Phi_f|\alpha_o|\Phi_i> = \frac{(2I+1)^{1/2}}{8\pi^2} <\psi_{int} D^I_{OM_f}(\varepsilon) | \sum_{LM} R_o \beta_L D^L_{OM}(\varepsilon) Y^{*M}_L(\hat{r}) | \psi_{int} D^0_{00}(\varepsilon)>$$

$$= \frac{(2I+1)^{1/2}}{8\pi^2} \sum_{LM} R_o \beta_L Y^{*M}_L(\hat{r}) <D^I_{OM_f}(\varepsilon) | D^L_{OM}(\varepsilon) | D^0_{00}(\varepsilon)> . \qquad \text{(III.35)}$$

Since, (Ro57)

$$<D^I_{OM_f}(\varepsilon) | D^L_{OM}(\varepsilon) | D^0_{00}(\varepsilon)> = \frac{8\pi^2}{2I+1} \delta_{L,I} \delta_{M,M_f} . \qquad \text{(III.36)}$$

then

$$<\Phi_f|\alpha_o|\Phi_i> = \frac{R_o \beta_L}{(2I+1)^{1/2}} Y^{*M}_L(\hat{r}) \delta_{I,L} \delta_{M_f,M}$$

$$\equiv C(I) Y^{*M}_I(\hat{r}) . \qquad \text{(III.37)}$$

Now, if we define a radial form factor:

$$F_o(r) = \frac{R_c}{R_o} f_c(r,R_c) - V_o \frac{\partial}{\partial R_o} f(r,R_o,a_o)$$

$$- i(R_i/R_o)(W - 4a_i W_D \frac{\partial}{\partial r}) \frac{\partial}{\partial R_i} f(r,R_i,a_i) \qquad \text{(III.38)}$$

where $f_c(r,R_c)$ ~~is~~ obtained from equation (III.29) by omitting the part $C(I)Y^{*M}_I$, then for the Coulomb, real and imaginary contributions one gets:

$$<IM|\Delta U_c + \Delta U_r + \Delta U_i|00> = C(I) F_o(r) Y^{*M}_I(\hat{r}) \qquad \text{(III.39)}$$

Similarly, for the spin-dependent parts:

$$<IM|U_{s,def(1)}|00> = C_{SO}(I) F_1(r) Y^{*M}_I(\hat{r}) \vec{\sigma}\cdot\vec{L} \qquad \text{(III.40)}$$

$$\langle IM|U_{s,def(2)}|00\rangle = C_{SO}(I)F_2(r)\ \vec{\sigma}\cdot[\vec{\nabla}(Y_I^{*M})\times\frac{1}{i}\vec{\nabla}] \tag{III.41}$$

$$F_1(r) = \left(\frac{h}{m_\pi c}\right)^2[V_{SO}\ \frac{1}{r}\ \frac{\partial^2}{\partial r\partial R_{SO}}\ f(r,R_{SO},a_{SO}) + iW_{SOI}\ \frac{1}{r}\ \frac{\partial^2}{\partial r\partial R_{SOI}}\ f(r,R_{SOI},a_{SOI})] \tag{III.42}$$

$$F_2(r) = \left(\frac{h}{m_\pi c}\right)^2[V_{SO}\ \frac{\partial}{\partial R_{SO}}\ f(r,R_{SO},a_{SO}) + iW_{SOI}\ \frac{\partial}{\partial R_{SOI}}\ f(r,R_{SOI},a_{SOI})]\,. \tag{III.43}$$

The T-matrix element may now be written as:

$$T_{fi} = T_0 + T_1 + T_2$$

where

$$T_0 = C(I)\sum_{\mu_i'\mu_f'}\ \langle\chi^{(-)}_{\mu_f'\mu_f}(\vec{k}_f,\vec{r})|\langle\frac{1}{2}\ \mu_f'|F_o(r)Y_I^{*M}(\hat{r})|\frac{1}{2}\ \mu_i'\rangle|\ \chi^{(+)}_{\mu_i'\mu_i}(\vec{k}_i,\vec{r})\rangle \tag{III.44}$$

$$T_1 = C_{SO}(I)\sum_{\mu_i'\mu_f'}\ \langle\chi^{(-)}_{\mu_f'\mu_f}(\vec{k}_f,\vec{r})|\langle\frac{1}{2}\ \mu_f'|F_1(r)Y_I^{*M}(\hat{r})\vec{\sigma}\cdot\vec{L}\ |\frac{1}{2}\ \mu_i'\rangle|\chi^{(+)}_{\mu_i'\mu_i}(\vec{k}_i,\vec{r})\rangle \tag{III.45}$$

$$T_2 = C_{SO}(I)\sum_{\mu_i'\mu_f'}\ \langle\chi^{(-)}_{\mu_f'\mu_f}(\vec{k}_f,\vec{r})|\langle\frac{1}{2}\ \mu_f'|F_2(r)\vec{\sigma}\cdot[\vec{\nabla}(Y_I^{*M})\times\frac{1}{i}\vec{\nabla}]\ |\frac{1}{2}\ \mu_i'\rangle|\chi^{(+)}_{\mu_i'\mu_i}(\vec{k}_i,\vec{r})\rangle\ . \tag{III.46}$$

These expressions are also valid for the excitation of a vibrational state $|IM\rangle$.

If we choose the z-axis along the vector $\vec{k}_i$ (see Figure 1), then one can write the following partial wave expansion of the distorted

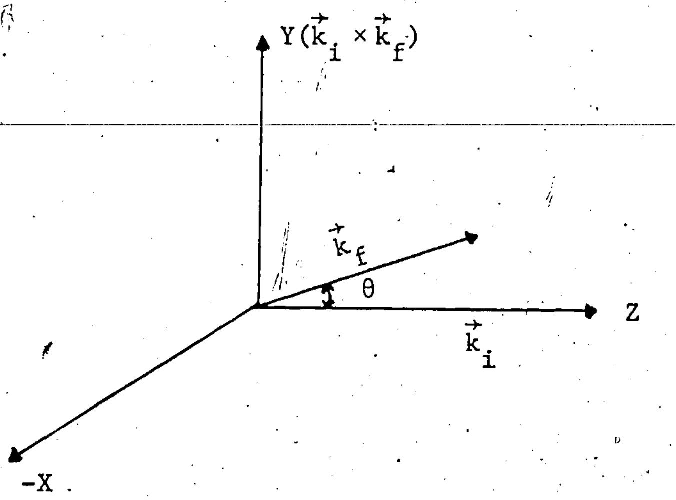

Figure 1. Coordinate system.

waves

$$\chi^{(+)}_{\mu_i'\mu_i}(\vec{k}_i,\vec{r}) = \frac{(4\pi)^{1/2}}{k_i} \sum_{\ell j} i^{\ell} e^{i\sigma_\ell} (2\ell+1)^{1/2} <\ell\tfrac{1}{2};0\mu_i|j\mu_i>$$

$$<\ell\tfrac{1}{2};\mu_i-\mu_i'|j\mu_i> Y_\ell^{\mu_i-\mu_i'}(\hat{r}) \frac{F_{\ell j}(k_i,r)}{r} \qquad \text{(III.47)}$$

and

$$\chi^{*(-)}_{\mu_f'\mu_f}(\vec{k}_f,\vec{r}) = \frac{4\pi}{k_f} \sum_{\ell' j' \nu} i^{-\ell'} e^{i\sigma_{\ell'}} Y_{\ell'}^{\nu-\mu_f}(\theta,0)$$

$$<\ell' \tfrac{1}{2},\nu-\mu_f \; \mu_f|j'\nu><\ell' \tfrac{1}{2};\nu-\mu_f' \; \mu_f'|j'\nu>$$

$$\times Y_{\ell'}^{*\nu-\mu_f'}(\hat{r}) \frac{F_{\ell' j'}(k_f,r)}{r} \qquad \text{(III.48)}$$

Where θ is the scattering angle, $<\ell s,m_\ell m_s|jm_j>$ denotes the Clebsh-Gordan coefficients, σ_ℓ is the Coulomb phase shift

$$\sigma_\ell = \arg \Gamma(\ell+1+in) \qquad \text{(III.49)}$$

where

$$n = \frac{ZZ'e^2}{\hbar^2 k} \qquad \text{(III.49)}$$

and the $F_{\ell j}$ are regular radial wave functions and are normalized such that

$$\lim_{r\to\infty} F_{\ell j} = \frac{i}{2}[H^* - \eta_{\ell j}H_\ell] \tag{III.51}$$

where $\eta_{\ell j}$ are the reflection coefficients or scattering matrix elements for the (ℓj) partial wave, and H_ℓ is the outgoing wave Coulomb function (Hu59).

The final expression for the T-matrix is given by equation (36) in reference (Sh69). In terms of the T-matrix element, which is written as $T(\mu_i,\mu_f,M)$, we can write the differential cross-section in the following fashion

$$\frac{d\sigma}{d\Omega} = \frac{m^{*2}}{4\pi^2\hbar^4}\frac{k_f}{k_i}\frac{1}{2}\sum_{\mu_i\mu_f M}|T(\mu_i;\mu_f M)|^2 \tag{III.52}$$

where m^* is the reduced mass, and the factor $\frac{1}{2}$ arises from averaging over initial spins. The summation over μ_i in equation (III.52) can be taking care of using the relation (Sh71)

$$\sum_{\mu_i,\mu_f M}|T(\mu_i;\mu_f M)|^2 = 2\sum_{\mu_f M}|T(\tfrac{1}{2},\mu_f M)|^2 . \tag{III.53}$$

The inelastic polarization could be written also in terms of the T-matrix element. But before doing that let us define a density matrix ρ in the following fashion (W056)

$$\rho = TT^+ \tag{III.55}$$

which is a matrix in the spin space of the scattered particle. If we write $T(\mu_i;\mu_f M)$ as a matrix element $T_{\mu_f\mu_i}(M)$ such that

$$(T(M)T^+(M))_{\mu_f\mu_f'} = \sum_{\mu_i} T_{\mu_f\mu_i}(M)T^*_{\mu_f'\mu_i}(M) \tag{III.56}$$

and making an incoherent sum over M, we can write the following

$$\rho_{\mu_f\mu_f'} = \sum_{\mu_i M} T(\mu_i;\mu_f M)T^*(\mu_i;\mu_f' M). \tag{III.57}$$

The polarization vector $\vec{P}(\theta)$ is the expectation value of the $\vec{\sigma}$ operator

$$\vec{P}(\theta) = \frac{\mathrm{tr}\rho\vec{\sigma}}{\mathrm{tr}\rho} = \frac{\mathrm{tr}\ TT^{+}\vec{\sigma}}{\mathrm{tr}\ TT^{+}} \qquad \text{(III.58)}$$

where the denominator is given by

$$\begin{aligned} \mathrm{tr}\rho &= \mathrm{tr}\ TT^{+} \\ &= \sum_{\mu_i\mu_f M} |T(\mu_i;\mu_f M)|^2 \end{aligned} \qquad \text{(III.59)}$$

and is thus proportional to the differential cross-section, and the final expression for the polarization could be written as

$$P(\theta) = \frac{2\mathrm{Im}\sum_{m} T(\frac{1}{2};-\frac{1}{2},M)T^{*}(\frac{1}{2};\frac{1}{2}M)}{\sum_{\mu_f M} |T(\frac{1}{2};\mu_f M)|^2} . \qquad \text{(III.60)}$$

It was found that this model is successful in explaining the experimental data for low-lying excited collective states at low energies. (Ba-62, Fr65, Fr67, Fu68, Sh69, Wi68). In the present work we have calculated both the inelastic cross-section and polarization for different targets at intermediate energies. The results of these calculations according to this model will be shown and compared with the results of the unconventional potential calculations in Chapter VII.

IV. DIRAC PHENOMENOLOGY FOR NUCLEON ELASTIC SCATTERING

We have seen in Chapter II how to do elastic scattering according to a non-relativistic model, i.e. the standard optical model. In this chapter we discuss another model for doing elastic scattering also, but from a different point of view. A relativistic optical model is constructed to be used for the analysis of proton elastic scattering (Ar81). The model is based on the Dirac equation with a mixture of Lorentz scalar potential, U_s, and the time like component of a four-vector potential, U_v. The time independent Dirac equation which describes proton elastic scattering is ($\hbar = c = 1$)

$$\{\vec{\alpha}\cdot\vec{p} + \beta(m + U_s(r)) + (U_v(r) + V_c(r)\}\psi(\vec{r}) = E\psi(\vec{r}) \tag{IV.1}$$

where α and β are the 4 by 4 Dirac matrices and

$$\alpha = \begin{pmatrix} 0 & \vec{\sigma} \\ \vec{\sigma} & 0 \end{pmatrix} ; \qquad \beta = \begin{pmatrix} I & 0 \\ 0 & -I \end{pmatrix} \tag{IV.2}$$

$\vec{\sigma}$ is the Pauli 2 by 2 spin matrix, I is the 2 by 2 unit matrix, $\vec{p}$ is the momentum operator of the incident proton, m is the rest mass of the proton, ψ is the Dirac spinor, V_c is the Coulomb potential (it is determined from the empirical nuclear charge distribution given by electron scattering experiments) and E is the proton total energy.

Major properties of the nucleon-nucleon interaction can be represented by one boson exchange potentials employing the known mesons (π, $\rho,\omega,\phi,\ldots$) plus the addition of the $J^{\pi}=0^{+}$, T=0 "σ" meson which is presently interpreted in terms of two-pion exchange processes. The dominant characteristics of the nucleon-nucleus interaction for a spin zero isospin zero target nucleus are expected to be represented by the exchange of neutral scalar and vector mesons (Ar81).

The main effect of using a mixture of a Lorentz scalar and the time like component of a four-vector potential in the Dirac equation was originally discussed by Furry (Fu36). He pointed out that to lowest order in v/c the sum U_v+U_s contributes to the central potential, while the difference U_v-U_s appears in the spin orbit potential. This feature of the potential mixtures plays an essential role in the description of both elastic scattering and polarization data at intermediate energies (Ar81). This model is quite successful in describing the experimental data at intermediate energy. In particular, for energies above 200 MeV, it seems to be superior than the standard optical model.

In order to compare with the non-relativistic optical model, it is convenient to rewrite equation (IV.1) in second order form. If we write the Dirac spinor in terms of an upper and a lower component as follows

$$\psi = \begin{pmatrix} \psi_\mu \\ \psi_\ell \end{pmatrix} \qquad \text{(IV.3)}$$

and if we substitute equations (IV.2, IV.3) into equation (IV.1), we get,

$$\left[\begin{pmatrix} 0 & \vec{\sigma}\cdot p \\ \vec{\sigma}\cdot p & 0 \end{pmatrix} + \begin{pmatrix} m+U_s & 0 \\ 0 & -(m+U_s) \end{pmatrix} + \begin{pmatrix} U_v+V_c & 0 \\ 0 & U_v+V_c \end{pmatrix}\right]\begin{pmatrix} \psi_\mu \\ \psi_\ell \end{pmatrix} = E\begin{pmatrix} \psi_\mu \\ \psi_\ell \end{pmatrix} . \qquad \text{(IV.4)}$$

This will lead to two coupled equations as follows

$$\vec{\sigma}\cdot\vec{p}\psi_\ell + (m+U_s+U_v+V_c)\psi_\mu = E\psi_\mu \qquad \text{(IV.5)}$$

$$\vec{\sigma}\cdot\vec{p}\psi_\mu + (U_v+V_c-m-U_s)\psi_\ell = E\psi_\ell \quad , \qquad \text{(IV.6)}$$

From equation (IV.6) we get

$$\psi_\ell = \frac{1}{E+m+U_s-U_v-V_c}\,\vec{\sigma}\cdot\vec{p}\,\psi_\mu$$

$$= \frac{1}{D}\,\vec{\sigma}\cdot\vec{p}\,\psi_\mu \quad . \qquad \text{(IV.7)}$$

where

$$D \equiv E + m + U_s - U_v - V_c \ . \qquad \text{(IV.8)}$$

Using equation (IV.7) in equation (IV.5) we get

$$\vec{\sigma}\cdot\vec{p}\,\frac{1}{D}\,\vec{\sigma}\cdot\vec{p}\psi_\mu + (m+U_s+U_v+V_c)\psi_\mu = E\psi_\mu . \qquad \text{(IV.9)}$$

After some mathematical manipulations one can write the following

$$\vec{\sigma}\cdot\vec{p}\,\frac{1}{D}\,\vec{\sigma}\cdot\vec{p}\psi_\mu = (\vec{\sigma}\cdot\vec{p}\,\frac{1}{D})\,\vec{\sigma}\cdot\vec{p}\psi_\mu + \frac{1}{D}\,(\vec{\sigma}\cdot\vec{p})(\vec{\sigma}\cdot\vec{p})\psi_\mu$$

$$= \frac{i}{D^2}\,\frac{1}{r}\,\frac{\partial D}{\partial r}\,\vec{r}\cdot\vec{p}\psi_\mu - \frac{1}{D^2}\,\frac{1}{r}\,\frac{\partial D}{\partial r}\,\vec{\sigma}\cdot\vec{L}\psi_\mu$$

$$+ \frac{1}{D}\,p^2\psi_\mu \ . \qquad \text{(IV.10)}$$

Substituting equation (IV.10) in equation (IV.9), one can rewrite the latter as follows

$$P^2\psi_\mu + D(m+U_s+U_v+V_c)\psi_\mu - \frac{1}{D}\,\frac{1}{r}\,\frac{\partial D}{\partial r}\,\vec{\sigma}\cdot\vec{L}\,\psi_\mu$$

$$+ \frac{i}{D}\,\frac{1}{r}\,\frac{\partial D}{\partial r}\,\vec{r}\cdot\vec{p}\psi_\mu = ED\psi_\mu \ . \qquad \text{(IV.11)}$$

To eliminate the Darwin term $\frac{i}{D}\,\frac{1}{r}\,\frac{\partial D}{\partial r}\,\vec{r}\cdot\vec{p}\psi_\mu$ one can make the substitution

$$\psi_\mu(\vec{r}) = (D(r))^{1/2}\Phi_\mu(\vec{r}) \ . \qquad \text{(IV.12)}$$

Then the term $P^2\psi_\mu$ could be written as

$$P^2\psi_\mu = P^2 D^{1/2}\Phi_\mu$$

$$= (P^2 D^{1/2})\Phi_\mu + 2\vec{P}D^{1/2}\cdot\vec{P}\Phi_\mu + D^{1/2}P^2\Phi_\mu \qquad \text{(IV.13)}$$

and after some algebra it could be rewritten as

$$P^2\psi_\mu = -\frac{1}{r} D^{-1/2} D'\Phi_\mu + \frac{1}{4} D^{-3/2} D'^2 \Phi_\mu - \frac{1}{2} D^{-1/2} D''\Phi_\mu - D^{-1/2} D' \frac{\partial\Phi_\mu}{\partial r} + D^{1/2} P^2 \Phi_\mu \qquad \text{(IV.14)}$$

where (') and (") mean the first and the second derivatives with respect to r, respectively. Equation (IV.11) could be rewritten as

$$P^2\Phi_\mu(r) + \frac{3}{4}(D'/D)^2\Phi_\mu - \frac{1}{2}(D''/D)\Phi_\mu(r) - \frac{1}{r}(D'/D)\Phi'_\mu(r) + D(m+U_s+U_v+V_c)\Phi_\mu(r) - \frac{1}{r}(D'/D)\vec{\sigma}\cdot\vec{L}\Phi_\mu(r) = ED\Phi_\mu(r). \qquad \text{(IV.15)}$$

Since

$$D(m+U_s+U_v+V_c) - ED = 2E(U+V_c) + m^2 - E^2 + 2mU_s + U_s^2 - (U_v+V_c)^2 . \qquad \text{(IV.16)}$$

Then equation (IV.15) reduces to

$$\{P^2 + \frac{3}{4}(D'/D)^2 - \frac{1}{2}(D''/D) - \frac{1}{r}(D'/D) + 2mU_s + 2E(U_v+V_c) + U_s^2 - (U_v+V_c)^2 - \frac{1}{r}(D'/D)\vec{\sigma}\cdot\vec{L}\}\Phi_\mu(r) = (E^2-m^2)\Phi_\mu(r) . \qquad \text{(IV.17)}$$

If we divide equation (IV.17) by 2m, noting that

$$\frac{E^2-m^2}{2m} = \frac{k^2}{2m} \qquad \text{(IV.18)}$$

one can rewrite (IV.17) as follows

$$\left(\frac{P^2}{2m} + U_{eff}(r) + U_{SO}(r)\vec{\sigma}\cdot\vec{L}\right)\Phi_\mu(r) = \frac{k^2}{2m}\Phi_\mu(r) \qquad \text{(IV.19)}$$

where $U_{eff}(r)$ is the effective central potential defined as follows

$$U_{eff}(r) = \frac{1}{2m}\left[\frac{3}{4}\left(\frac{D'}{D}\right)^2 - \frac{1}{2}\left(\frac{D''}{D}\right) - \frac{1}{r}\left(\frac{D'}{D}\right)\right] + U_s + \frac{E}{m}(U_v+V_c) + \frac{1}{2m}(U_s^2 - (U_v+V_c)^2] \qquad \text{(IV.20)}$$

and $U_{SO}(r)$ is the spin orbit potential defined as follows

$$U_{SO}(r) = -\frac{1}{2m}\frac{1}{D}\frac{1}{r}\frac{dD}{dr} \, . \qquad \text{(IV.21)}$$

Equation (IV.19) looks like the non-relativistic Schrödinger equation which is usually written in the following fashion

$$\frac{p^2}{2m}\psi + V\psi = E\psi \, . \qquad \text{(VI.22)}$$

Since equations (IV.19) and (IV.22) produce equivalent elastic scattering, equation (IV.19) is called the Schrödinger equivalent equation. It should be mentioned here that the wave function Φ_μ, even though it is not the upper component of the Dirac spinor, it has the same asymptotic behaviour as ψ_μ in the absence of the Coulomb potential, this is because of the short range of U_v and U_s.

Equations (IV.20, IV.21) show that if U_v is repulsive (as it would be if it is due to neutral vector meson exchange), and U_s is attractive (as it would be if its origin is neutral scalar meson exchange), then U_v and U_s tend to cancel in the effective central potential while they add in the spin-orbit. Notice that there is no explicit spin dependence in the optical potentials U_v and U_s, where those are usually written as

$$U_v(r) = V_v f(r,R_v,a_v) + iW_v f(r,R_{wv},a_{wv}) \qquad \text{(IV.23)}$$

and

$$U_s(r) = V_s f(r,R_s,a_s) + iW_s f(r,R_{ws},a_{ws}) \qquad \text{(IV.24)}$$

where the function $f(r,R_x,a_x)$ is of the Woods-Saxon form. Note that the effective spin-orbit potential is completely specified by the potential mixture. We will call this type of calculation "the Dirac model" in the present work. The characteristics of the potentials and the elastic scattering cross-section and polarization predicted by this model will be discussed and shown in Chapter VI, and they will be compared with their counterparts from the standard model.

V. RELATIVISTIC INELASTIC SCATTERING (THE DIRAC MODEL)

We have seen in chapter III how to do inleastic scattering according to a non-relativistic model, namely the extended standard optical model. This model has been successful in describing the experimental data at low energies, but its credibility becomes suspect at intermediate and high energies. The intermediate energy range attracts the interest of many nuclear physicists these days, especially with the availability of facilities like SACLAY, SIN, LAMF, IUCF, and TRIUMF. Since the Dirac equation has been successful in describing proton elastic scattering at intermediate energies in recent years (Ar81,82), then the question arises as to whether there are serious implications for inelastic scattering as a result of the unconventional shape of the real central potential. Satchler (Sa83) has recently studied the effect on the inelastic cross-section for some low-lying states near 200 MeV, but his calculations were based on varying the shapes of the potentials and using the non-relativistic Schrödinger equation. In this chapter we will discuss a model based on the use of the Dirac equation to describe elastic scattering as discussed in chapter IV. To allow for inelastic scattering, we have to deform the scalar and the vector potentials for this purpose we use the same method used earlier to deform the non-relativistic potentials (see chapter III). The vector and scalar potentils are defined by equations (IV.23) and (IV.24) respectively. We can write the deformed vector potential in the following fashion

$$U_v^D(\vec{r}) = V_v f(r, R_v + \alpha_v(\hat{r}), a_v) + iW_v f(r, R_{wv} + \alpha_{wv}(\hat{r}), a_{wv}) \qquad (V.1)$$

and again express this in terms of spherical and non-spherical parts:

$$U_v^D(\vec{r}) = U_v(r) + \Delta U_v(\vec{r}) \qquad (V.2)$$

if we expand the function f and keep terms of first order in $\alpha(\hat{r})$ we can write (see equation (III.21))

$$\Delta U_v(\vec{r}) = \alpha_v(\hat{r})V_v \frac{\partial f}{R_v} + iW_v(\hat{r})W_v \frac{\partial f}{\partial R_{wv}} \qquad (V.3)$$

and by the same method, we can write for the scalar potential

$$\Delta U_s(\vec{r}) = \alpha_s(\hat{r})V_s \frac{\partial f}{\partial R_s} + i\alpha_{ws}(\hat{r})W_s \frac{\partial f}{\partial R_{ws}} . \qquad (V.4)$$

The effective central potential is defined by equation (IV.20), and it could be split into two parts as follows

$$U_{eff}(r) = A(r) + B(r) \qquad (V.5)$$

where

$$A(r) = \frac{(\hbar c)^2}{2m} [\frac{3}{4} (\frac{D'}{D})^2 - \frac{1}{2} (\frac{D''}{D}) - \frac{1}{r} (\frac{D'}{D})] \qquad (V.6)$$

and

$$B(r) = U_s(r) + \frac{E}{m} (U_v + V_c) + \frac{1}{2m} [U_s^2 - (U_v + V_c)^2] \qquad (V.7)$$

where D is defined by equation (IV.8). The deformation of B(r) follows as a result of deforming the scalar and vector potential and it could be written as follows

$$B^D(\vec{r}) = U_s^D(\vec{r}) + \frac{E}{m} (U_v^D(\vec{r}) + V_c^D(\vec{r})) + \frac{1}{2m} [U_s^{2D}(\vec{r}) - U_v^{2D}(\vec{r}) - 2U_v^D(\vec{r})V_c^D(\vec{r}) - V_c^{2D}(\vec{r})] . \qquad (V.8$$

which may be written as

$$B^D(\vec{r}) = B(r) + \Delta B(\vec{r}) \qquad (V.9)$$

where

$$\Delta B(\vec{r}) = \Delta U_s(\vec{r}) + \frac{E}{m}[\Delta U_v(\vec{r}) + \Delta V_c(\vec{r})]$$
$$+ \frac{1}{2m}[2U_s(r)\Delta U_s(\vec{r}) - 2U_v(r)\Delta U_v(\vec{r}) - 2U_v(r)$$
$$\Delta V_c(\vec{r}) - 2V_c(r)\Delta V_c(\vec{r})] \quad . \qquad (V.10)$$

The contributions to $\Delta B(\vec{r})$ due to Coulomb effects were investigated and found to be negligible, so we decided to leave these terms out, this will be discussed in chapter VII. We can then rewrite equation (V.10) as follows

$$\Delta B(\vec{r}) = \Delta U_s(\vec{r}) + \frac{E}{m}\Delta U_v(\vec{r}) + \frac{1}{m}[U_s(r)\Delta U_s(\vec{r})$$
$$- U_v(r)\Delta U_v(\vec{r})] \quad . \qquad (V.11)$$

The deformation of $A(r)$, depends on the deformation of $D(r)$ and its derivatives, and it could be done in the same way mentioned before. One can write

$$\Delta D(\vec{r}) = \Delta U_s(\vec{r}) - \Delta U_v(\vec{r}) \qquad (V.12)$$

$$\Delta D'(\vec{r}) = \Delta U'_s(\vec{r}) - \Delta U'_v(\vec{r}) \qquad (V.13)$$

and

$$\Delta D''(\vec{r}) = \Delta U''_s(\vec{r}) - \Delta U''_v(\vec{r}) \qquad (V.14)$$

After some straightforward algebra one can write $\Delta A(\vec{r})$ as follows

$$\Delta A(\vec{r}) = \frac{(hc)^2}{2m}[\frac{3}{2}(\frac{D'}{D})\Delta D' - \frac{3}{2}(\frac{D'}{D})^2(\frac{\Delta D}{D}) + \frac{1}{2}D''(\frac{\Delta D}{D^2})$$
$$- \frac{1}{2}(\frac{\Delta D''}{D}) - \frac{1}{r}(\frac{\Delta D'}{D}) + \frac{1}{r}D'(\frac{\Delta D}{D^2})] \qquad (V.15)$$

if we use the following relation

$$\nabla_r^2 D = \frac{2}{r}D' + D'' \qquad (V.16)$$

then we can write

$$D'' = \nabla_r^2 D - \frac{2}{r} D' \tag{V.17}$$

and

$$(\Delta D)'' = \nabla_r^2 (\Delta D) - \frac{2}{r} (\Delta D)' \ . \tag{V.18}$$

Substituting equations (V.17), (V.18) in equation (V.15) yields

$$\Delta A(\vec{r}) = \frac{(hc)^2}{2m} \left[\frac{3}{2} \left(\frac{D'}{D^2}\right)(\Delta D)' - \frac{3}{2} \left(\frac{D'}{D}\right)^2 \left(\frac{\Delta D}{D}\right)\right]$$

$$+ \frac{(hc)^2}{4m} \left[\nabla_r^2 D \left(\frac{\Delta D}{D^2}\right) - \frac{1}{D} \nabla_r^2 (\Delta D)\right] . \tag{V.19}$$

Then the deformed piece of the effective central potential $\Delta U_{eff}(\vec{r})$ is just the sum of equations (V.11) and (V.19) since

$$\Delta U_{eff}(\vec{r}) = \Delta A(\vec{r}) + \Delta B(\vec{r}) \quad . \tag{V.20}$$

If we define a formfactor

$$F_o(r) = V_s \frac{\partial f_s}{\partial R_s} + V_v \frac{\partial f_v}{\partial R_v} + \frac{1}{m} \left[V_s^2 f_s \frac{\partial f_s}{\partial R_s} - W_s^2 f_{ws} \frac{\partial f_{ws}}{\partial R_{ws}}\right]$$

$$+ i\left[W_s \frac{\partial f_{ws}}{\partial R_{ws}} + \frac{1}{m} V_s W_s \left(f_s \frac{\partial f_{ws}}{\partial R_{ws}} + f_{ws} \frac{\partial f_s}{\partial R_s}\right)\right]$$

$$+ \frac{(hc)^2}{4m} \left[3\left(\frac{D'}{D}\right)^3 - 3 \frac{D'D''}{D^2} + \frac{1}{D} \nabla^2 (D') - \frac{D'}{D^2} \nabla^2 D\right] \tag{V.21}$$

then

$$\langle IM | \Delta U_{eff}(\vec{r}) | 00 \rangle = C(I) F_o(r) Y_I^{*M}(\hat{r}) \ . \tag{V.22}$$

The deformation of the spin dependent part is more involved than that of the effective central potential but it is done by the same method. The deformed spin-orbit potential is given by

$$U_{SO}^D(\vec{r}) = - \frac{(hc)^2}{2m} \frac{1}{D(\vec{r})} \vec{\sigma} \cdot \vec{\nabla}(D(\vec{r})) \times \vec{p} \tag{V.23}$$

where

$$\frac{1}{D(\vec{r})} = \frac{1}{D(r)+\Delta D(\vec{r})} = \frac{1}{D(r)} - \frac{\Delta D(\vec{r})}{D^2(r)} \qquad (V.24)$$

if we substitute equation (V.24) into equation (V.23), this yields

$$U^D_{SO}(\vec{r}) = \frac{-(hc)^2}{2m}\left[\left(\frac{1}{D(r)} - \frac{\Delta D(\vec{r})}{D^2(r)}\right)\vec{\sigma}\cdot\vec{\nabla}(D(r)+\Delta D(\vec{r}))\times\vec{p}\right] \qquad (V.25)$$

which could be rewritten as follows

$$U^D_{SO}(\vec{r}) = \frac{-(hc)^2}{2m}\left[\frac{1}{D(r)}\frac{1}{r}\frac{\partial D}{\partial r}\vec{\sigma}\cdot\vec{L} + \frac{1}{D}\vec{\sigma}\cdot\vec{\nabla}(\Delta D)\times\vec{p} - \frac{\Delta D}{D^2}\vec{\sigma}\cdot\vec{\nabla}(D+\Delta D)\times\vec{p}\right]. \qquad (V.26)$$

The first term on the r.h.s. is the spherical spin-orbit interaction, and the other parts form the deformed spiece,

$$\Delta U_{SO}(\vec{r}) = \frac{-(hc)^2}{2m}\left[\frac{1}{D}\vec{\sigma}\cdot\vec{\nabla}(\Delta D)\times\vec{p} - \frac{\Delta D}{D^2}\vec{\sigma}\cdot\vec{\nabla}(D)\times\vec{p} - \frac{\Delta D}{D^2}\vec{\sigma}\cdot\vec{\nabla}(\Delta D)\times\vec{p}\right] \qquad (V.27)$$

where the last term drops out if we keep $\Delta U_{SO}(\vec{r})$ to first order in $\alpha(\hat{r})$, and the second term is not hermetian when the potentials are real and we have found its effect on the calculations to be negligible since it is divided by D^2, so we decided to leave this term out. Then equation (V.27) could be rewritten as follows

$$\Delta U_{SO}(\vec{r}) = U_{s,def(1)} + U_{s,def(2)}$$

where

$$U_{s,def(1)} = \frac{-(hc)^2}{2m}\frac{1}{D}\left[\left(\alpha_s(\hat{r})V_s\frac{\partial^2 f_s}{\partial r\partial R_s} - \alpha_v(\hat{r})V_v\frac{\partial^2 f_v}{\partial r\partial R_v}\right) + i\left(\alpha_{ws}(\hat{r})W_s\frac{\partial^2 f_{ws}}{\partial r\partial R_{ws}} - \alpha_{wv}(\hat{r})W_v\frac{\partial^2 f_{wv}}{\partial r\partial R_{wv}}\right)\right]\vec{\sigma}\cdot\vec{L} \qquad (V.29)$$

and

$$U_{s,def(2)} = \frac{-(hc)^2}{2m}\,\frac{1}{D}\left\{V_s\,\frac{\partial f_s}{\partial R_s}\,\vec{\sigma}\cdot[\vec{\nabla}\alpha_s(\hat{r})\times\frac{1}{i}\,\vec{\nabla}]\right.$$

$$-\,V_v\,\frac{\partial f_v}{\partial R_v}\,\vec{\sigma}\cdot[\vec{\nabla}\alpha_v(\hat{r})\times\frac{1}{i}\,\vec{\nabla}]$$

$$+\,i(W_s\,\frac{\partial f_{ws}}{\partial R_{ws}}\,\vec{\sigma}\cdot[\vec{\nabla}\alpha_{ws}(\hat{r})\times\frac{1}{i}\,\vec{\nabla}]$$

$$\left.-\,W_v\,\frac{\partial f_{wv}}{\partial R_{wv}}\,\vec{\sigma}\cdot[\vec{\nabla}\sigma_{wv}(\hat{r})\times\frac{1}{i}\,\vec{\nabla}])\right\} \qquad (V.30)$$

which is of the full Thomas form (Sh68). We can define the form-factors for $U_{s,def(1)}$ and $U_{s,def(2)}$ as follows

$$\langle IM|U_{s,def(1)}|00\rangle = C_{SO}(I)F_1(r)Y_I^{*M}(\hat{r})\vec{\sigma}\cdot\vec{L} \qquad (V.31)$$

and

$$\langle IM|U_{s,def(2)}|00\rangle = C_{SO}(I)F_2(r)\vec{\sigma}\cdot[\vec{\nabla}(Y_I^{*M}(\hat{r})\times\frac{1}{i}\,\vec{\nabla}]$$

where

$$F_1(r) = \frac{-(hc)^2}{2m}\,\frac{1}{D}\,[V_s\,\frac{\partial^2 f_s}{\partial r\partial R_s} - V_v\,\frac{\partial^2 f_v}{\partial r\partial R_v} + i(W_s\,\frac{\partial^2 f_{ws}}{\partial r\partial R_{ws}}$$

$$-\,W_v\,\frac{\partial^2 f_{wv}}{\partial r\partial R_{wv}})] \qquad (V.33)$$

and

$$F_2(r) = \frac{-(hc)^2}{2m}\,\frac{1}{D}\,[V_s\,\frac{\partial f_s}{\partial R_s} - V_v\,\frac{\partial f_v}{\partial R_v} + i(W_s\,\frac{\partial f_{ws}}{\partial R_{ws}} - W_v\,\frac{\partial f_{wv}}{\partial R_{wv}})]. \qquad (V.34)$$

Then if we substitute equations (V.21), (V.33) and (V.34) in equations (III.44), (III.45) and (III.46) the calculations will follow the same order as that of chapter III.

We have done the calculations for the inelastic cross-section and polarization according to this model. We will compare the results of this model with those obtained from the non-relativistic calculations which are based on the extended standard optical model, and with the results of another model (Sa83) for some cases in chapter VII.

VI. ELASTIC SCATTERING FITS

In this chapter we shall discuss the elastic scattering fits for different even-even nuclei at different bombarding energies. Two different codes were used in fitting the elastic cross-section and polarization data. The first code is a standard optical model potential called Magali (Ra69), relativistic kinematics were used in this code, i.e., we used an effective bombarding energy that ensured the relativistically correct centre of mass momentum. The Dirac equation based potential has been taken from the analysis of Cooper et al. (Co82). This analysis was done using the code Runt (1981). The code Magali is based on the optical potential described by equation (II.27) while the code Runt is based on the optical potential described by equations (IV.20) and IV.21). In both codes 12 parameters were used in an automatic search routine using a chi-squared minimization technique (see equations (II.30) and (II.31)). These parameters were varied to fit the calculated proton elastic scattering cross-section and polarization to the experimental data. The radius of the charge distribution R_c was held constant in both codes, since the fit is fairly insensitive to it. The parameters obtained from the code Magali are listed in Table I for different cases. We show a sample of the parameters obtained from the code Runt (Co82) in Table II. In both tables we have listed the optical potential parameters for different target nuclei at different energies. As can be seen from Table I the parameters of the potential are energy dependent, they vary with increasing energy. They also depend on the target mass number as it was reported by Nadaseen et al. (Na81) and by van Oers et al. (Va74). We also show the calculated reaction cross-section (σ_R) in millibarns for each case.

TABLE I

OPTICAL MODEL PARAMETERS

(THE STANDARD MODEL)

Target	^{12}C	^{24}Mg	^{28}Si	^{32}S	^{40}Ca	^{40}Ca	^{40}Ca	^{40}Ca	^{208}Pb
E_p(MeV)	200	155	155	155	155	181	300	500	200
V_o(MeV)	14.18	12.29	13.96	12.90	13.68	17.52	25.72	-41.69	13.17
r_o(F)	1.30	1.39	1.34	1.37	1.37	1.29	1.07	0.70	1.33
a_o(F)	0.68	0.57	0.50	0.59	0.61	0.70	0.68	0.79	0.58
W(MeV)	17.64	22.31	58.56	19.55	6.00	13.81	20.26	54.21	25.90
W_D(MeV)	0.00	0.00	0.00	0.00	0.00	0.00	0.00	0.00	0.00
r_W(F)	0.95	0.98	0.78	1.06	1.26	1.15	1.19	1.04	1.13
a_w(F)	0.78	0.81	0.78	0.80	0.60	0.81	0.78	0.79	0.88
V_{SO}(MeV)	4.01	4.19	14.1	4.72	4.86	3.20	3.58	4.95	3.38
V_{SO}(F)	0.88	0.90	0.42	0.93	1.06	1.02	1.06	0.99	1.10
a_{SO}(F)	0.66	0.71	0.96	0.70	0.58	0.65	0.62	0.75	0.73
W_{SOI} (MeV)	-2.09	-1.65	-5.94	-1.24	-1.61	-2.25	-1.39	-4.15	-2.69
r_{SOI}(F)	0.96	0.96	0.78	1.02	1.06	1.01	0.94	1.08	1.08
a_{SOI}(F)	0.37	0.57	0.59	0.58	0.68	0.56	0.60	0.68	0.70
σ_RmB	194.74	402.5	501.2	494.8	296.8	495.5	568.5	591.5	1827.7

TABLE II

OPTICAL MODEL PARAMETERS FOR ^{40}Ca AT $E_p = 181$ MeV

(THE DIRAC MODEL)

V_v(MeV)	r_v(F)	a_v(F)
295.184	1.0416	0.6017
W_v(MeV)	r_{wv}(F)	a_{wv}(F)
-89.7876	1.0774	0.6518
V_s(MeV)	r_s(F)	a_s(F)
-404.386	1.0288	0.6314
W_s(MeV)	r_{ws}(F)	a_{ws}(F)
93.6447	1.0871	0.6262

σ_R(mB) = 594.80

In the present work we will label the curves resulting from the standard model as, STANDARD, while those resulting from the Dirac model as, DIRAC. The curve labeled Dirac is actually obtained using the Schrödinger equivalent potential (the effective central potential $U_{eff}(r)$, see equation (IV.20)) as well as relativistic kinematics in the Schrödinger equation. The wave function which satisfies the Schrödinger equation, with $U_{eff}(r)$, differs from the upper component of the Dirac wave function only in the nuclear interior but they have the same asymptotic behaviour. One, therefore, expects the equivalent potential ($U_{eff}(r)$) when used in a Schrödinger equation based elastic scattering calculation, to reproduce the same elastic scattering obtained using the Dirac equation. This point has been checked by actual numerical calculations for targets up to ^{208}Pb by Cooper (Co81).

We will show below a few cases from the analysis of proton elastic scattering in this work.

VI.1 ^{12}C

Figures 2 and 3 show the fits to the elastic scattering cross-section and polarization data at 200 MeV. The data are from Meyer et al. (Me81). The experimental data were reduced to 60°, since there is a large disagreement in the fit according to the two models for angles beyond that. The fit is comparable or equivalent to that of Meyer et al. (Me81). The reaction cross-section resulting from the calculation of the standard model equals 292.7 milli barns (mb), while that of the Dirac model equals 236.5 mb.

VI.2 ^{24}Mg

Figures 4 and 5 show the fits to the elastic scattering cross-section and polarization experimental data at 155 MeV. The data are

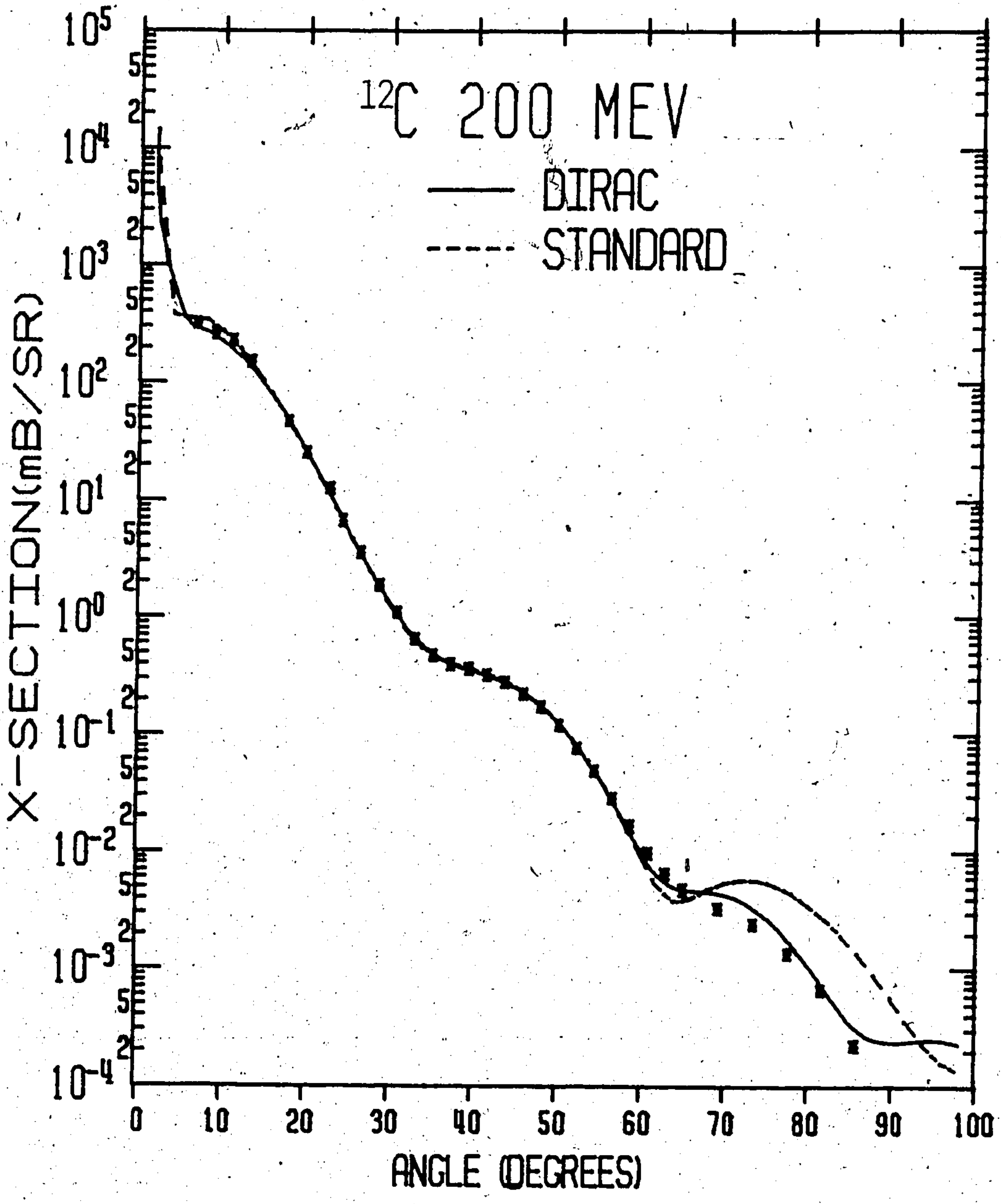

Figure 2 Differential cross-section for P + ^{12}C elastic scattering at E_p = 200 MeV. The solid curve is the DIRAC model and the dashed curve is the STANDARD model.

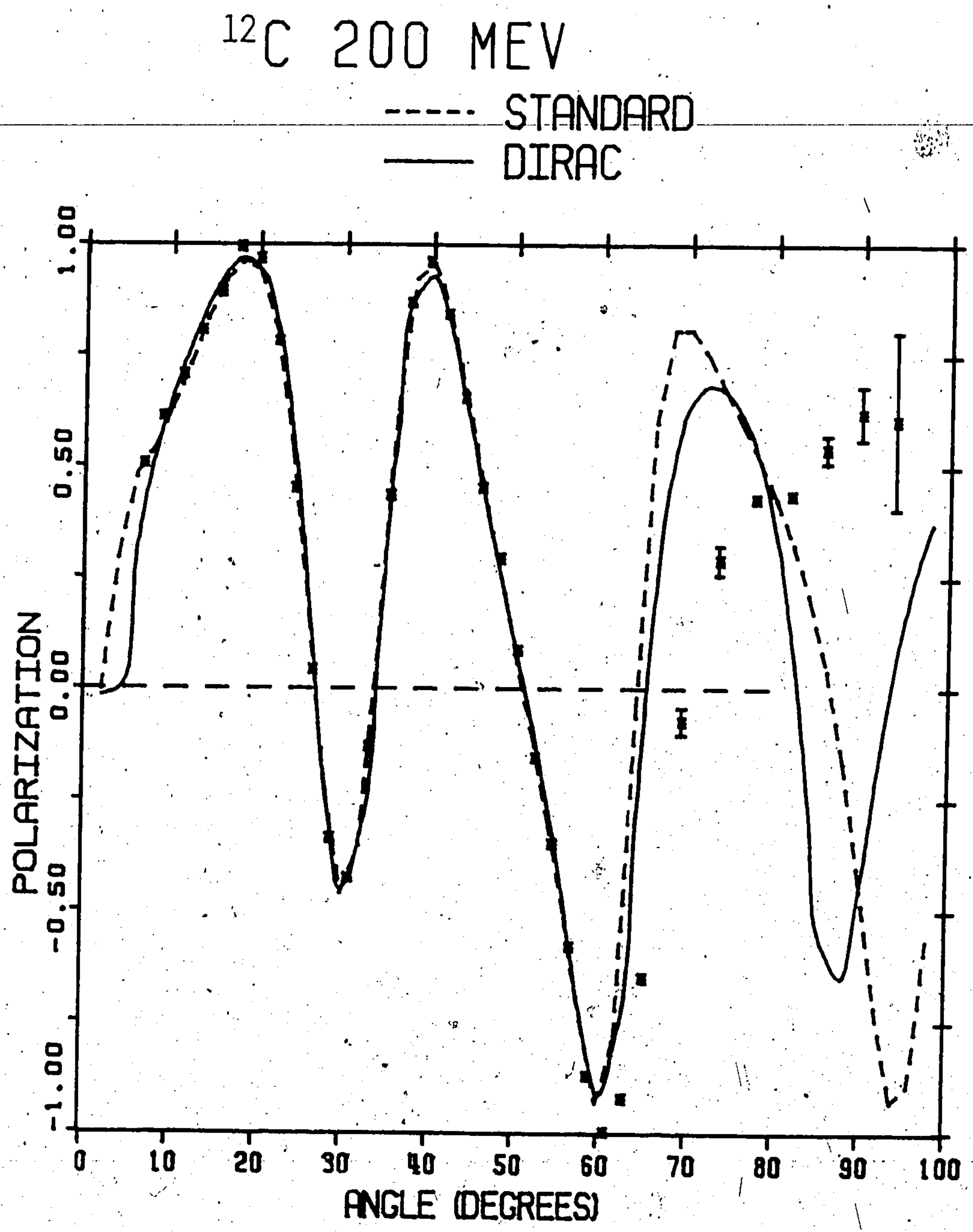

Figure 3 Polarization for P + ^{12}C elastic scattering at E_p = 200 MeV. The solid curve is the DIRAC model and the dashed curve is the STANDARD model.

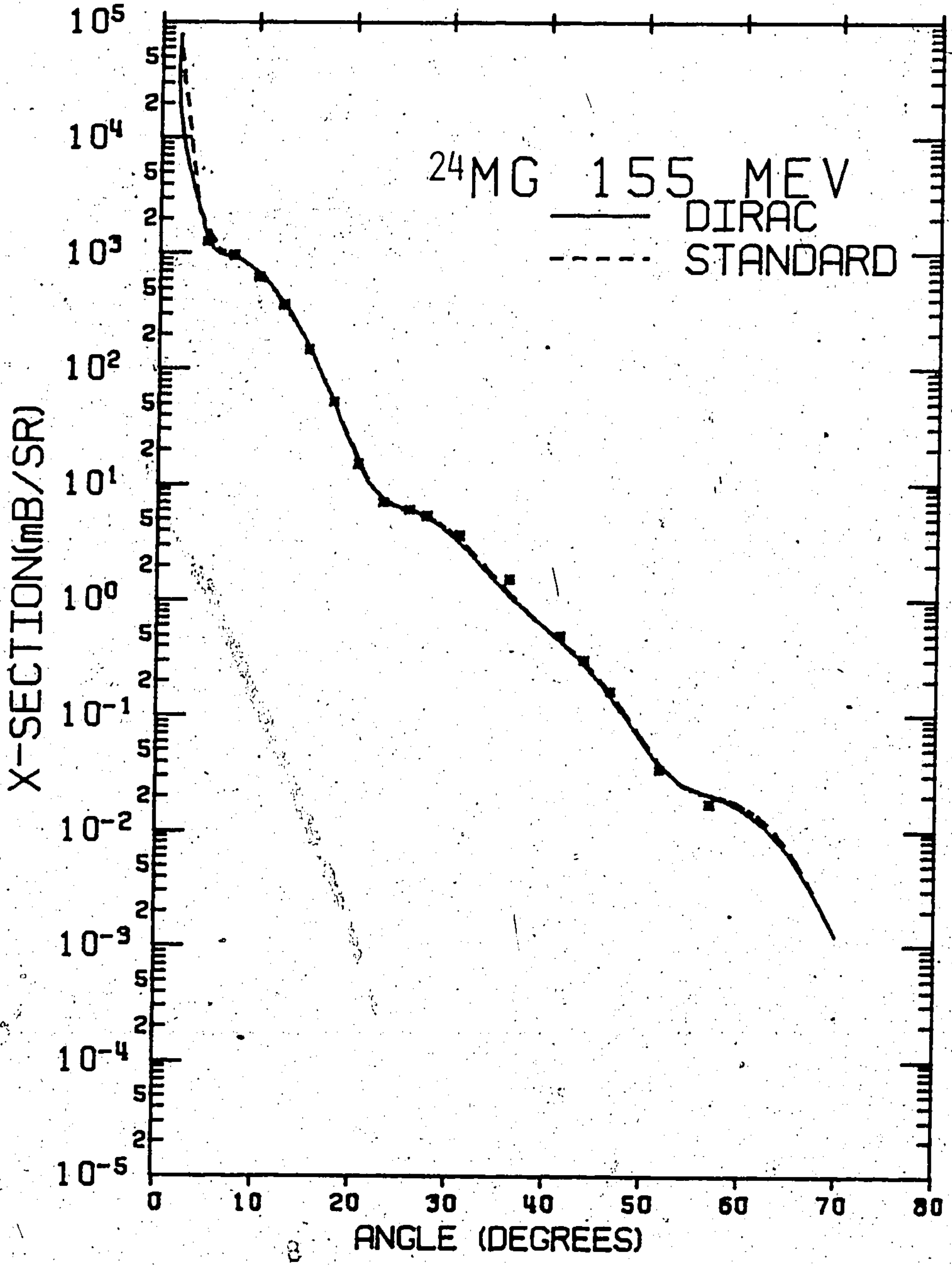

Figure 4 Differential cross-section for P + ^{24}Mg elastic scattering at E_p = 155 MeV. The solid curve is the DIRAC model and the dashed curve is the STANDARD model.

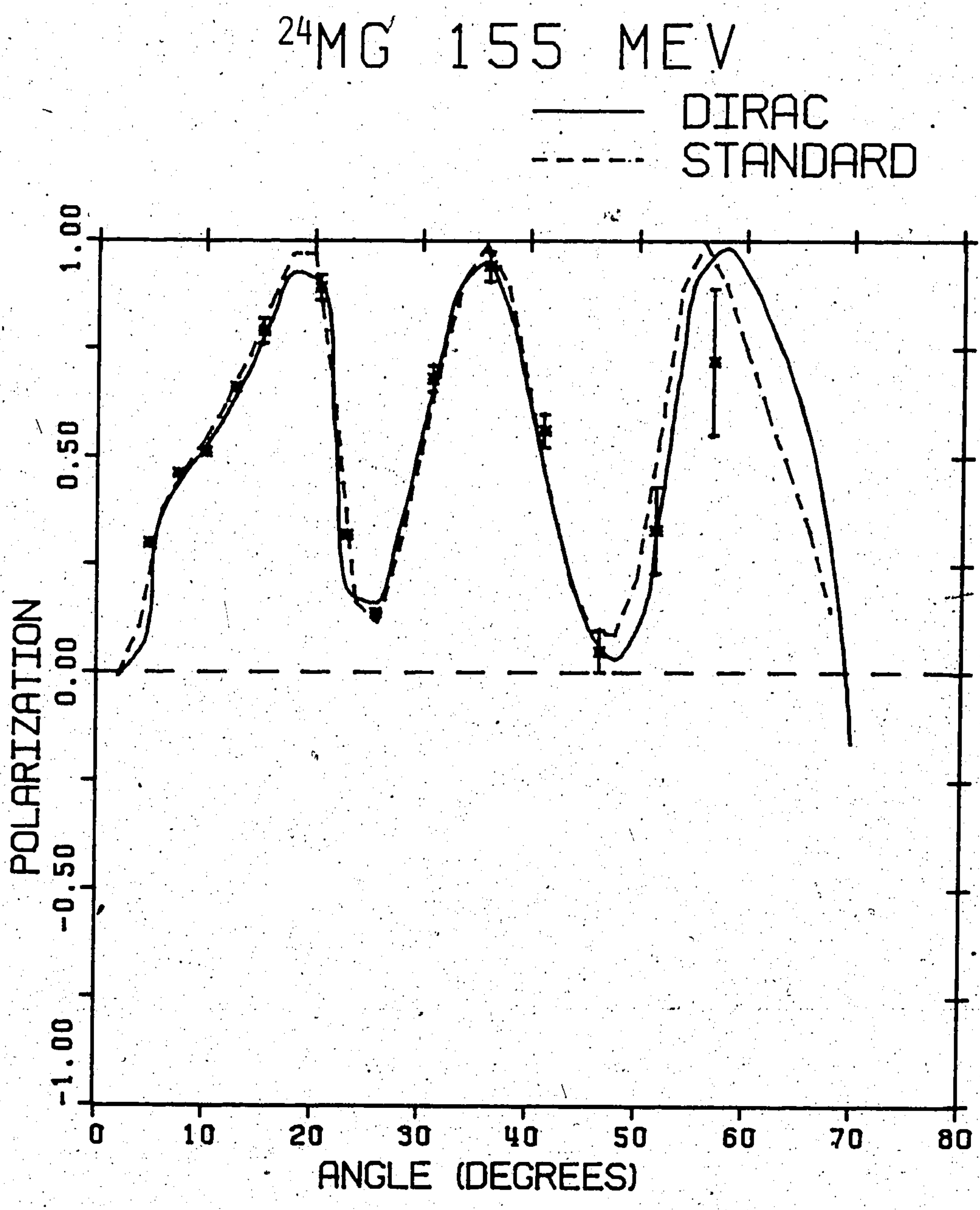

Figure 5 Polarization for P + ^{24}Mg elastic scattering at E_p = 155 MeV. The solid curve is the DIRAC model and the dashed curve is the STANDARD model.

from Willis et al. (Wi68). The fits according to the two models are nearly equivalent. The Dirac model is slightly in better agreement with the experiment for the elastic polarization. The reaction cross-section resulting from the calculations of the standard model equals 402.5 mb while that of the Dirac model equals 349.2 mb.

VI.3 ^{40}Ca

For calcium we have analysed the data from the four energies, 155 MeV, 181 MeV, 300 MeV and 500 MeV. We show the fits to the elastic scattering cross-section and polarization at 181 MeV, in figures 6 and 7. The data are from Ingemarsson et al. (In71). As the figures show the agreement between the two models in fitting the experimental data is very good. They are approximately equivalent. The reaction cross-section resulting from the calculations of the standard model equals 495.5 mb while that of the Dirac model equals 594.5 mb and the experimental value (Jo61) equals 524±14 mb.

VI.4 Potential Equivalence

It is known that the non-relativistic optical potentials, i.e. the potentials resulting from the standard model are energy dependent. The real central potential remains attractive as the energy increases, then turn repulsive at some energy. While the imaginary part remains attractive. The energy dependence comes out explicitly in the Dirac model (see equation (IV.20)). With increasing energy, the real central potential changes slowly from attractive to repulsive in the interior, resulting in the "Wine Bottle Bottom" shape, in the energy range 100-200 MeV. Figure 8 shows the real central potential for the case of $P + {}^{40}$Ca at 181 MeV, as it is predicted by both models, illustrating the above mentioned properties of this potential. Figure 9 shows the prediction of the imaginary central potential for the same case mentioned above.

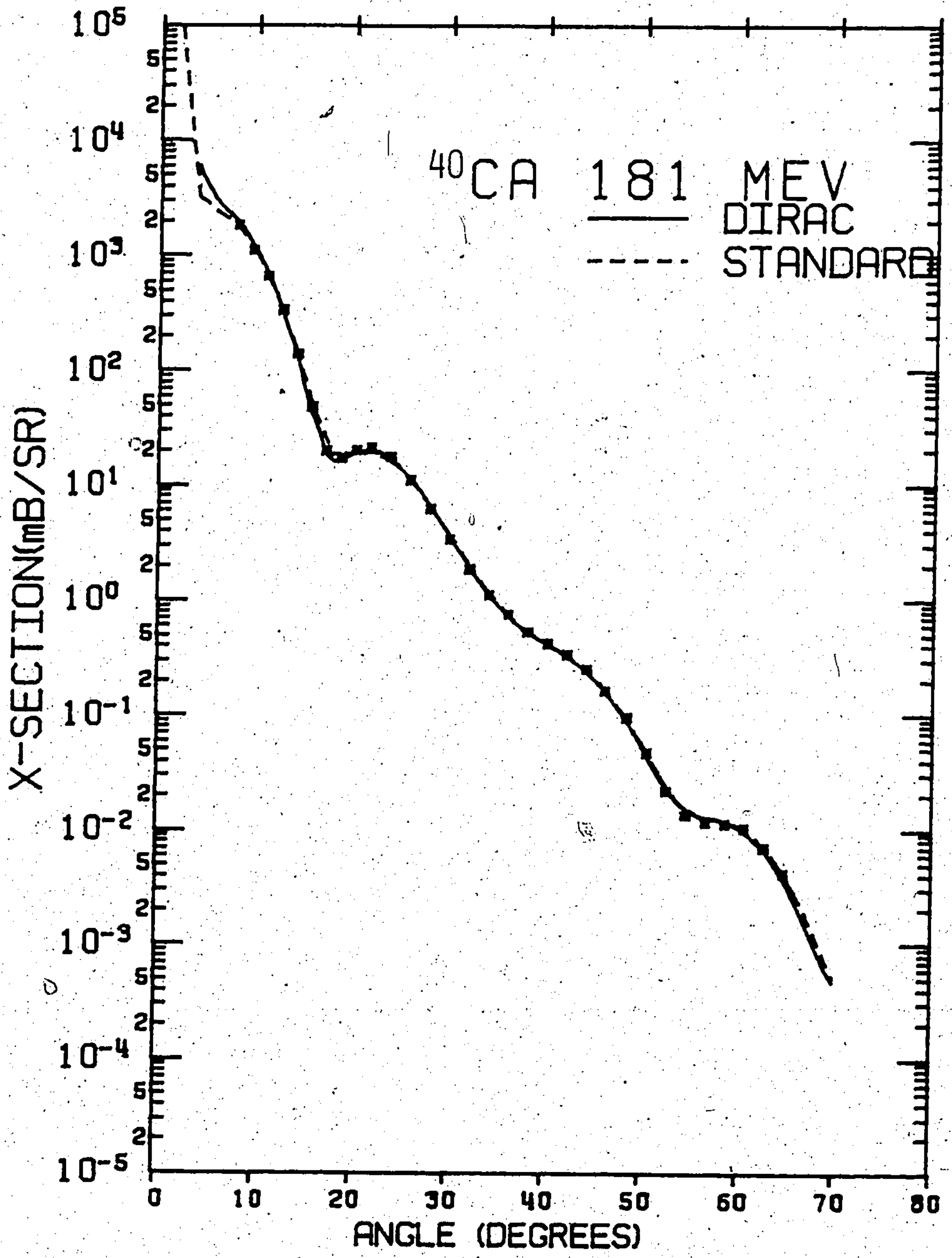

Figure 6 Differential cross-section for P + ^{40}Ca elastic scattering at E_p = 181 MeV. The solid curve is the DIRAC model and the dashed curve is the STANDARD model.

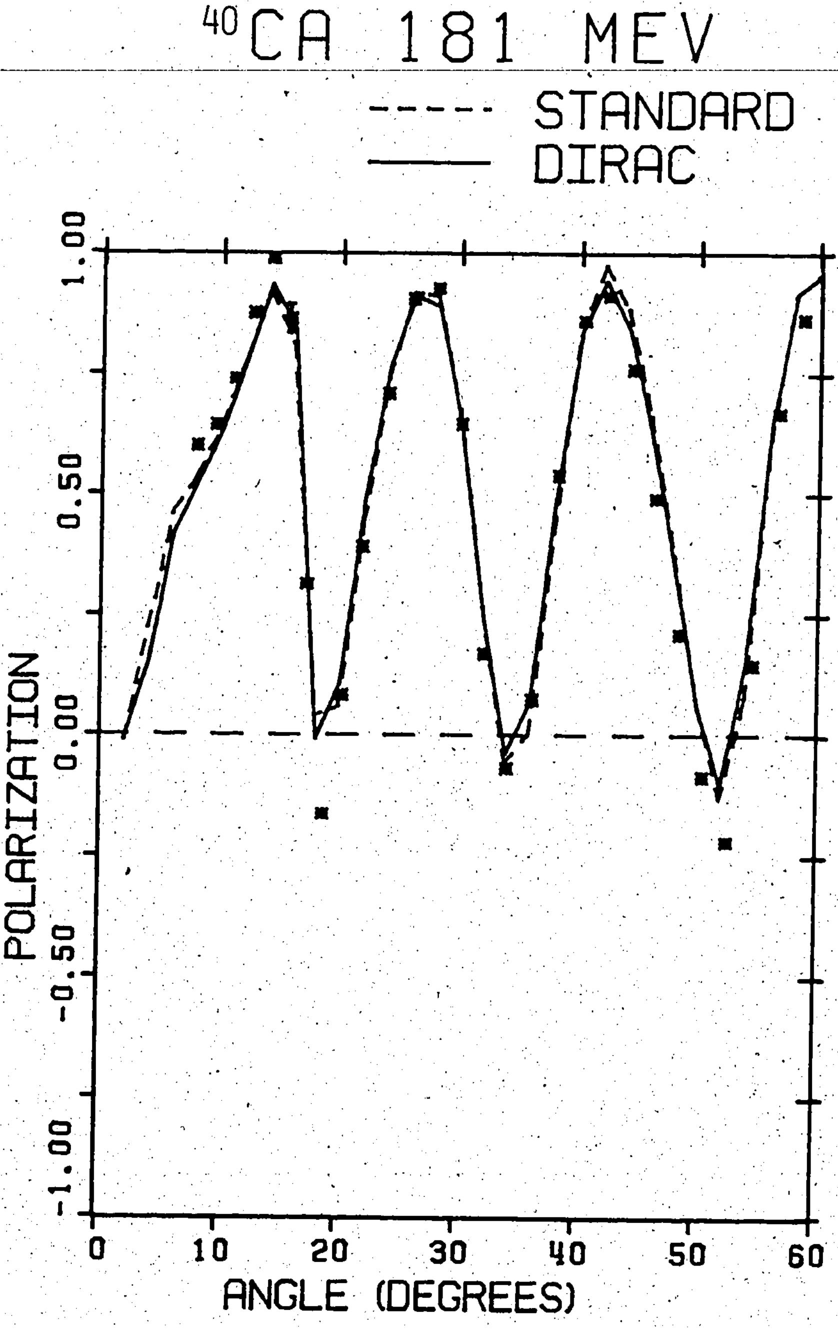

Figure 7 Polarization for P + ^{40}Ca elastic scattering at E_p = 181 MeV. The solid curve is the DIRAC model and the dashed curve is the STANDARD model.

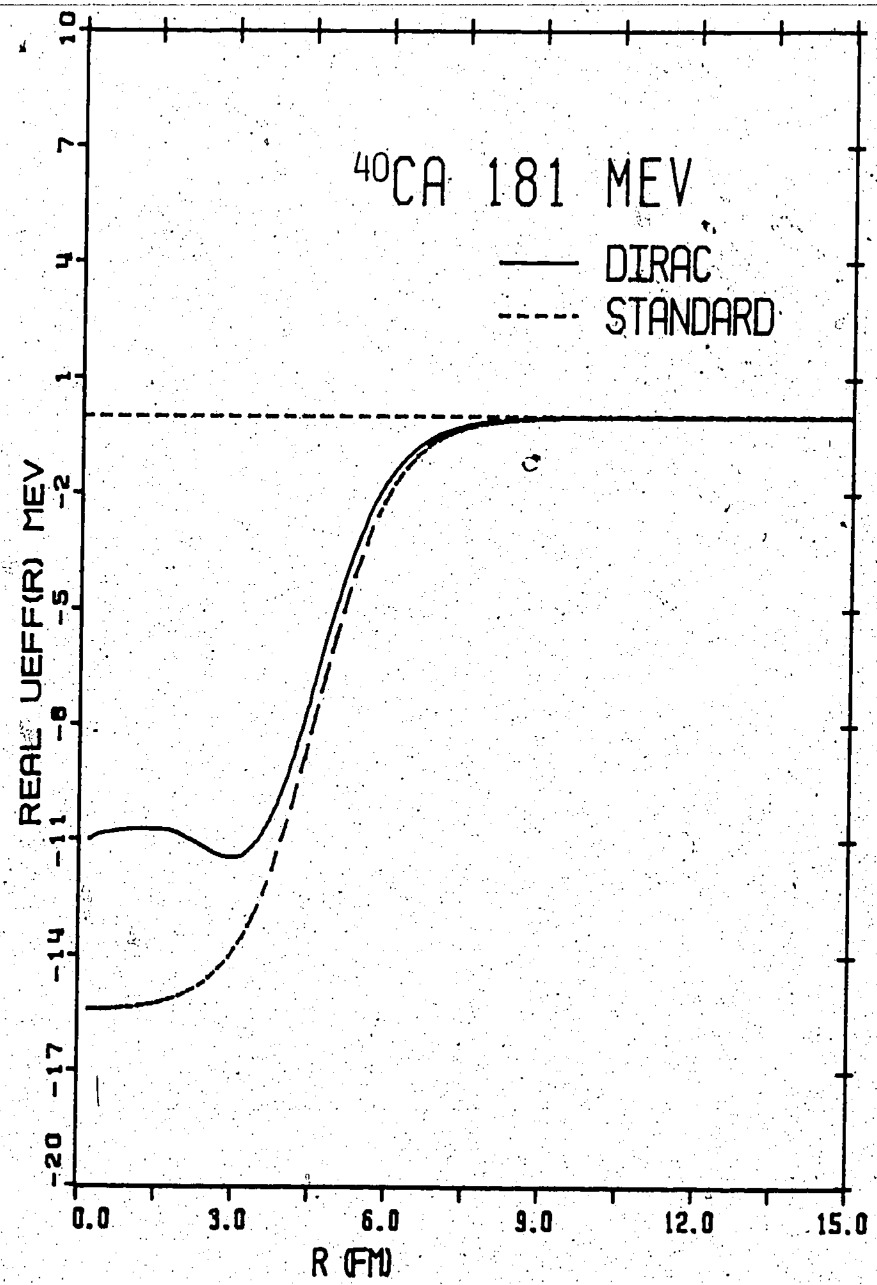

Figure 8 The real part of the central potential for P + ^{40}Ca at E_p = 181 MeV. The solid curve is the DIRAC model and the dashed curve is the STANDARD model.

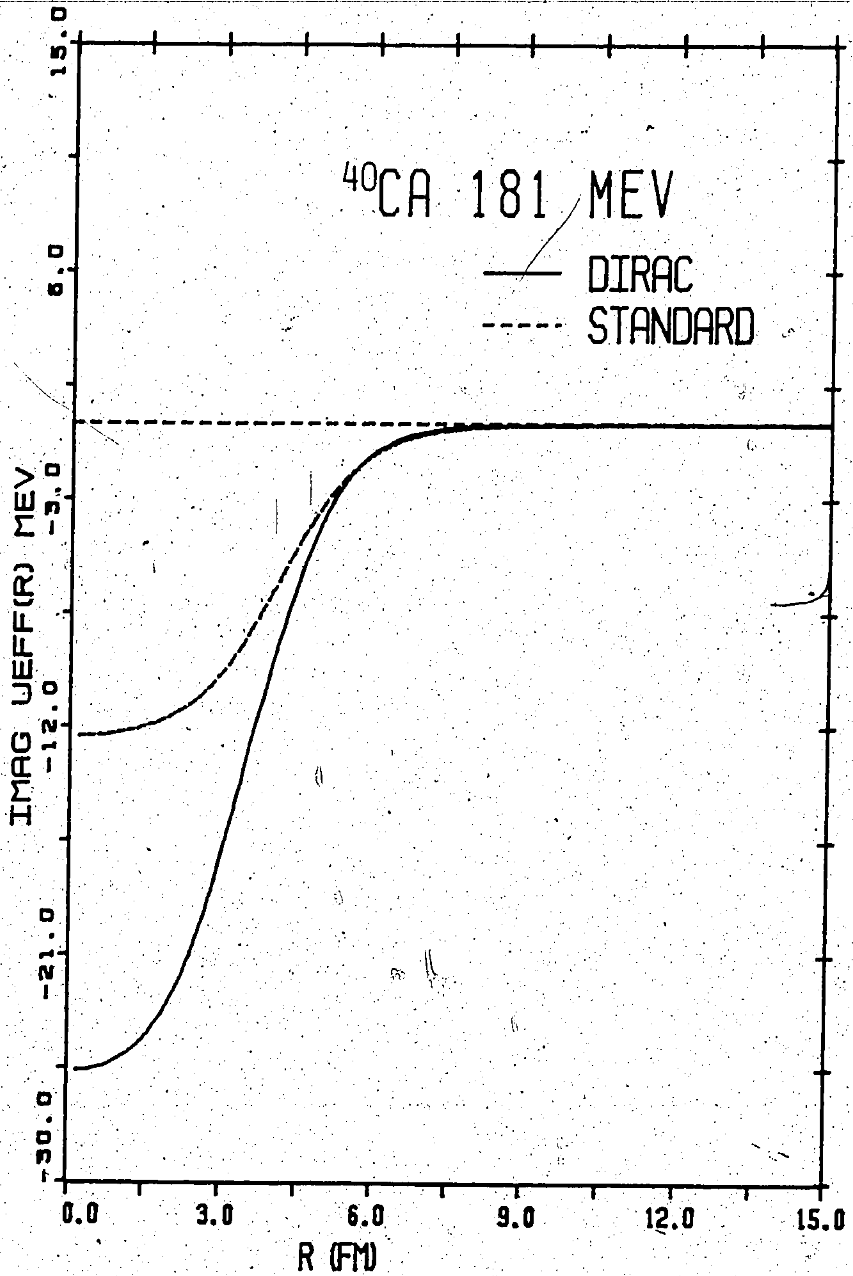

Figure 9 The imaginary part of the central potential for P + ^{40}Ca at E_p = 181 MeV. The solid curve is the DIRAC model and the dashed curve is the STANDARD model.

Note that the Dirac model prediction is much deeper than that of the Standard model. In fact the imaginary central potential gets deeper as energy increases.

The spin-orbit potentials also have some energy dependence, but it is much smaller than that of the central potential. This too comes about as a result of the energy dependent denominator of equation (IV.21). In figures 10 and 11, we show both the real and imaginary spin-orbit potentials as predicted by both models. We can see that the predictions for the real spin-orbit potential of both models have the same general shape with only a slight difference in magnitude. For the imaginary part, on the other hand, the difference in magnitude gets larger. The Standard model prediction is higher than that of the Dirac model by a factor of nearly 3.

Finally one can say that the two potentials (the Standard and the Dirac models) do differ in shape, particularly near 200 MeV, but inspite of this fact they still can be regarded as equivalent, since they give reasonably good agreement with the data at this energy range. This accord may not hold beyond this energy range due to the inability of the Standard model to provide an equivalent fit to the experimental data as that of the Dirac model.

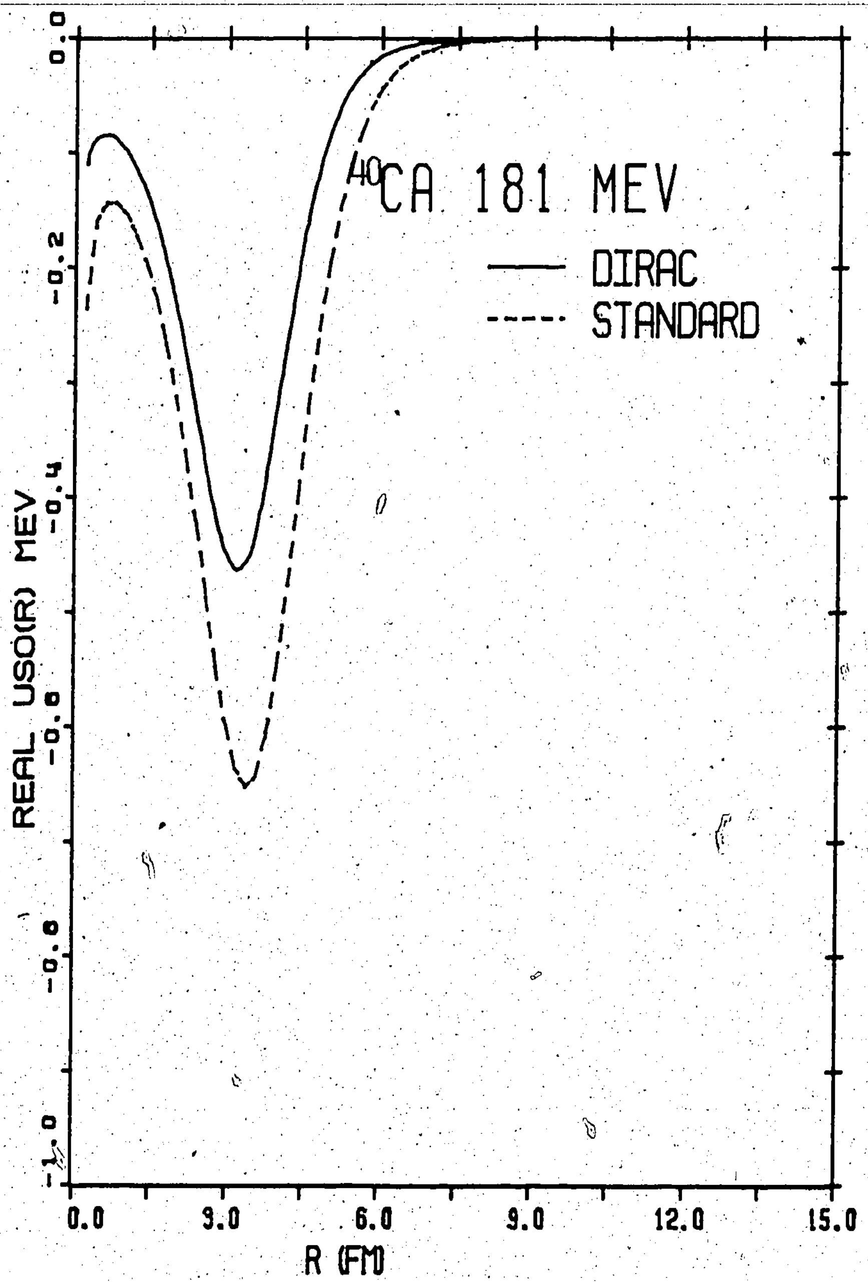

Figure 10 The real part of the spin orbit potential for P + ^{40}Ca at E_p = 181 MeV. The solid curve is the DIRAC model and the dashed curve is the STANDARD model.

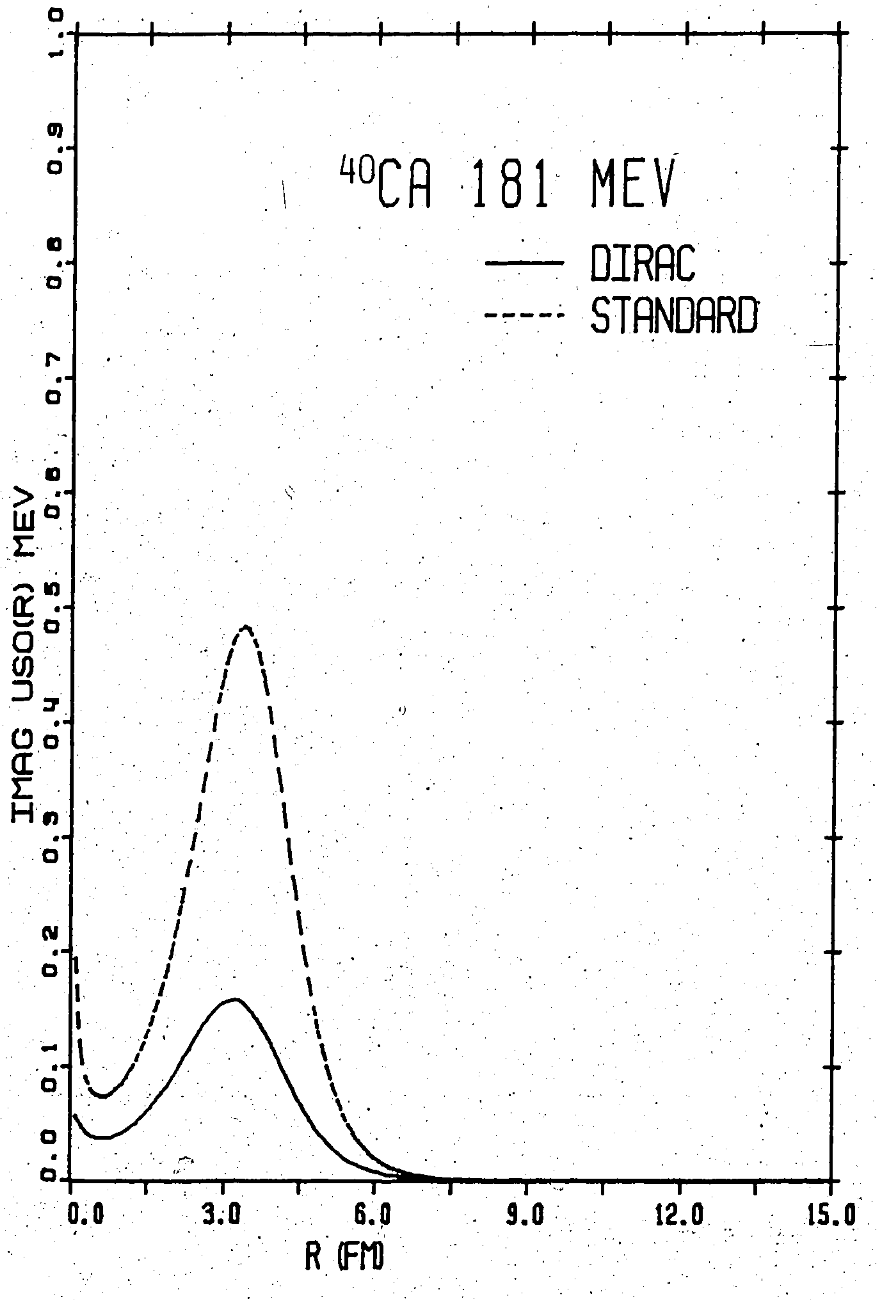

Figure 11 The imaginary part of the spin orbit potential for P + ^{40}Ca at E_p = 181 MeV. The solid curve is the DIRAC model and the dashed curve is the STANDARD model.

VII. INELASTIC SCATTERING

In the preceding chapter we have shown comparisons between the Standard model and the Dirac model for some elastic scattering data. In this chapter we shall carry out a discussion about the extended optical model potential and its applications in inelastic scattering. In particular, we are interested in finding out whether the near equivalence of the 'Standard' and 'Dirac' models for elastic scattering does extend to the case of inelastic scattering. In other words, we wish to investigate the impact, on inelastic scattering, of the differences in potentials associated with the two models, particularly in the region near 200 MeV.

We use the extended Standard model in a non-relativistic distorted wave Born approximation (DWBA) calculation for proton inelastic scattering. We have used a DWBA code (Sh68) for this purpose, which is based on the formalism given in chapter III. The only adjustable parameter in this calculation is the deformation parameter (β). We have used equal deformation length (βR) in our calculations, since it gives better prediction for the polarization than using equal deformation parameters (see below).

We have modified the (DWBA) code mentioned above to carry out similar calculation for inelastic scattering based on the Dirac model. Three more subroutines were added to the code to calculate the relativistic kinematics, the Dirac equation based "equivalent" potentials and their associated form factors. The formalisms of these calculations are given in chapters IV and V. We have also used equal deformation lengths for all parts of the potentials for the same reason mentioned above. For the purpose of comparisons between the two models, we have used the same deformation length in both cases.

Figures 12 to 17 show comparisons of the inelastic scattering form factors for the excitation of the 3^- state at 3.73 MeV in ^{40}Ca at 181 MeV. It is clear that for the real central form factor (figure 12) there is a difference between the predictions of the two models in the interior, reflecting the Wine Bottle Bottom shape in the Dirac model. Figure 13 shows that the imaginary central form factor is much stronger in the Dirac model but has the same shape except at very short distance. This feature could be explained by relating it to the fact that the imaginary central potential in the Dirac model is much deeper than that of the Standard model.

The spin-orbit potential was deformed and included in the calculation. In the present analysis we use the full Thomas form (Sh68a) for the deformed spin-orbit potential. Spin-orbit 1 refers to the spin-orbit term in equation (III.27) and its counterpart in equation (V.29), while spin-orbit 2 refers to the spin-orbit term in equation (III.28) and its counterpart in equation (V.30). We note from figures (14) to (17) that the spin-orbit form factors in the two models are similar in shape but vary in magnitude near peaks and minima.

We have found that the effect of including spin-orbit deformation in the transition potential on the calculated cross-section is important. This is contrary to what Satchler (Sa83) had expected; namely that the effect will not be appreciable in the energy range near 200 MeV. Figures 18 and 19 show an illustration for the above mentioned effect calculated using both the Standard and the Dirac models for the case of inelastic scattering on ^{40}Ca at 181 MeV. We can see that the differences are appreciable, they are present, both in the magnitude of the peak in the cross-section and in the angular distribution itself.

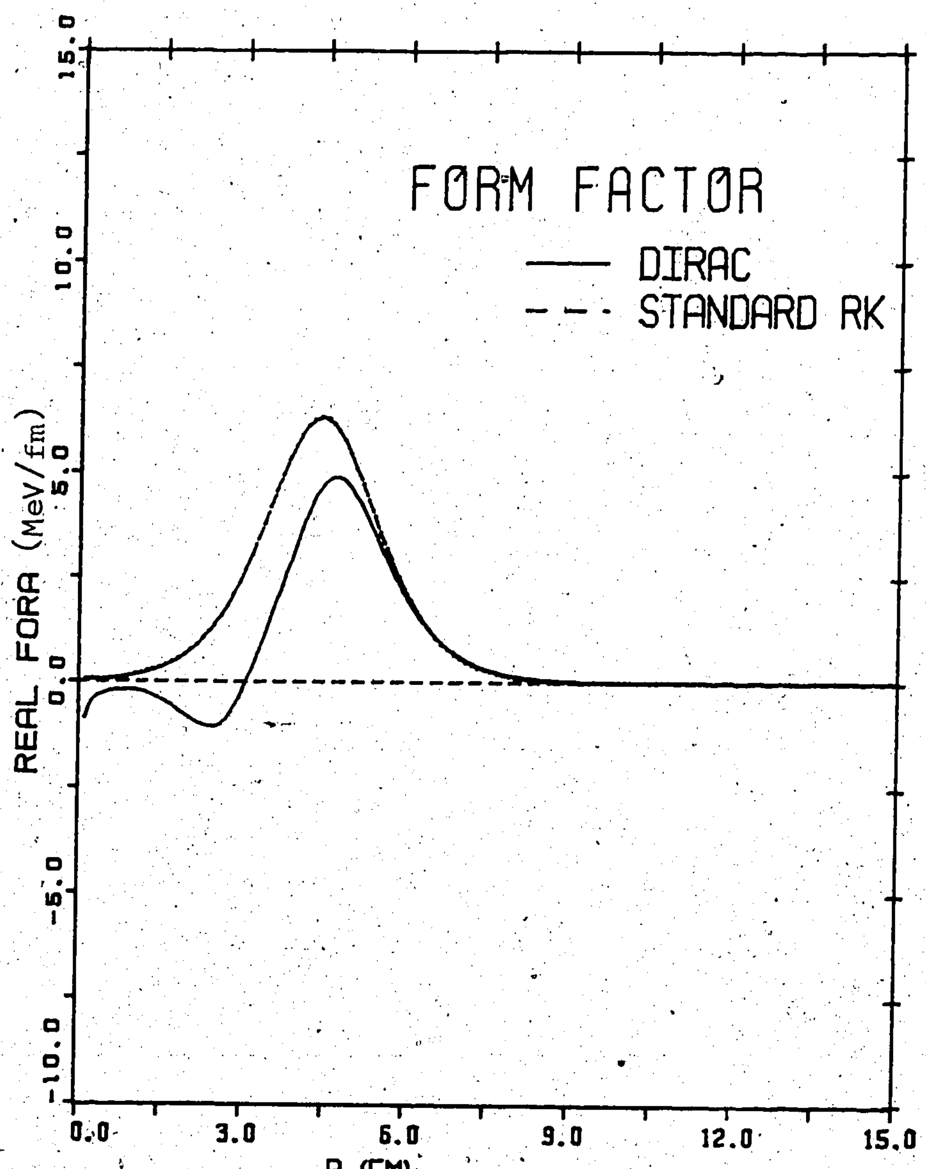

Figure 12 The real part of the central radial form factor for P + ^{40}Ca at E_p = 181 MeV. The solid curve is the DIRAC model and the dashed curve is the STANDARD model.

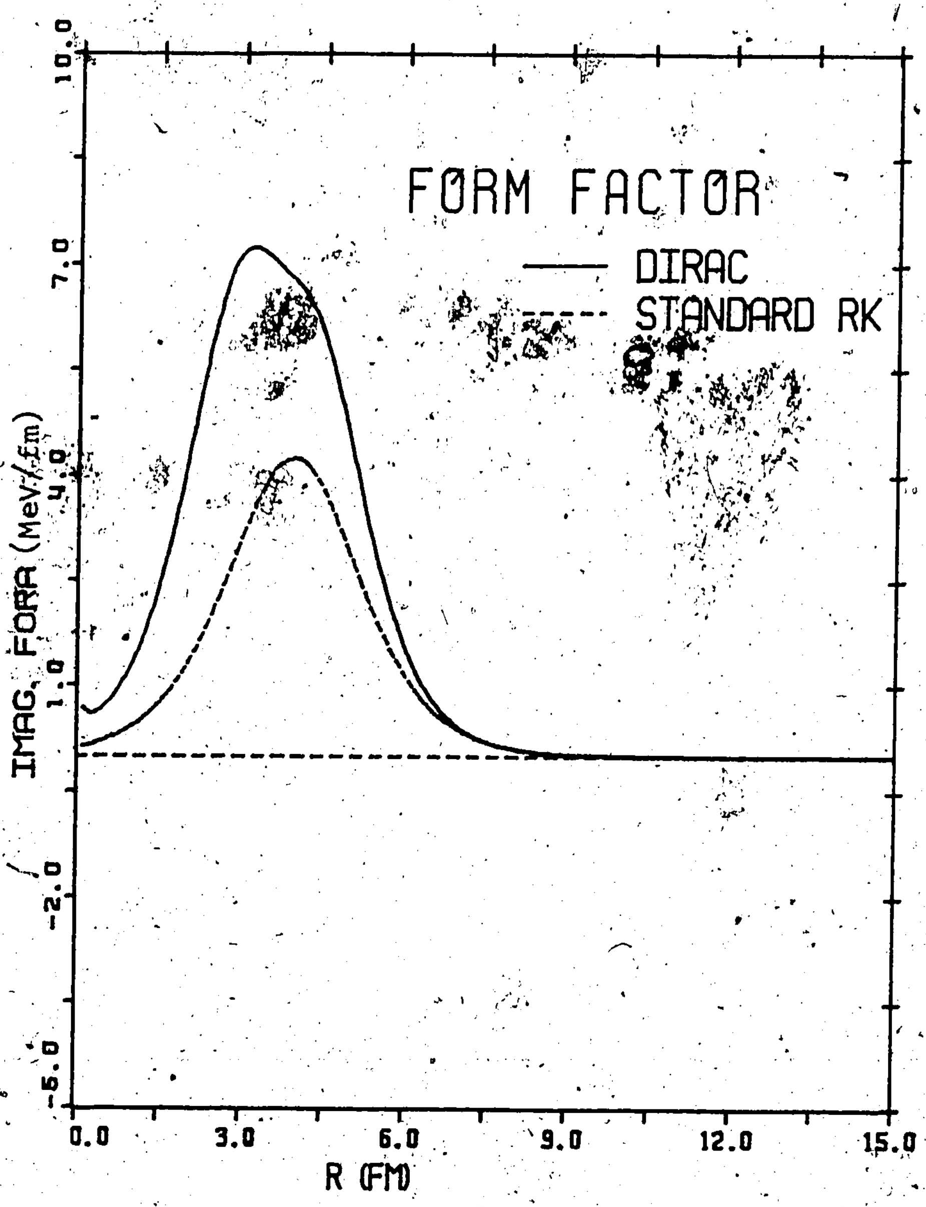

Figure 13 The imaginary part of the central radial form factor for P + ^{40}Ca at E_p = 181 MeV. The solid curve is the DIRAC model and the dashed curve is the STANDARD model.

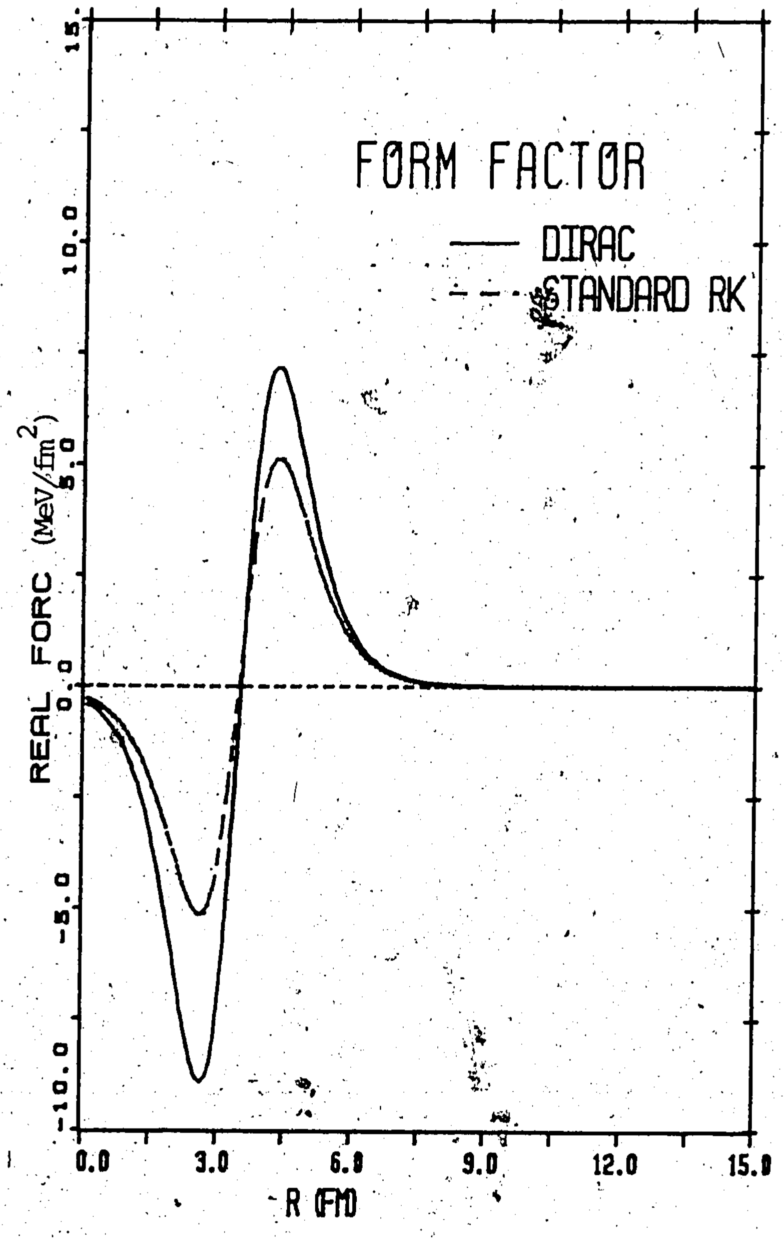

Figure 14 The real part of spin orbit 1 form factor for P + ^{40}Ca at E_p = 181 MeV. The solid curve is the DIRAC model and the dashed curve is the STANDARD model.

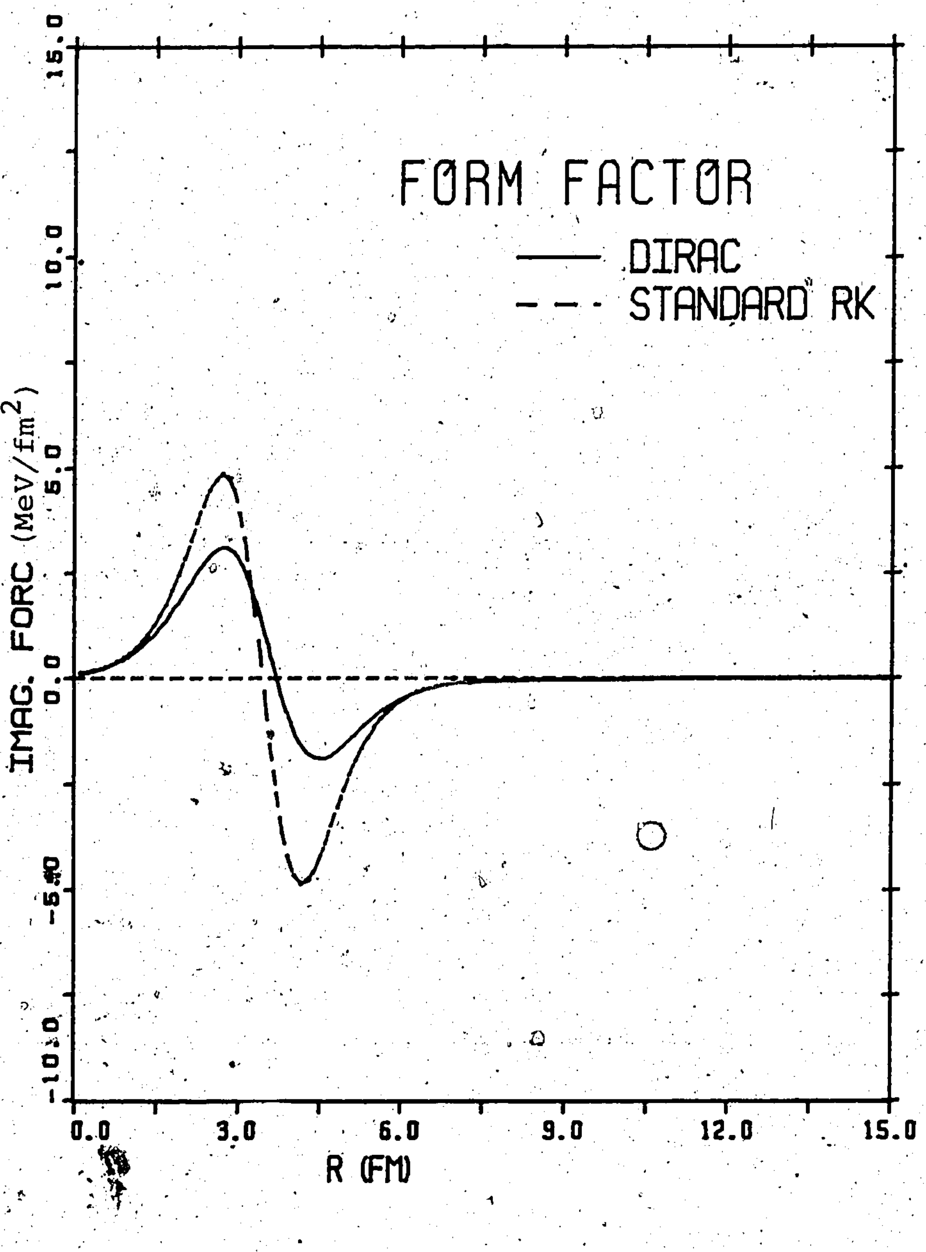

Figure 15 The imaginary part of spin orbit 1 form factor for P + ^{40}Ca at E_p = 181 MeV. The solid curve is the DIRAC model and the dashed curve is the STANDARD model.

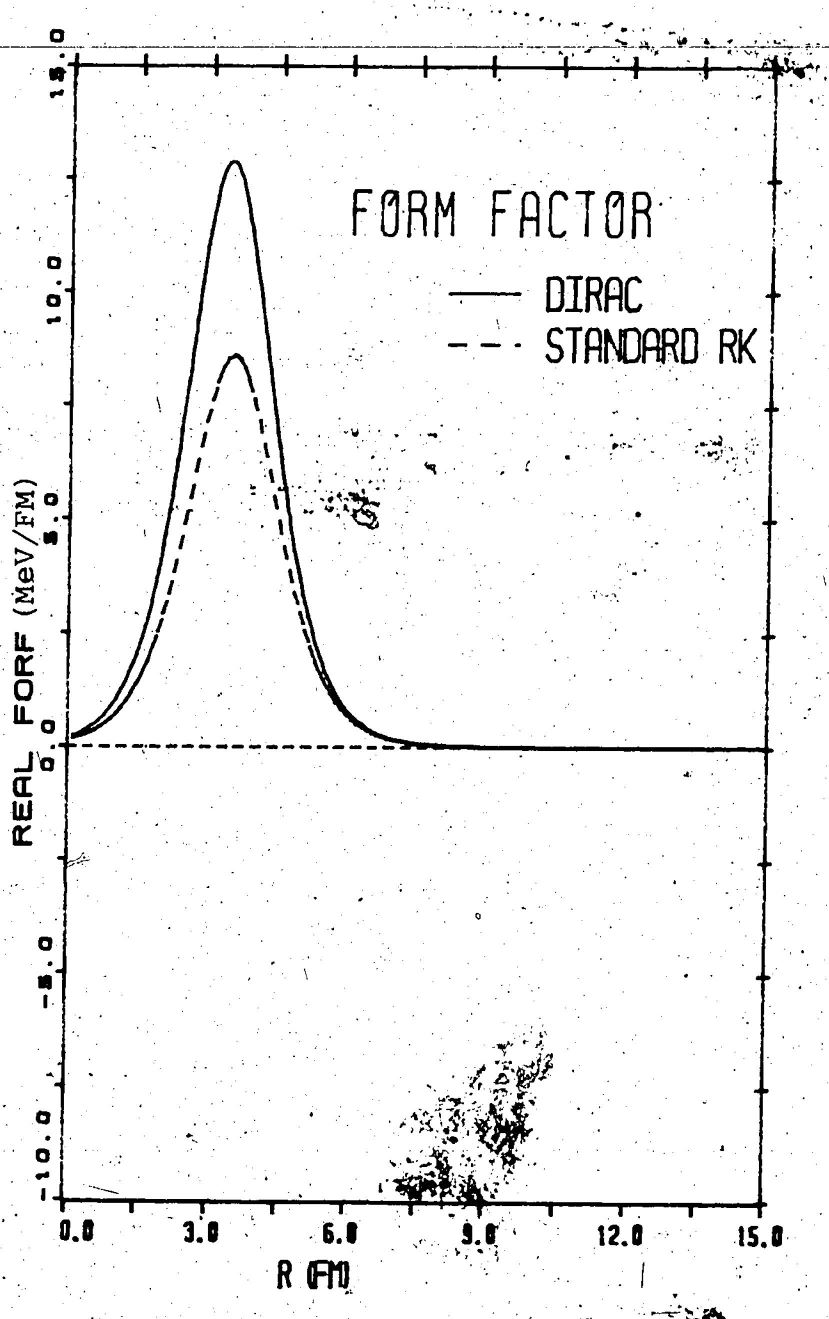

Figure 16 The real part of spin orbit 2 form factors for P + ^{40}Ca at E_p = 181 MeV. The solid curve is the DIRAC model and the dashed curve is the STANDARD model.

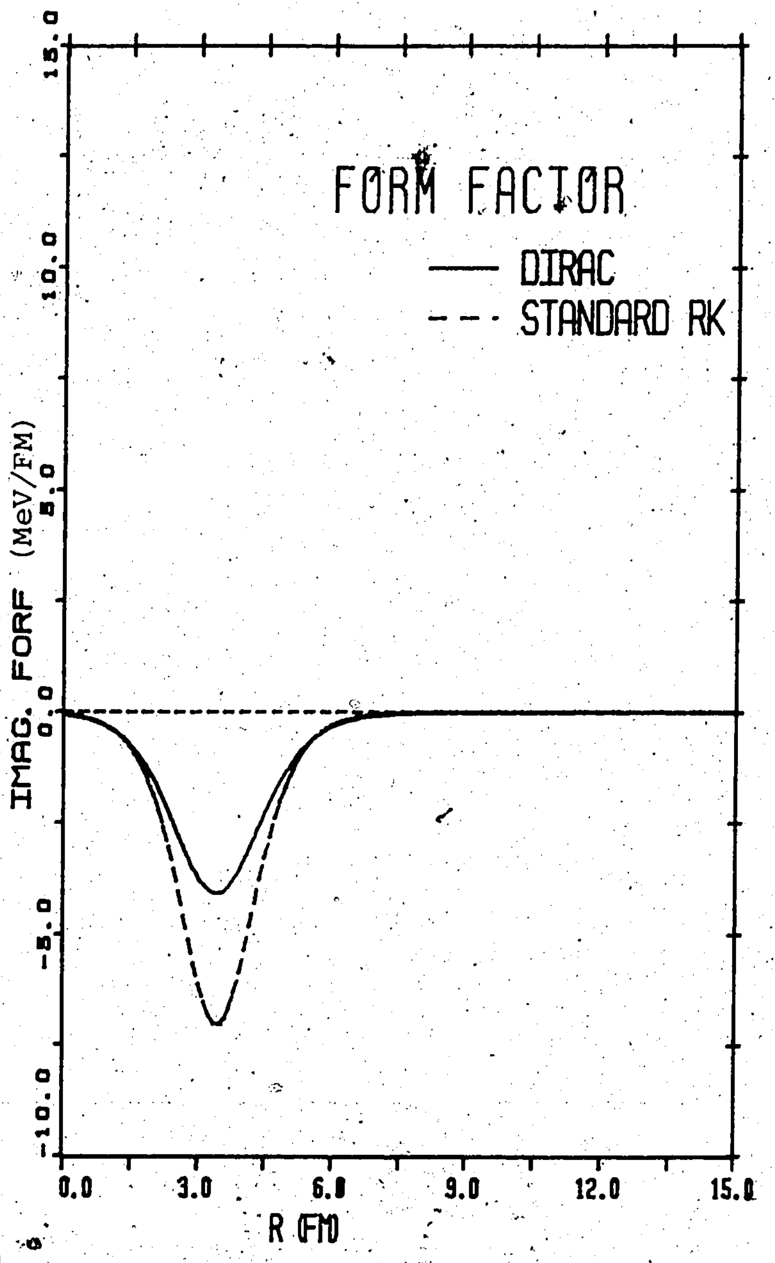

Figure 17 The imaginary part of spin orbit 2 form factor for P + ^{40}Ca at E_p = 181 MeV. The solid curve is the DIRAC model and the dashed curve is the STANDARD model.

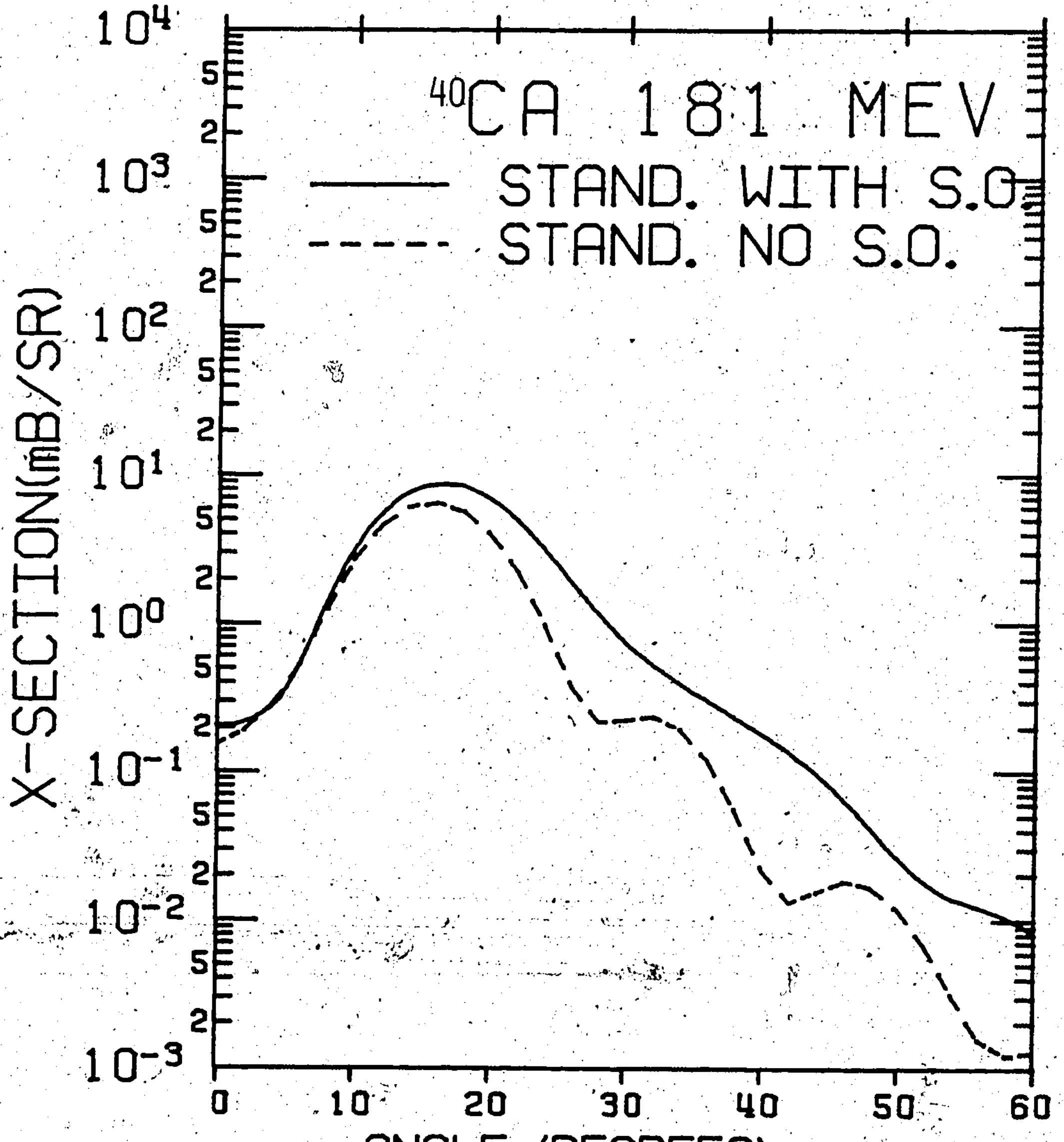

Figure 18 The effect of the deformed spin orbit term on the calculated cross-section. The calculations are the standard model predictions for ^{40}Ca (3$^-$ state, E_x = 3.73 MeV) at E_p = 181 MeV.

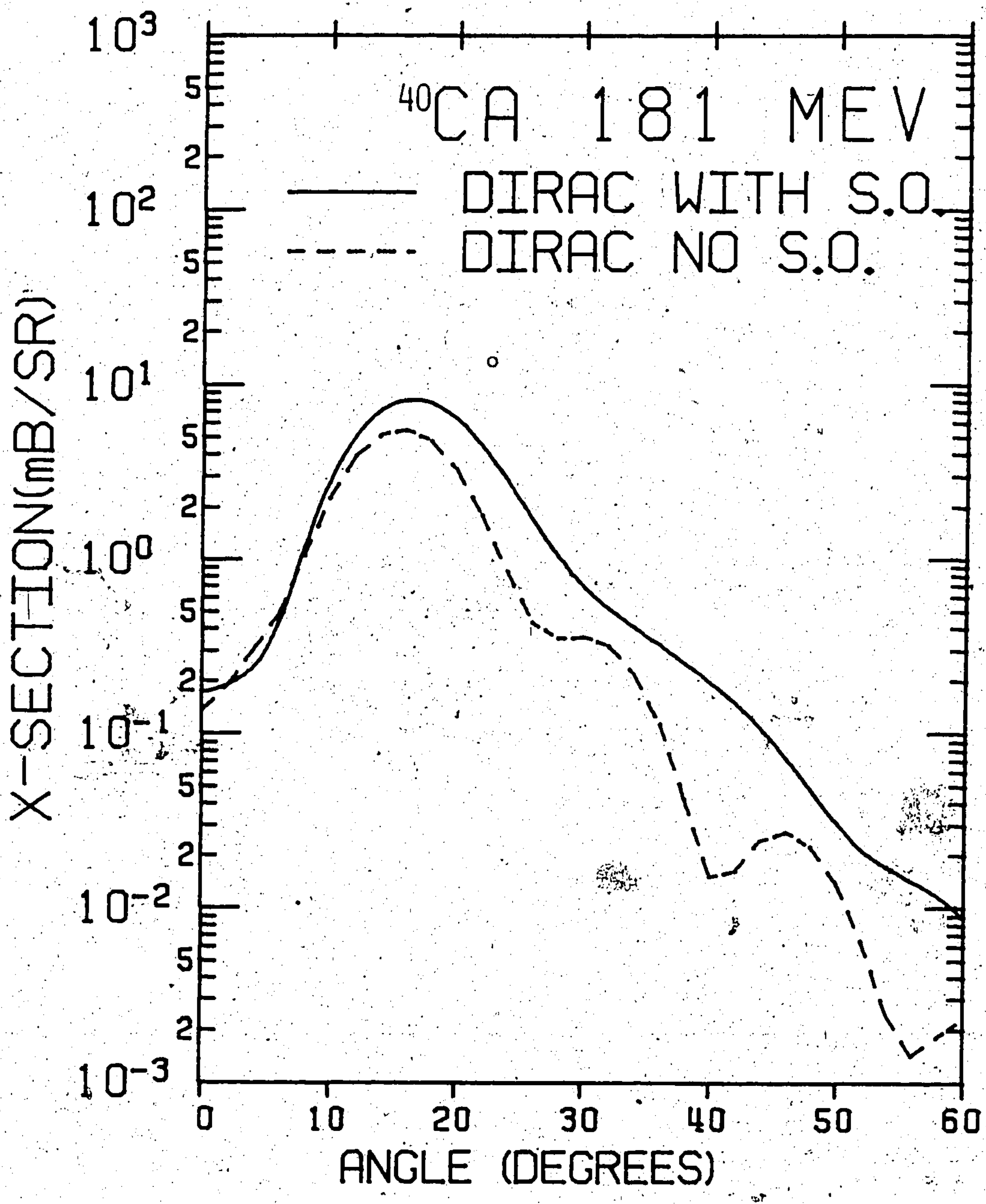

Figure 19 The effect of the deformed spin orbit term on the calculated cross-section. The calculations are the DIRAC model predictions for ^{40}Ca (3^- state, E_x = 3.73 MeV) at E_p = 181 MeV.

The prediction of the two models for the cross-section drops off more rapidly and oscillates more sharply as the angle increases. Besides these observations, it is known that the spin-orbit deformation is important and crucial in the calculation of inelastic polarization.

Below we will discuss some other effects on the calculations namely the effects of using equal deformation length, the effects of the kinematics and the effects of Coulomb deformations.

VII.1 The Effect of Using Equal Deformation Length.

We have done the calculations of the Standard model with equal deformation parameter β, which means all parts of the form factors get multiplied by the same number β, then we repeated the whole calculations with equal deformation length βR, which means that all parts of the form factors get multiplied by βR_o where R_o is the radius of the real part of the central potential. We have found that the prediction of the Standard model for the proton inelastic polarization is in better agreement with experimental data when equal deformation length βR is used. So we have considered the calculations of both models with equal deformation length βR in our analysis, and we kept βR equal for both models for purposes of comparison.

VII.2 The Effect of Kinematics.

We have studied the role of kinematics in the close accord between the predictions of the two models. We have carried out the entire Standard model calculations with non-relativistic and with relativistic kinematics. We have compared the results and we found that there are minor differences and one can say that the two types of calculations are basically the same at the energy range of 200 MeV, aside from a

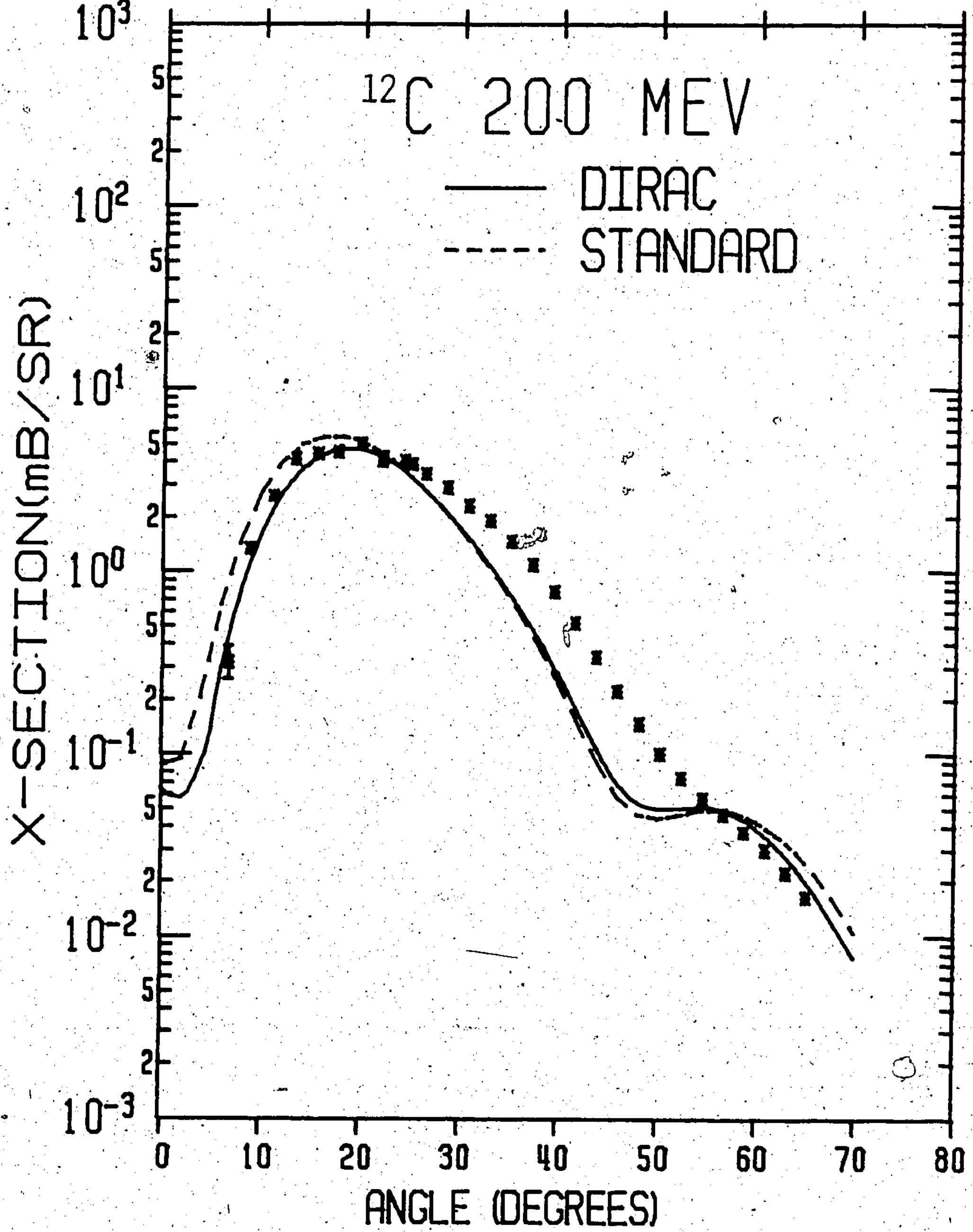

Figure 20 Differential cross-section for P + ^{12}C inelastic scattering (2^+, E_x = 4.43 MeV) at E_p = 200 MeV. The solid curve is the DIRAC model and the dashed curve is the STANDARD model.

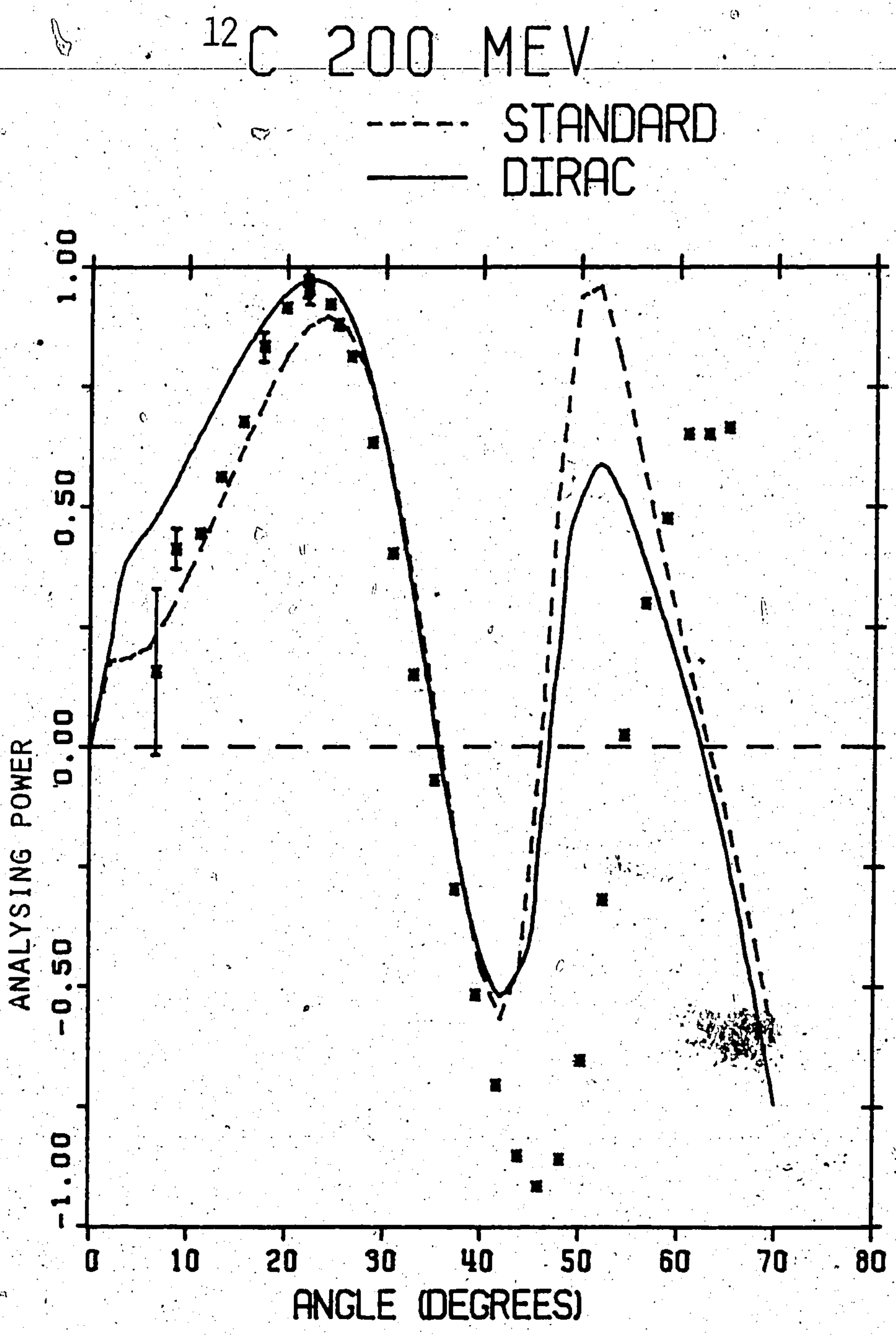

Figure 21 Analysing power for P + ^{12}C inelastic scattering (2^- state, E_x = 4.43 MeV) at E_p = 200 MeV. The solid curve is the DIRAC model and the dashed curve is the STANDARD model.

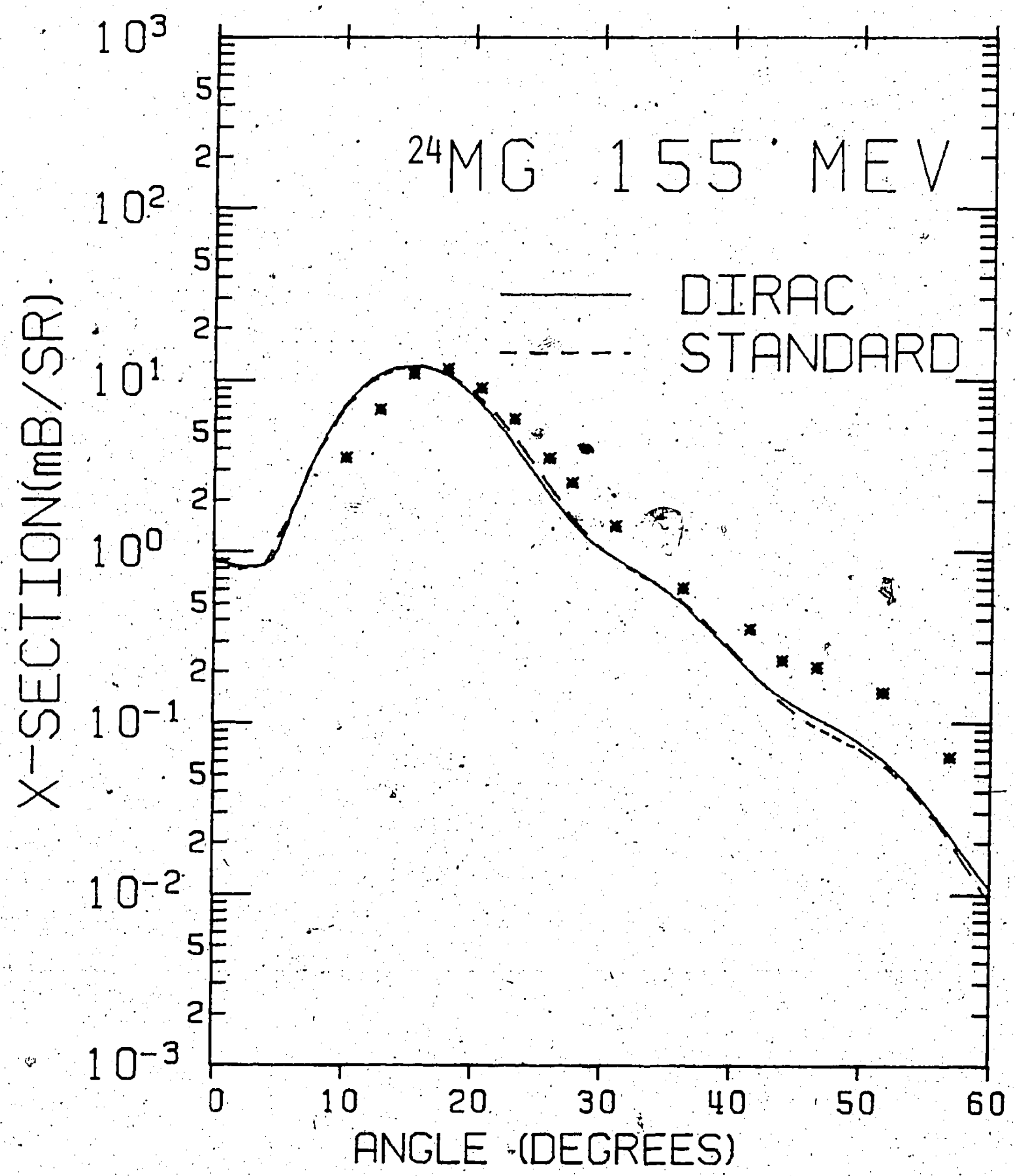

Figure 22 Differential cross-section for P + ^{24}Mg inelastic scattering (2^+ state, E_x = 1.37 MeV) at E_p = 155 MeV. The solid curve is the DIRAC model and the dashed curve is the STANDARD model.

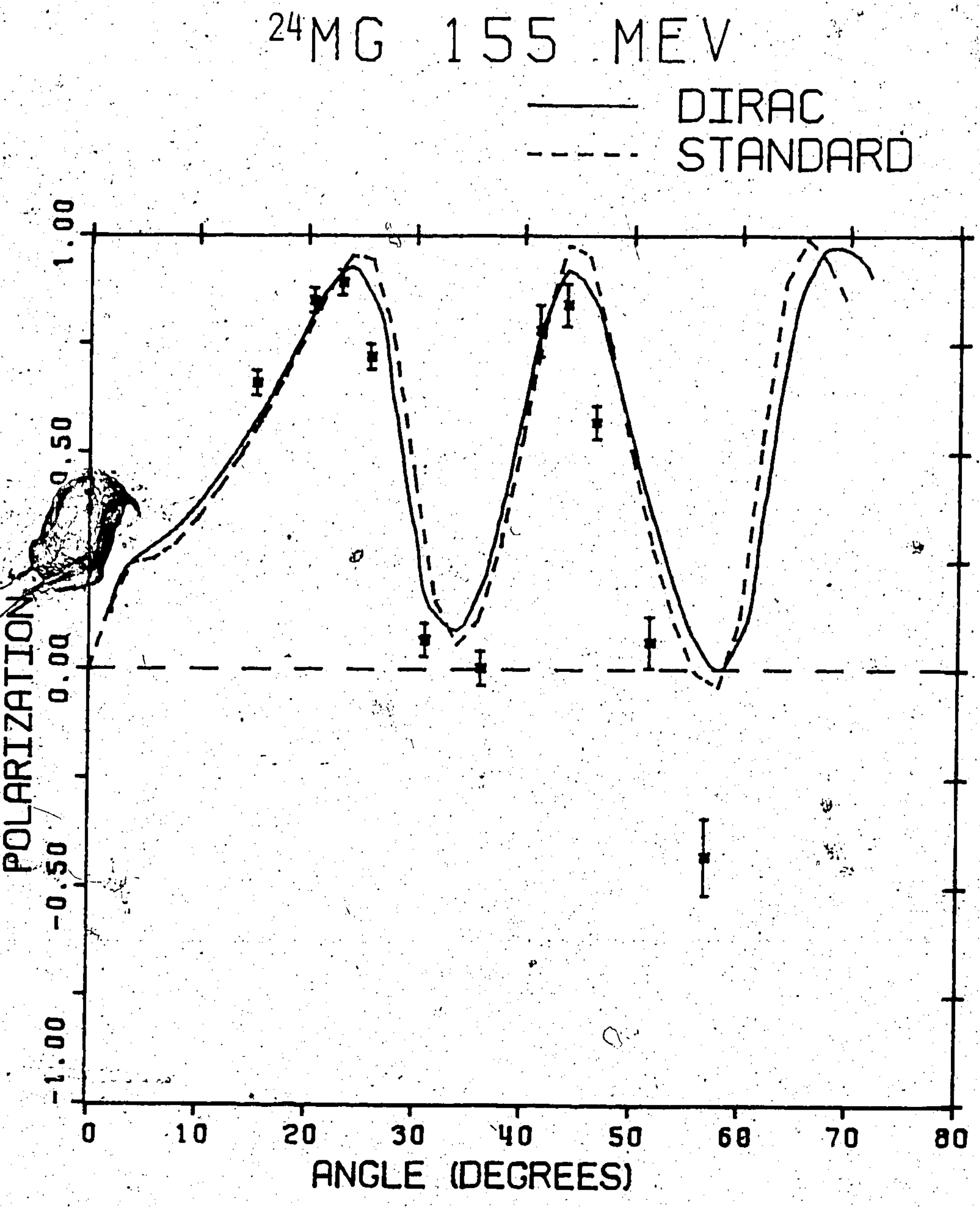

Figure 23 Polarization for P + ^{24}Mg inelastic scattering (2^+ state, E_x = 1.37 MeV) at E_p = 155 MeV. The solid curve is the DIRAC model and the dashed curve is the STANDARD model.

slight change in normalization.

VII.3 The Effect of Coulomb Deformation.

We have also studied the effects of including the deformation of the Coulomb potential, and we have found that the effects are very small and do not affect the calculations except for ^{208}Pb. We have, therefore, left these effects out of the calculations for both models.

Below we will show comparisons between the predictions of the Dirac model and the Standard model, as well as compare these to the experimental results whenever available.

VII.4 $^{12}C(p,p')^{12}C^{*}$ 2^{+} State (Ex = 4.43 MeV) at Ep = 200 MeV.

Figures 20 and 21 show the prediction of the two models for both inelastic cross-section and analysing power. The agreement between the two types of calculations is satisfactory. The agreement with the experimental data is not that good but it is comparable with other analyses (Me81). The Dirac model is in slightly better agreement with the data especially at forward angles. The data are from (Me81). We have normalized the Dirac calculations to the experimental data, then we extracted $\beta = 0.60$, and 0.439 for the Dirac model and the Standard model, respectively, and $\beta R = 1.30$ F for both models. If we normalize the Standard model calculations to the data we get $\beta = 0.56$ and 0.41 for the Dirac model and the Standard model, respectively with $\beta R = 1.21$ F for both models.

VII.5 $^{24}Mg(p,p')^{24}Mg^{*}$ 2^{+} State (Ex = 1.37 MeV) at Ep = 155 MeV.

Figures 22 and 23 show comparisons between the predictions of the Standard model and the Dirac model for inelastic scattering cross-section and polarization, and the experimental data. The data are from

(Wi68). The agreement between the prediction of the two models is satisfactory. They do predict the general shape of the experimental data. We have used equal deformation length in both models, ($\beta R = 1.364$ fm), where $\beta = 0.34$ for the Standard model while $\beta = 0.482$ for the Dirac model. Sherif (Sh68), in his analysis of the same case using the Standard model obtained $\beta = 0.353$ and $\beta R = 1.30$ fm.

VII.6 $^{32}S(p,p')^{32}S^*$ 2^+ State (Ex = 2.24 MeV) at Ep = 155 MeV.

Figures 24 and 25 show comparisons between the predictions of the Standard and the Dirac models for the inelastic cross-section and polarization. We also show the experimental data of Willis et al. (Wi68) for comparison. The agreement between the two types of calculations is very good. Where the agreement between the calculations and the experimental data is quite good for the inelastic cross-section over the whole angular range (i.e. up to $\theta = 60°$) while it is good for the polarization only up to $\theta = 40°$. We get a deformation parameter $\beta = 0.23$ for the Standard model and $\beta = 0.31$ for the Dirac model and a $\beta R = 1.033$ F for both models. From previous analyses for the same case, Sherif (Sh68) obtained $\beta = 0.24$ and $\beta R = 1.15$ F while Haybron (Ha66) got a fit to another set of data using collective model DWBA without spin-orbit deformation and obtained $\beta = 0.29$ and $\beta R = 1.12$ F.

VII.7 $^{40}Ca(p,p')^{40}Ca^*$ 3^- State (Ex = 3.73 MeV) at Ep = 181 MeV.

Figures 26 and 27 show the predictions of the two models for both inelastic cross-section and polarization comparing them with the experimental data. The data are from (In71). The agreement between the predictions of the two models is very good. The results of the present work are superior to that of Satchler (Sa83) in fitting the experimental

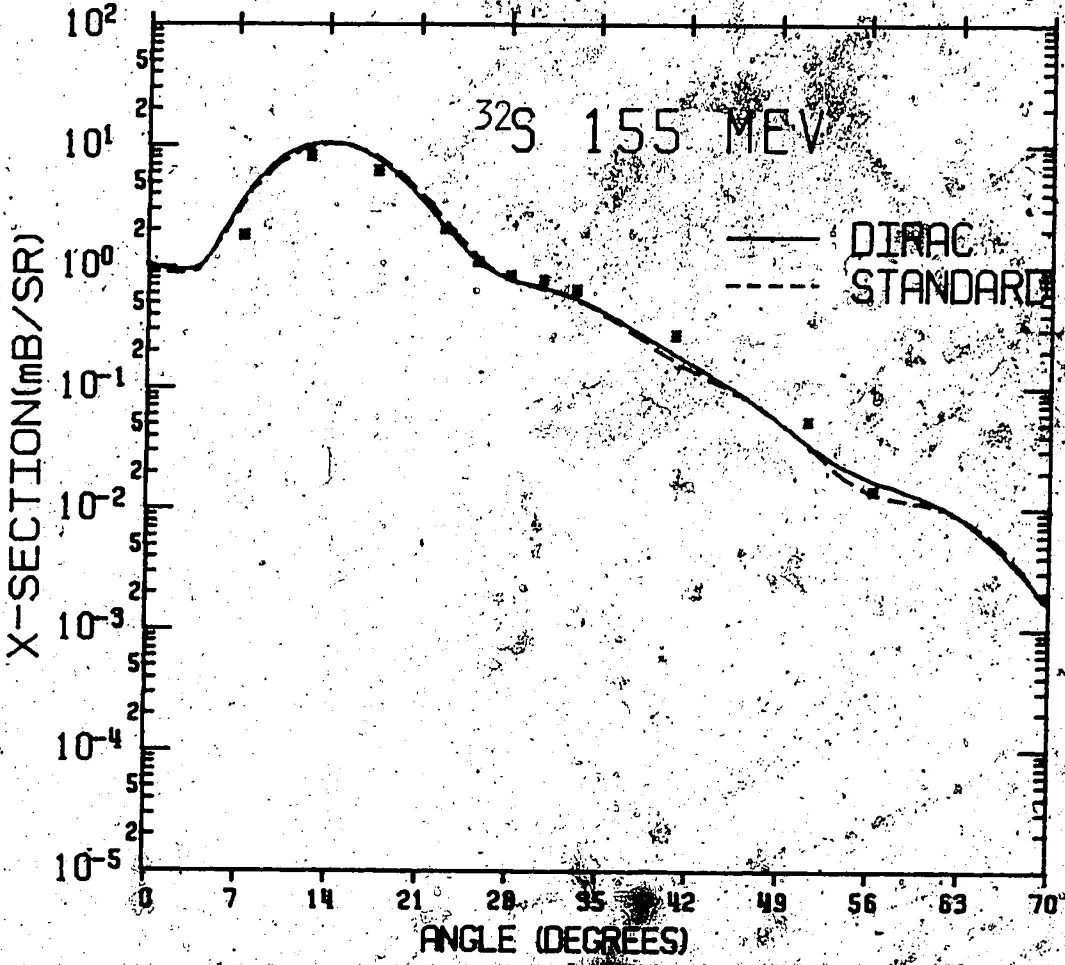

Figure 24. Differential cross section for P + ^{32}S inelastic scattering (2^+ state, $E_x = 2.24$ MeV) at $E_p = 155$ MeV. The solid curve is the DIRAC model and the dashed curve is the STANDARD model.

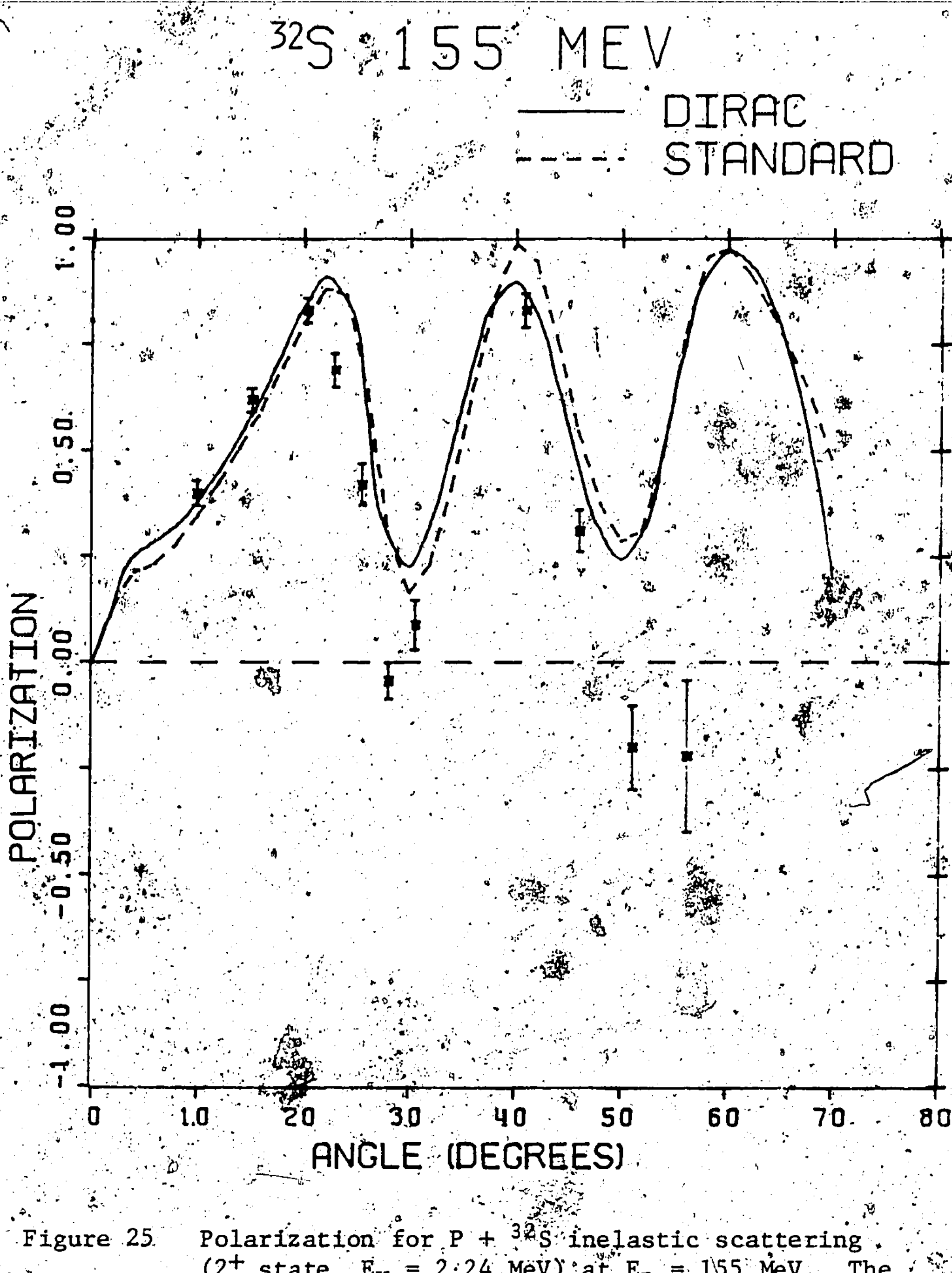

Figure 25 Polarization for P + ^{32}S inelastic scattering (2^+ state, E_x = 2.24 MeV) at E_p = 155 MeV. The solid curve is the DIRAC model and the dashed curve is the STANDARD model.

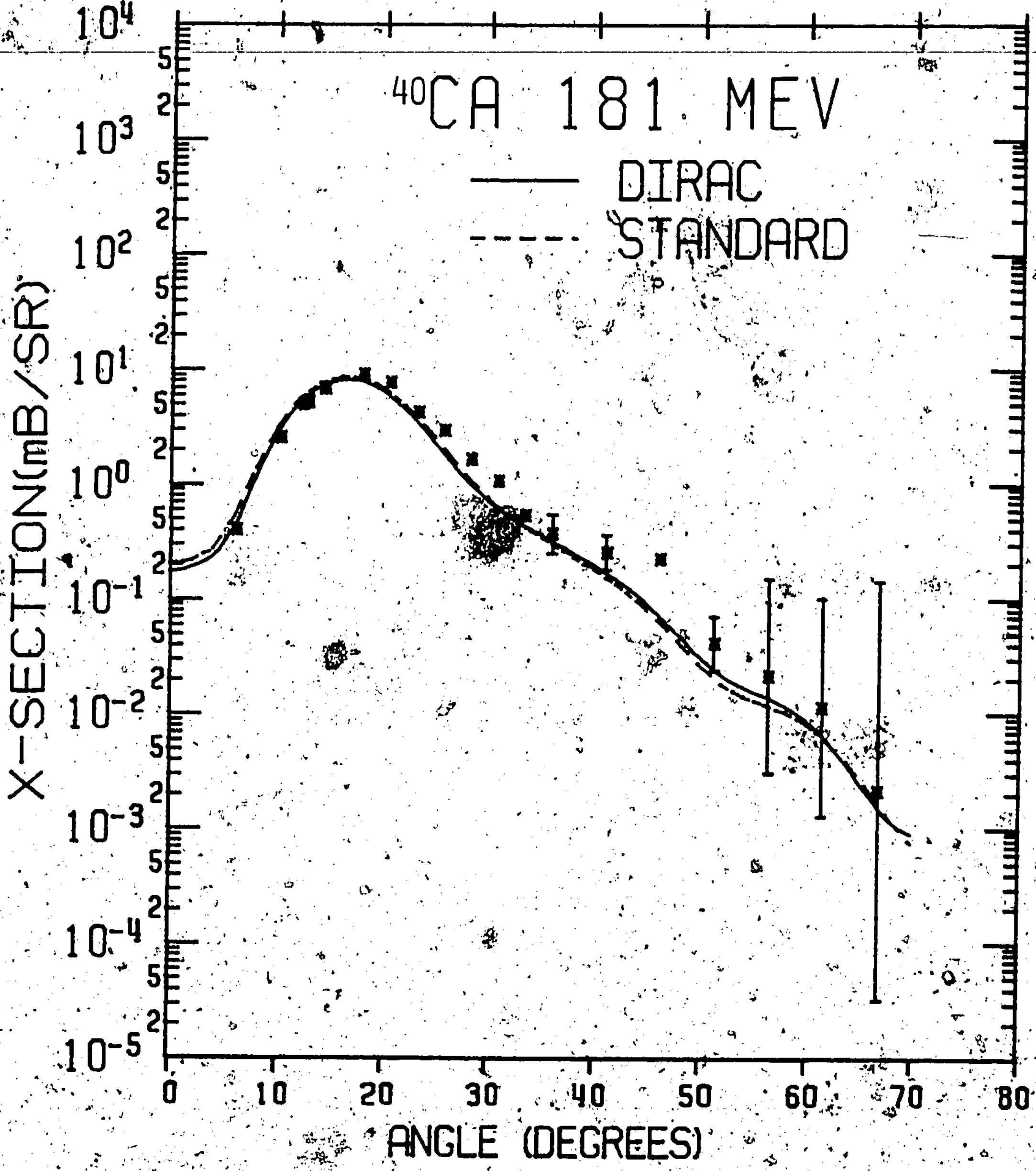

Figure 26 Differential cross-section for P + ^{40}Ca inelastic scattering at E_p = 181 MeV. The solid curve is the DIRAC model and the dashed curve is the STANDARD model.

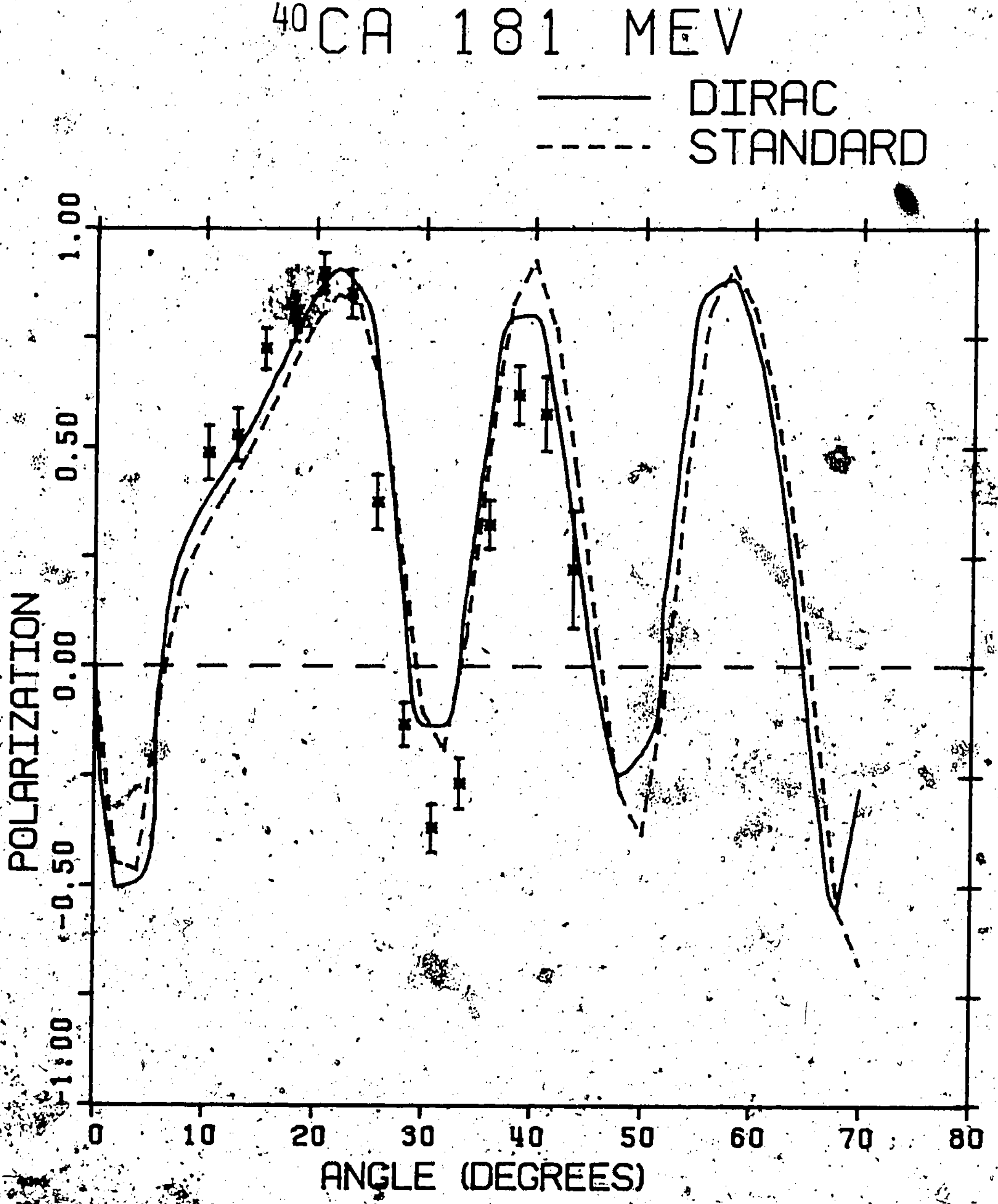

[illegible] 27 Polarization for P + ^{40}Ca inelastic scattering (3^- state, E_x = 3.73 MeV) at E_p = 181 MeV. The solid curve is the DIRAC model and the dashed curve is the STANDARD model.

data, since he neglected the effects of the deformed spin-orbit potential which were shown to be important for this energy range. We get a deformation parameter $\beta = 0.23$ for the Standard model, $\beta = 0.285$ for the Dirac model and hence $\beta R = 1.014$ F for both models. Satchler (Sa83) used equal deformation parameter $\beta = 0.35$ in his analysis and $\beta R = 1.464$ and 1.398 F for the W-S model and the WBB model respectively. If we carry out our calculations without including the effect of the deformed spin-orbit interaction we get $\beta = 0.27$ and $\beta = 0.336$ for the Standard model and the Dirac model respectively and $\beta R = 1.19$ F for both of them. The ratio of the peak cross-section of the Standard model to that of the Dirac model with and without including the spin-orbit interaction in the calculation is 1.093 and 1.168 respectively if we use equal deformation length. If we use equal deformation parameter $\beta = 0.27$ for the calculations without including the spin-orbit the ratio will be 1.81, where according to Satchler (Sa83) the ratio will be 2 if we use equal deformation parameter (β), and 1.5 if we use equal deformation length (βR).

VII.8 ^{40}Ca(p,p')^{40}Ca* 2^{+} State (Ex = 18 MeV) at Ep = 181 MeV.

Figures 28 and 29 show the predictions of both models for inelastic scattering and polarization. We don't have experimental data for this case to compare with the theoretical calculations, but we note that the two models are in good agreement. We have used $\beta = 0.23$ for the Standard model and $\beta = 0.285$ for the Dirac model and $\beta R = 1.014$ F for both models. Satchler (Sa83) used $\beta = 0.254$ for both W-S and WBB models and $\beta R = 1.094$ F for the W-S model and 0.981 for the WBB model. The peak cross-section for the Standard model is 15.57 mb/sr while it is 12.75 mb/sr for the Dirac model. Satchler (Sa83) obtained a value of

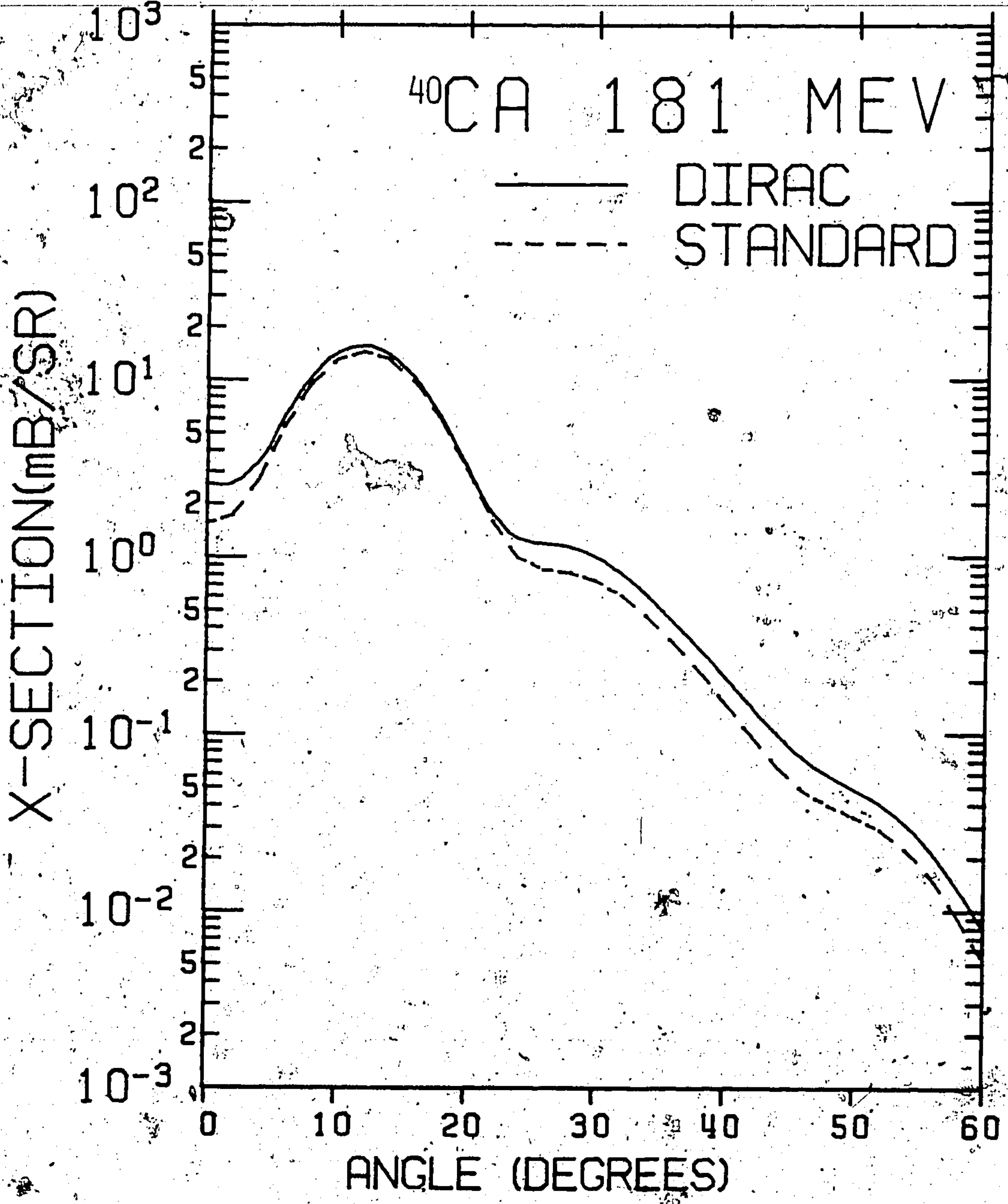

Figure 28 Differential cross-section for P + ^{40}Ca inelastic scattering (2^+ state, E_x = 18 MeV) at E_p = 181 MeV. The solid curve is the DIRAC model and the dashed curve is the STANDARD model.

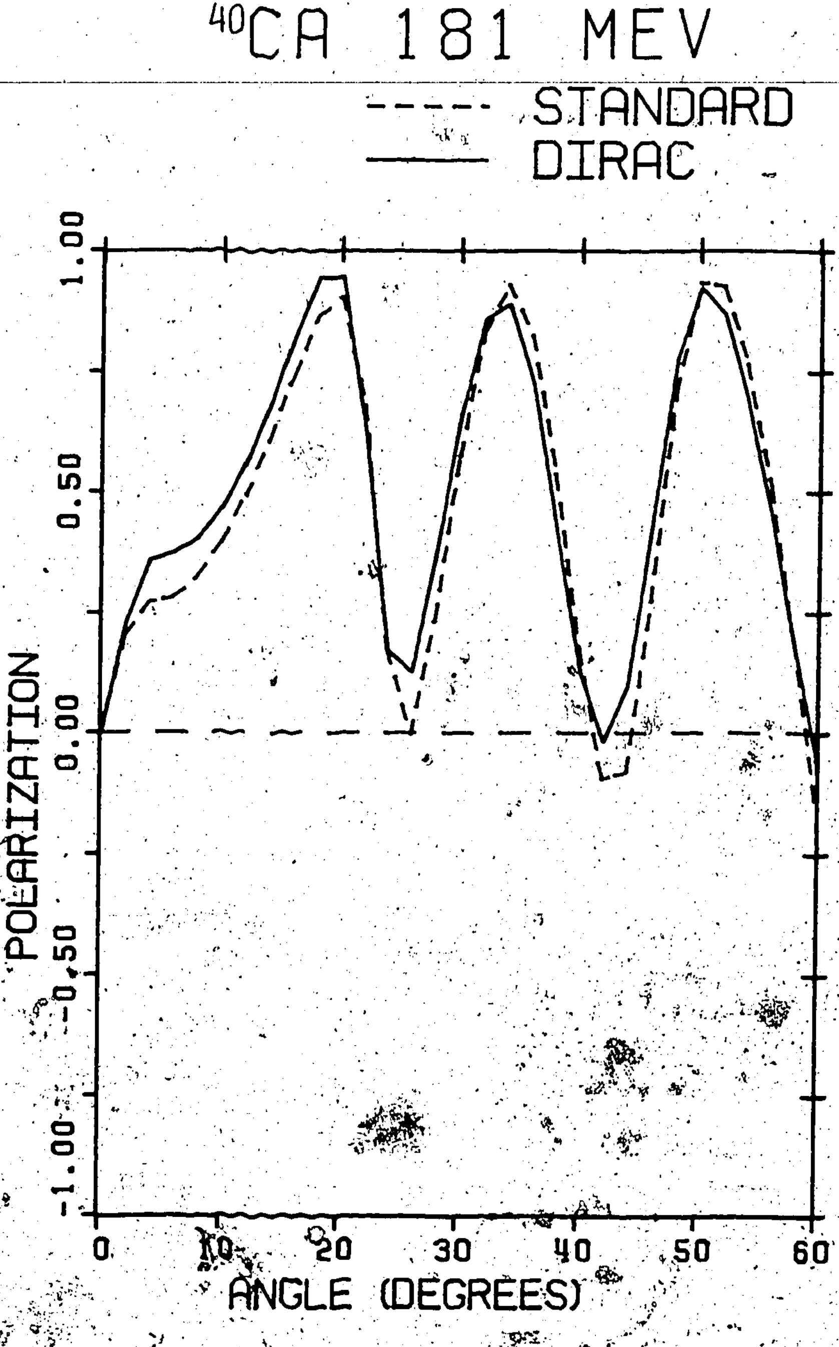

Figure 29 Polarization for P + ^{40}Ca inelastic scattering (2^+ state, E_x = 18 MeV) at E_p = 181 MeV. The solid curve is the DIRAC model and the dashed curve is the STANDARD model.

14.9 mb/sr for the W-S model and 7.9 mb/sr for the WBB model.

VII.9 ^{40}Ca(p,p')^{40}Ca* 3^{-} State (3.73 MeV) at Ep = 300 MeV.

Figures 30 and 31 show the predictions of both models for the inelastic cross-section and polarization. The agreement between the two models is good in cross-section, while large differences appear in polarization, There is no experimental data for this case to test the two models' predictions. It should be mentioned here that the two models do not predict the same elastic scattering, the Dirac model is superior to the Standard model. We believe that the differences in the inelastic scattering relations are due to those of the elastic scattering.

VII.10 ^{40}Ca(p,p')^{40}Ca* 3^{-} State (3.73 MeV) at 500 MeV.

Figures 32 and 33 show the predictions of the two models for both inelastic cross-section and polarization. There are no published experimental data for this specific case but some preliminary experimental data have been made available to us (Se83). At this energy the disagreement between the predictions of the two models is getting larger, particularly for the polarization. It should be mentioned here that the two models do not predict the same elastic scattering at this energy, the Dirac model is superior to the Standard model. We believe that the differences in the predictions of the inelastic scattering observables are a magnification of those of the elastic scattering.

VII.11 ^{208}Pb(p,p')^{209}Pb* 3^{-} State (2.62 MeV) at Ep = 200 MeV.

Figures 34 and 35 show the predictions of the two models for inelastic scattering cross-section and polarization. The experimental data are from (Be81). The two models are in good agreement in the cross-section predictions, while they are in less agreement in the polarization

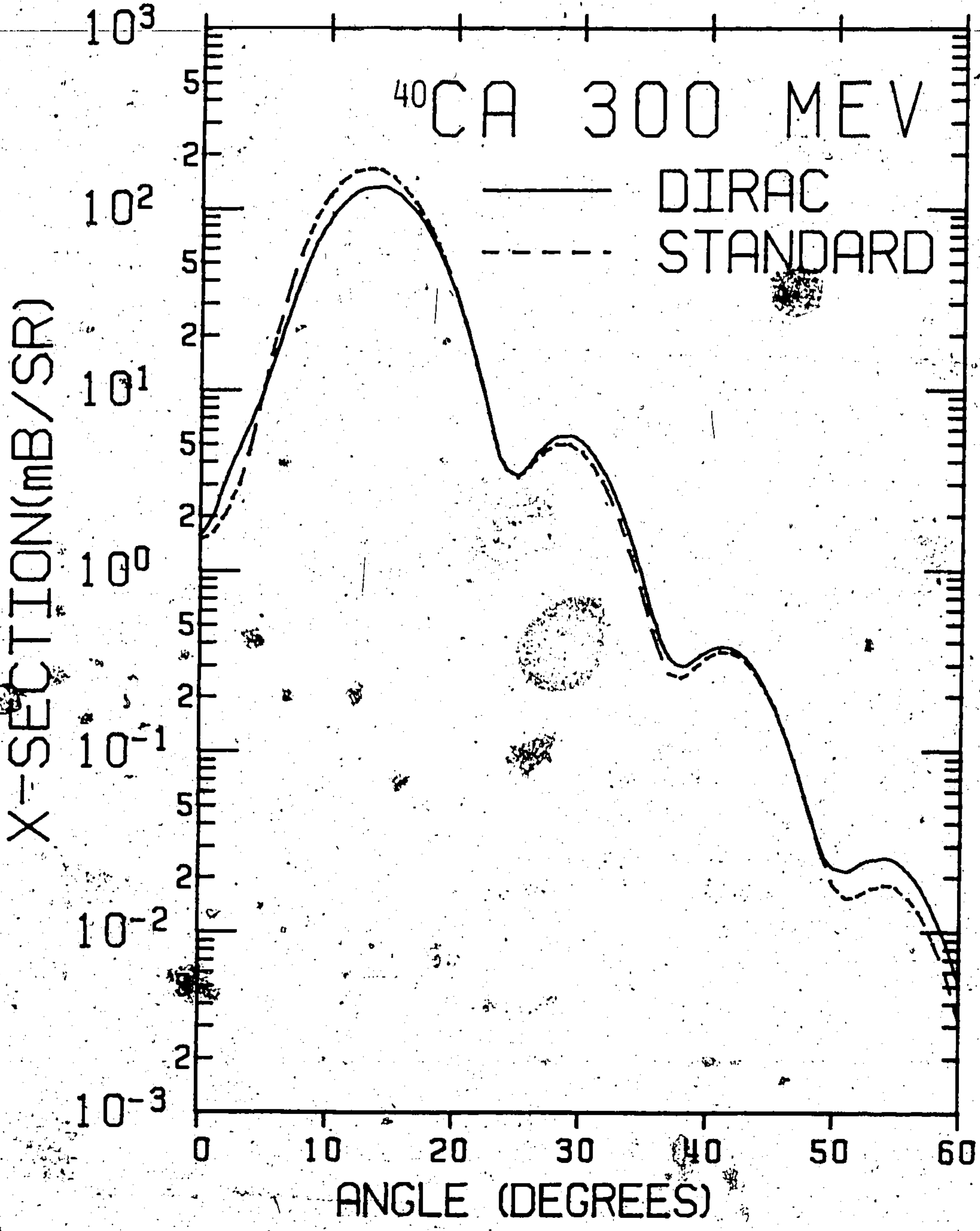

Figure 30 Differential cross-section for P + ^{40}Ca inelastic scattering (3^- state, E_x = 3.73 MeV) at E_p = 300 MeV. The solid curve is the DIRAC model and the dashed curve is the STANDARD model.

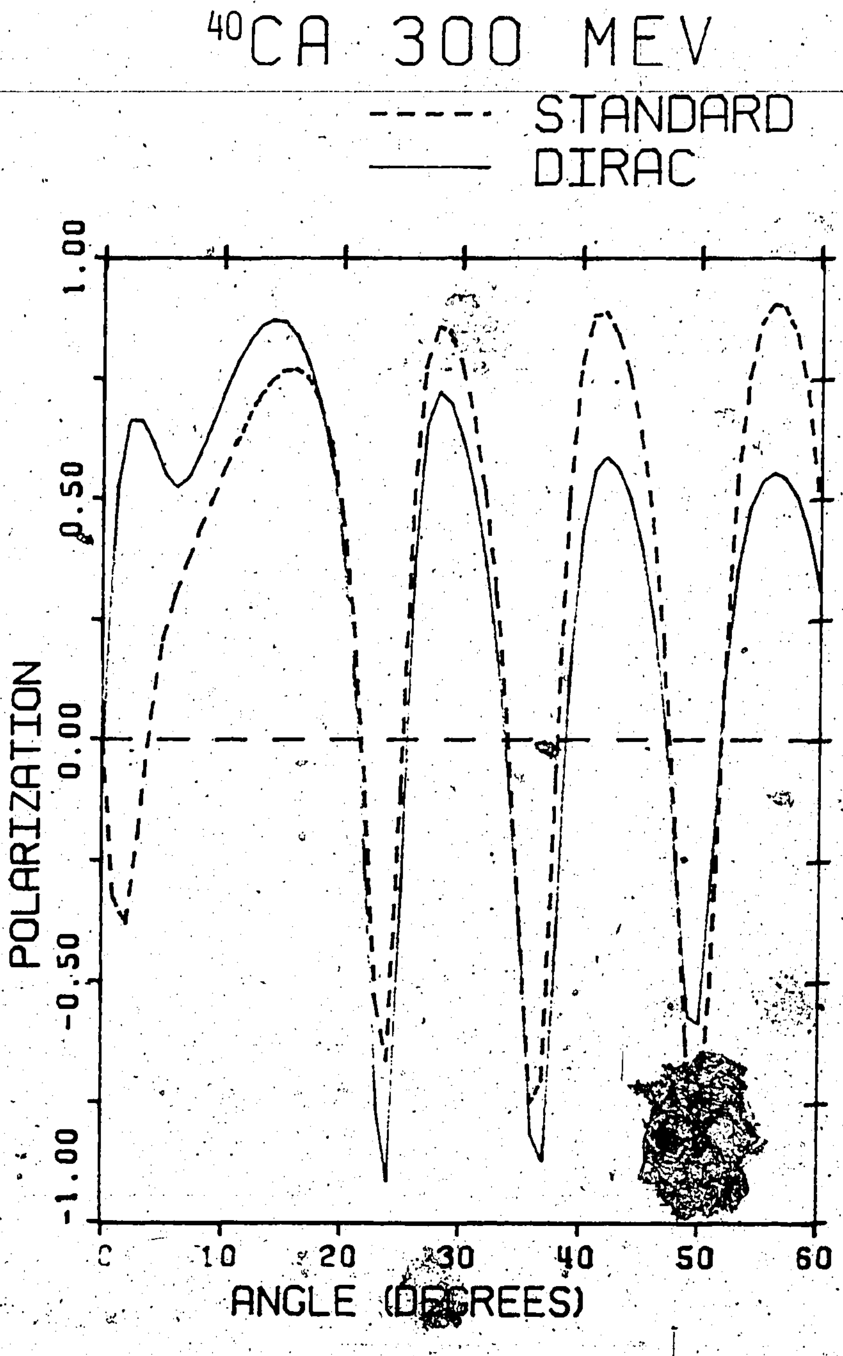

Figure 31 Polarization for P + ^{40}Ca inelastic scattering (3^- state, E_x = 3.73 MeV) at E_p = 300 MeV. The solid curve is the DIRAC model and the dashed curve is the STANDARD model.

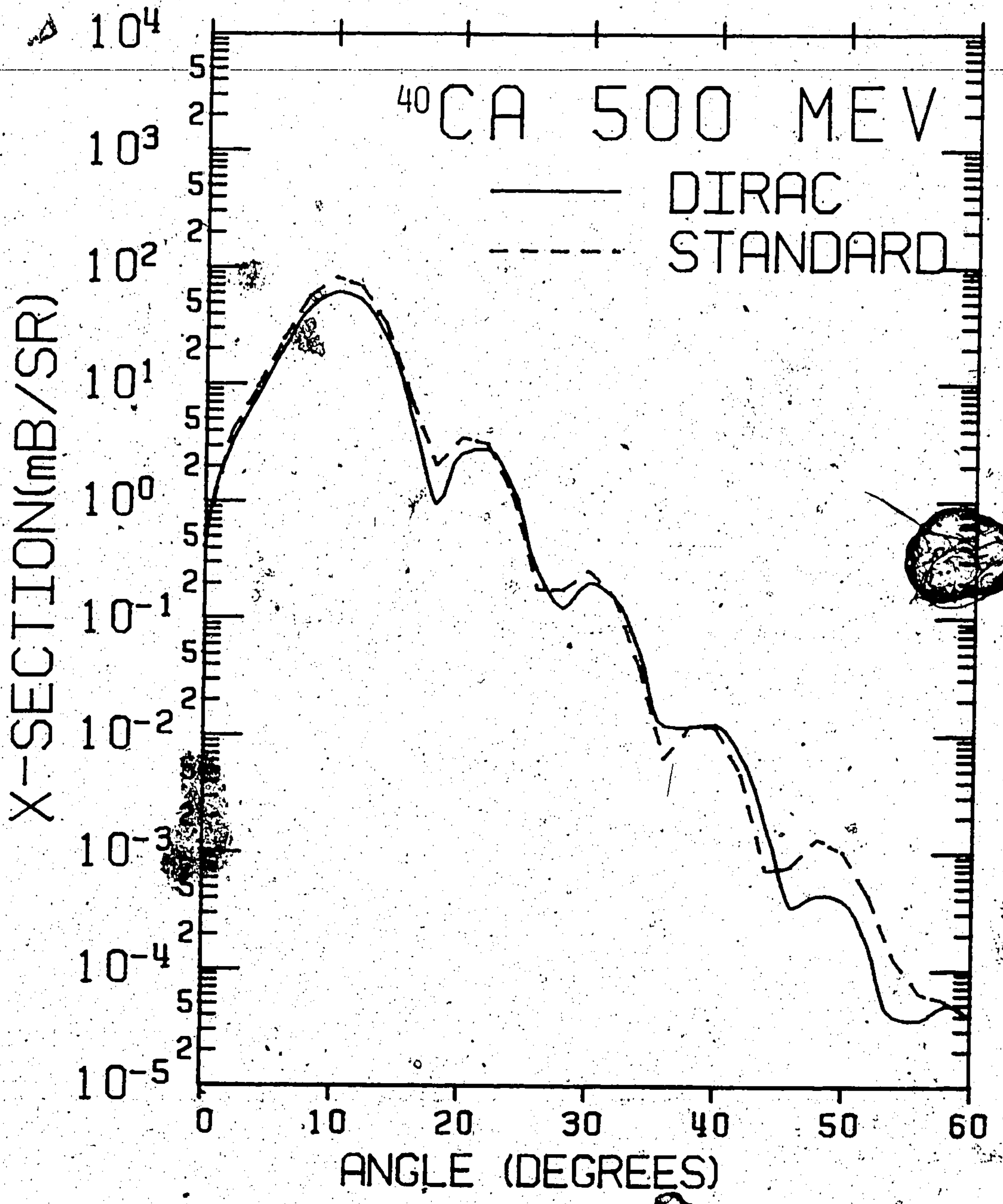

Figure 32 Differential cross-section for P + ^{40}Ca inelastic scattering (3^- state, E_x = 3.73 MeV) at E_p = 500 MeV. The solid curve is the DIRAC model and the dashed curve is the STANDARD model.

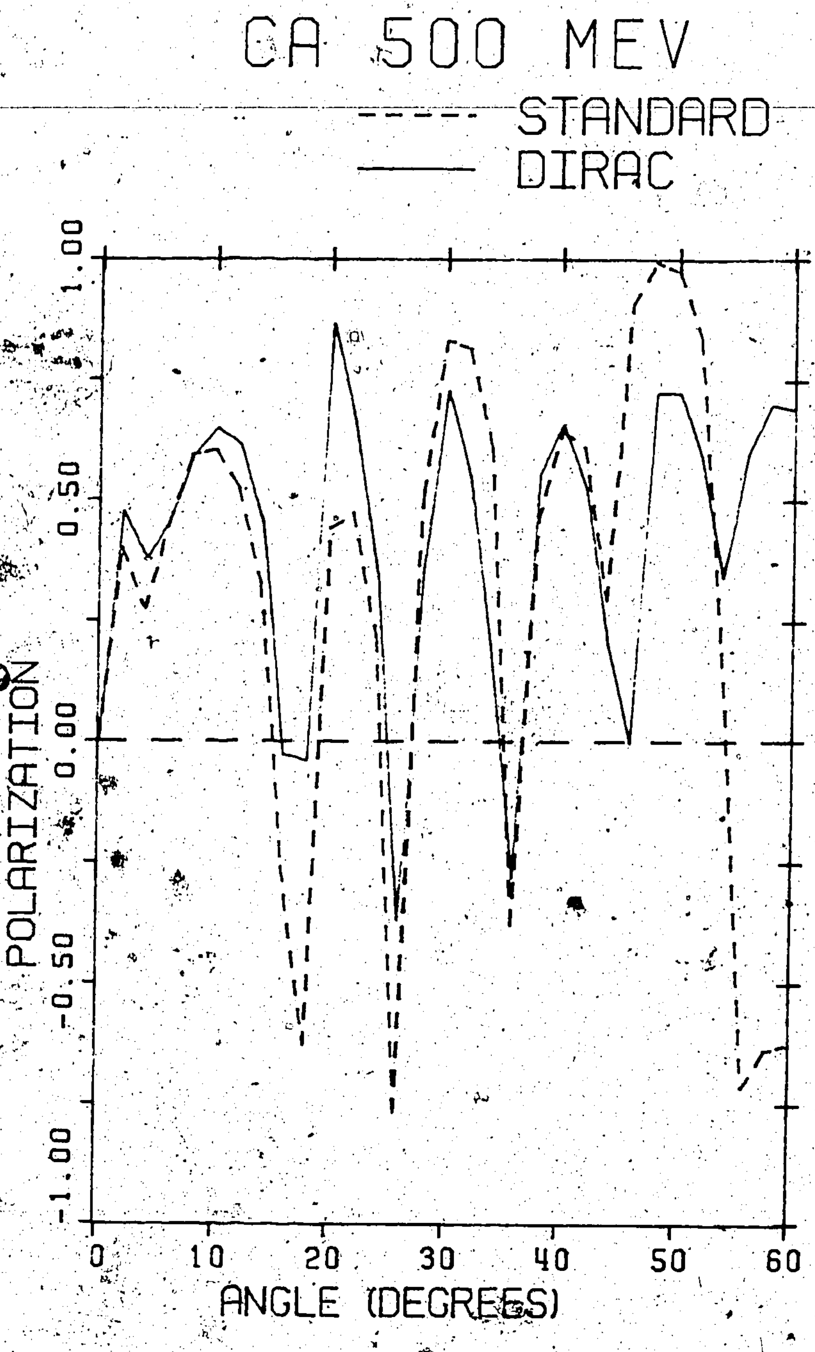

Figure 33 Polarization for P + ^{40}Ca inelastic scattering (3^- state, E_x = 3.73 MeV) at E_p = 500 MeV. The solid curve is the DIRAC model and the dashed curve is the STANDARD model.

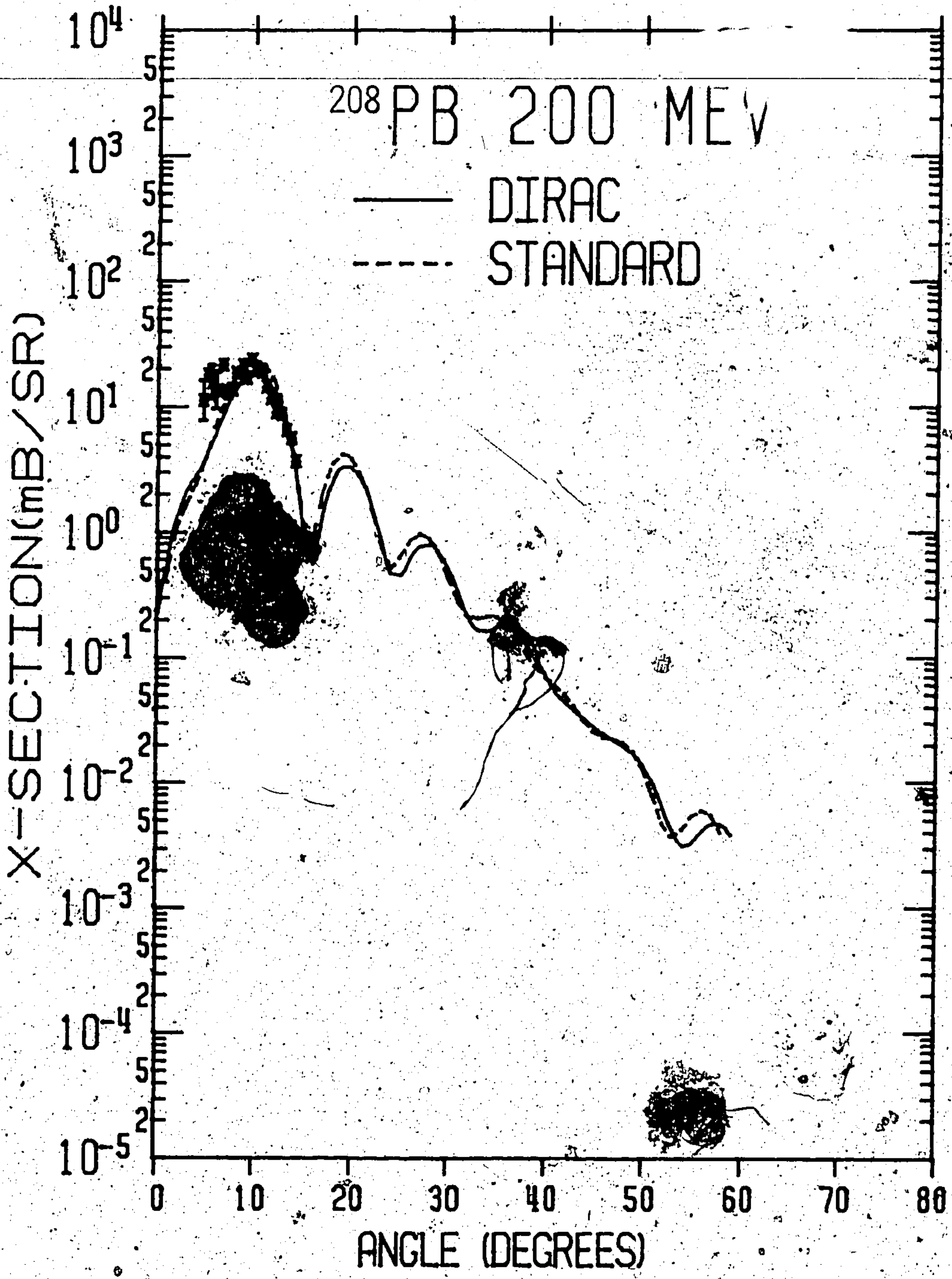

Figure 34 Differential cross-section for P + ^{208}Pb inelastic scattering (2_1^+ state, E_x = 2.62 MeV) at E_p = 200 MeV. The solid curve is the DIRAC model and the dashed curve is the STANDARD model.

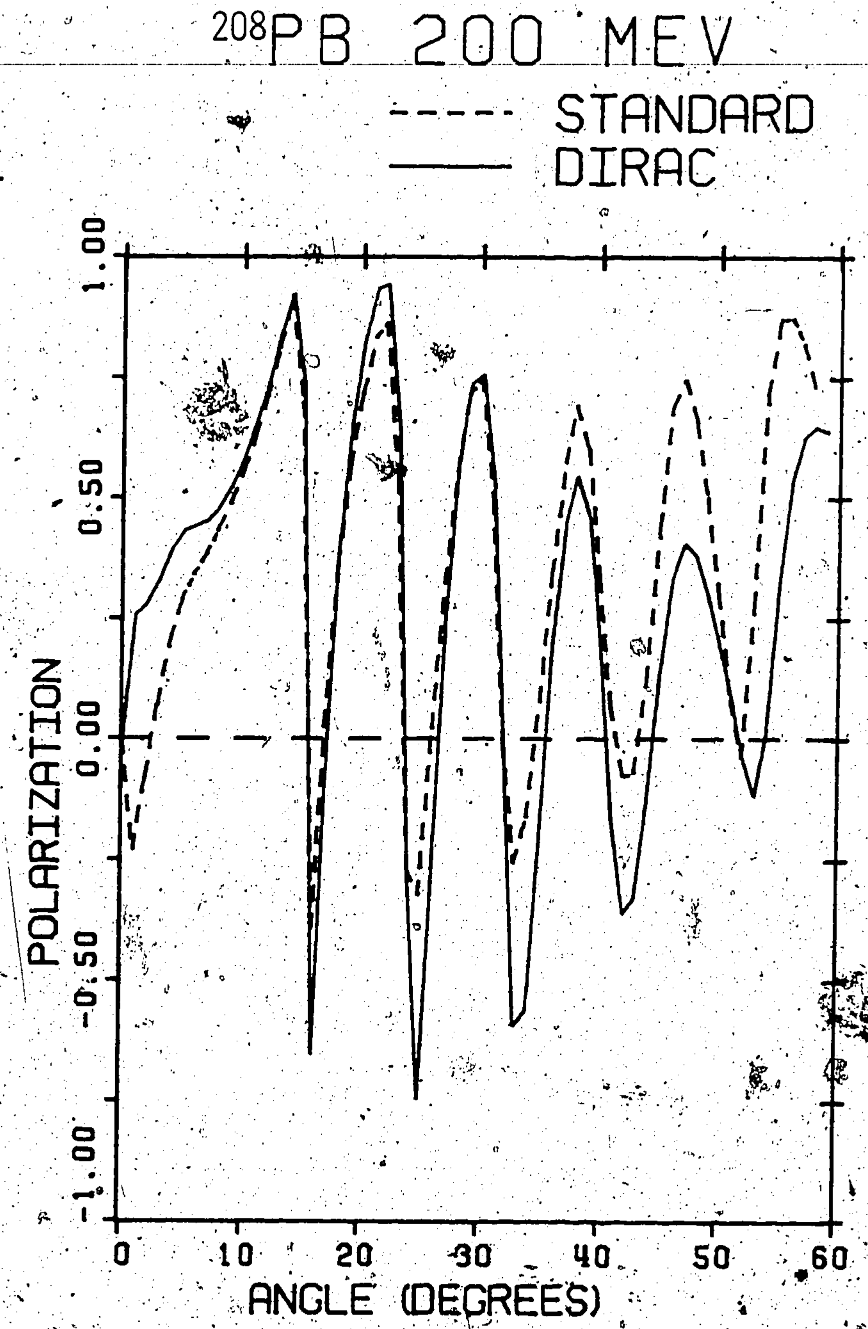

Figure 35 Polarization for P + ^{208}Pb inelastic scattering (2^+ state, E_x = 2.62 MeV) at E_p = 200 MeV. The solid curve is the DIRAC model and the dashed curve is the STANDARD model.

prediction. We used $\beta = 0.095$ for the Standard model and $\beta = 0.1132$ for the Dirac model and $\beta R = 0.745$ F for both models. Satchler (Sa83) used $\beta = 0.116$ in his analysis for both models, and $\beta R = 0.8405$ fm for the W-S model and $\beta R = 0.8027$ fm for the WBB model. He did not include the effect due to the deformed spin-orbit potential which we found is important and necessary. The prediction for peak cross-section is (23.8 mb/sr) for the W-S model, while that of the WBB is 16.70 mb/sr which means that the ratio between the predictions of the two models is 1.425. In our analysis the Standard model predicts a peak cross-section of 23.4 mb/sr while the Dirac model predicts 16.84 mb/sr, this means that the ratio between the predictions of the two models is 1.39. If we do the calculations without including the deformed spin-orbit interaction the Dirac model predicts a peak cross-section of 14.675 mb/sr using the same βR as before, but if we fit the calculations to the experimental data we get $\beta = 0.143$ and $\beta R = 0.94$ F. The shape of the angular distribution will be different, the effect is illustrated in Figure 36. From the above discussion, it is clear that the effect of using the deformed spin dependent interaction is important especially in predicting the shape of the angular distribution (see figure 36). It has less effect in the prediction of the magnitude of the peak cross-section, than the case of 3^- state in ^{40}Ca at Ep = 181 MeV.

The effects of Coulomb deformations for this case have been investigated. We have done the calculations of the Standard model again, but including the deformed Coulomb potential. We have found that the Standard model predicts a peak cross-section of 20.31 mb/sr, which means that the inclusion of the deformed Coulomb potential does reduce the peak cross-section by about 15%. The effects are not large and they

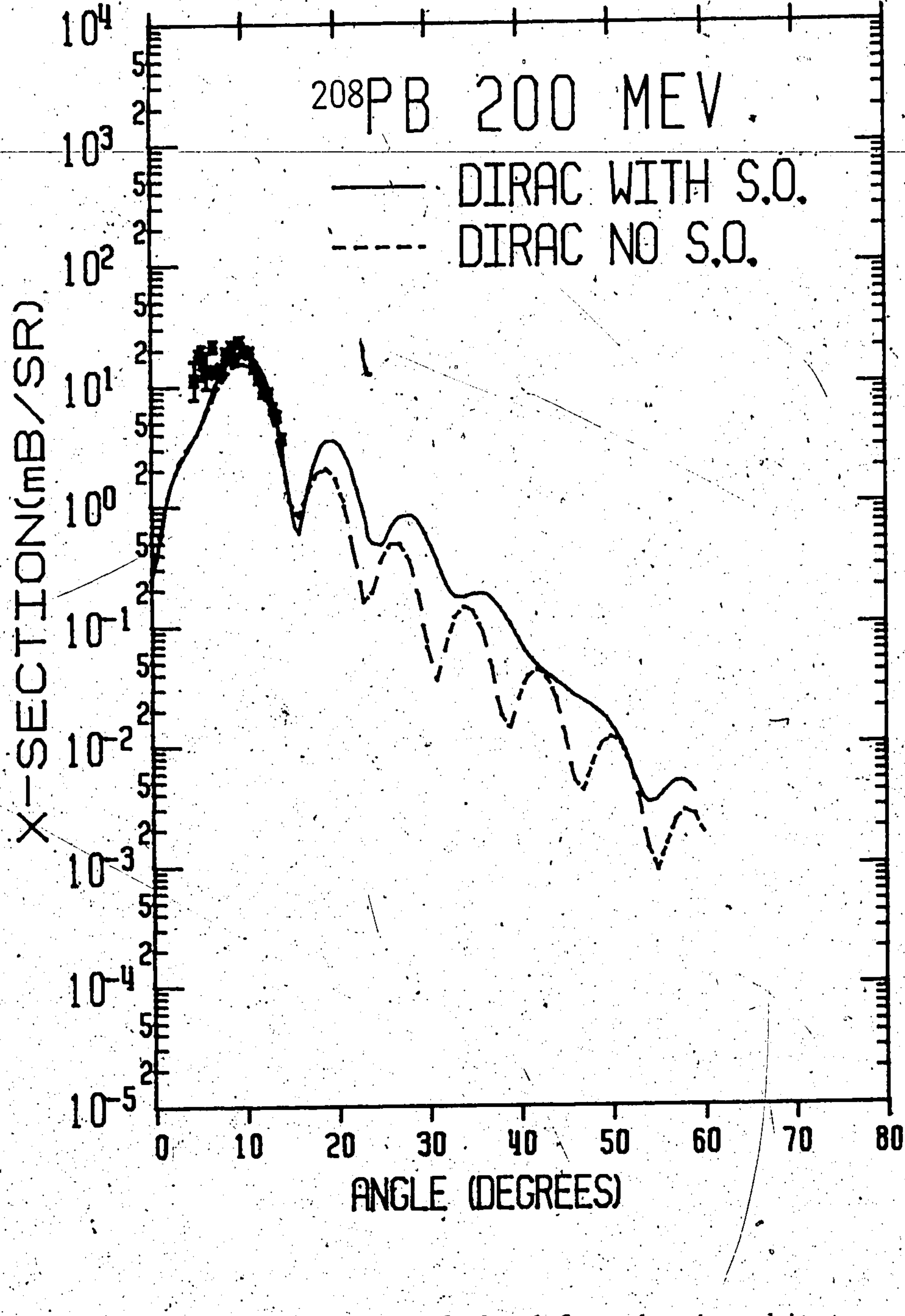

Figure 36 . The effect of the deformed spin orbit term on the calculated cross-section. The calculations are the Dirac model predictions for ^{208}Pb (3^- state, Ex = 2.61 MeV) at Ep = 200 MeV.

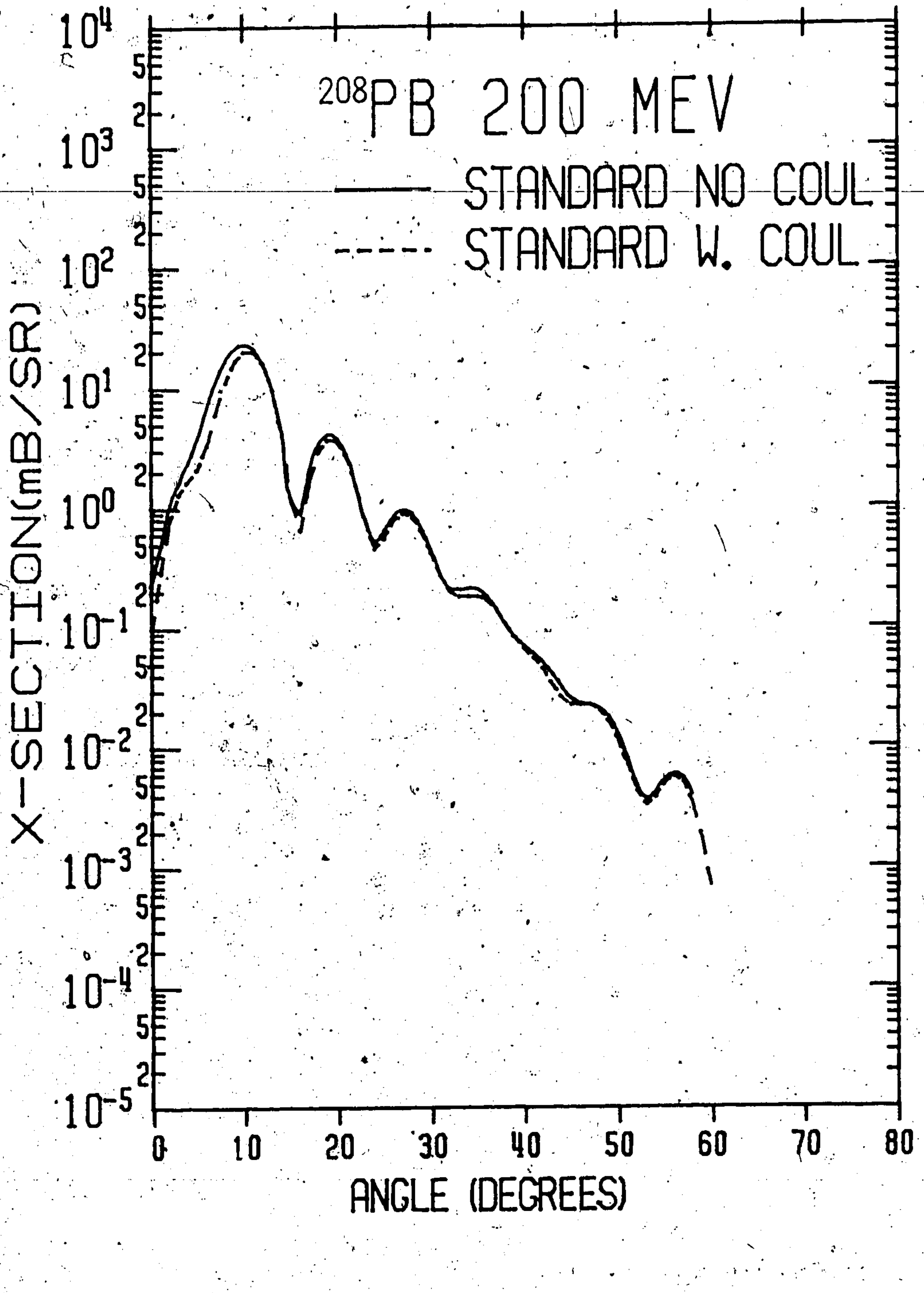

Figure 37 The effect of the deformed Coulomb potential on the calculated cross-section. The calculations are the Standard model predictions for ^{208}Pb (3^- state, Ex = 2.61 MeV) at Ep = 200 MeV.

do not change the shape of the distribution. The effect is illustrated in Figure 37.

Satchler (Sa83) calculates the values of β for some low-lying collective states from electromagnetic transitions, but his values for β were higher than those of the present work. We believe that one of the reasons for this is that Satchler (Sa83) did not include the effects of the deformed spin-orbit interaction in his analysis which we found would require higher β to fit the experimental data. Osterfeld et al. (Os79), in a recent investigation of the hadronic transition operator for inelastic proton scattering from ^{208}Pb (3^- state, Ex = 2.61 MeV), have found that the value of βR calculated by that operator deviates about 24% from that calculated for the electromagnetic transition operator at Ep = 40 MeV, while the deviation reaches about 50% for the same case at Ep = 156 MeV. They also mentioned that the value of βR decreases as the incident projectile energy increases. As we can see from table III, Osterfeld et al. (Os79) obtained these values for $\beta R = 0.899, 0.735, 0.638, 0.474$ F at Ep = 24.55, 40.0, 54.0, 61.25, 156.0 MeV, respectively. Satchler (Sa83) has obtained R = 0.8405, 0.8027 F for the W-S model and the WBB model respectively at Ep = 200 MeV for the same case. In the present work we have obtained a $\beta R = 0.745$ F for both models. Gruhn et al. (Gr72) also noticed the same feature of decreasing βR as projectile energy increases in their analysis of inelastic proton scattering from ^{40}Ca at different projectile energies. They have obtained $\beta R = 1.44, 1.40, 1.32, 1.32$ F for proton inelastic scattering from ^{40}Ca (3^- state; Ex = 3.73 MeV) at Ep = 17, 25, 40, 55 MeV respectively. Sherif (Sh68) obtained $\beta R = 1.187$ F at Ep = 155 MeV for the same case. Satchler (Sa83) got $\beta R = 1.464, 1.398$ F for the W-S and the

TABLE III

THE VALUES OF βR(F) FOR INELASTIC PROTON SCATTERING FROM ^{208}Pb (3^- STATE; Ex = 2.61 MeV)

Ep (MeV)	Osterfeld et al. (Os72)	Satchler (Sa83)	Present Work
24.55	0.899	---	---
40.0	0.725	---	---
54.0	0.732	---	---
61.25	0.638	---	---
156.0	0.474	---	---
200.0	--- ---	0.8405 (W-S) 0.8027 (WBB)	0.745 ---

TABLE IV

THE VALUES OF $\beta R(F)$ FOR INELASTIC PR[illegible]ON SCATTERING FROM ^{40}Ca (3^- STATE; Ex = 3.73 MeV).

Ep. (MeV)	Gruhn et al. (Gr 72)	Sherif (Sh 68)	Satchler (Sa83)	Present work
17.0	1.44	---	---	---
25.0	1.40	---	---	---
40.0	1.32	---	---	---
55.0	1.32	---	---	---
155.0	---	1.187	---	1.058
181.0	--- ---	--- ---	1.464 (W-S) 1.398 (WBB)	1.014 ---

WBB models at $Ep = 181$ MeV respectively. In the present work we have obtained $\beta R = 1.014$ F for both models at $Ep = 181$ MeV.

Finally, we would like to say that the values of βR obtained in the present work do agree with the general behaviour of βR, mentioned in the above discussion, more than those of Satchler (Sa83). Inspite of that, the magnitude of β remains an open question.

VIII. CONCLUSION

The work described in this thesis was done to study both conventional and unconventional optical potential models for proton inelastic scattering. We have carried out comparisons, over a wide range of bombarding energies, between the predictions of two models, namely the Standard model based on Schrödinger equation and the Dirac model based on the reduced Dirac equation, and experimental data whenever available at the same or nearby energy.

We have found in the present work that the deformed spin-dependent interactions in addition to being crucial in the calculation of polarization, are relatively important in the case of cross-section, in the energy region of 155-500 MeV. We have carried out calculations with and without including the deformed spin-dependent interactions in this energy range and we have found that they are important for predicting both the right magnitude for the peak cross-section and the general shape of the experimental data. We also concluded that the kinematics do not crucially affect the results at this energy aside from a slight change in normalization.

We have used equal deformation lengths for the different parts of the potentials throughout this work, and we have found that this is an important and a necessary ingredient for the calculations, because the results obtained for the inelastic polarization are in a better agreement with the data than those using equal deformation parameters (β).

We would like to emphasize here that the change in the shape of the potential does not crucially affect the calculation if all parts of the potential including the spin-dependent part are deformed and included in a full consistent manner, with a necessary constraint that all of these parts have the same deformation length. This is contrary to Satchler's calculation (Sa83), where he found that the ratio between the peak cross-section of Standard to Wine Bottle Bottom models predictions is about 1.5 when equal deformation lengths are used while it is about 2 when equal deformation parameters are used. Our results show that the two models are approximately equivalent in their prediction of the inelastic cross-section at this energy in spite of the fact that the shapes of the real central potentials are quite different inside the nuclear volume. We have also compared the predictions of the two models for the inelastic polarization. Although they differ somewhat they still have the same general shape.

Such accord, however, may not hold as the projectile energy is increased. This would be mainly due to the inability of the Standard model to provide as good a representation of the elastic data as the Dirac model. In other words, the two potentials are not expected to be nearly equivalent except perhaps near 1 GeV bombarding energy where both models yield completely repulsive real central potentials.

The quality of the fits to the angular distribution predicted by the Dirac model is either comparable or slightly in a better agreement with the experimental data to those of the Standard model. The agreement between the two calculations for the inelastic scattering observables depends on that of the elastic scattering. We believe that the differences between the two calculations are somehow a magnification of their differences in fitting the elastic data, which means that the two potentials are not entirely equivalent. Since the Dirac model fits elastic scattering better than the Standard model or at least the same, it is expected to do the same in the inelastic scattering calculation and this is what we conclude from the present study.

REFERENCES

(Ar81) L.G. Arnold, B.C. Clark, R.L. Mercer and F. Schwandt, Phys. Rev. C23 (1981) 1949.

(Ar82) L.G. Arnold, B.C. Clark, E.D. Cooper, H.S. Sherif, D.A. Hutcheon, P. Kitching, J.M. Cameron, R.P. Liljestrand, R.N. MacDonald, W.J. McDonald, C.A. Miller, G.C. Neilson, W.C. Olsen, D.M. Sheppard, G.M. Stinson, D.K. McDaniels, J.R. Tinsley, R.L. Mercer, L.W. Swenson, P. Schwandt and C.E. Stronach, Phys. Rev. C25 (1982) 936.

(Ba62) N. Austern and J.S. Blair, Annals of Physics 33 (1965) 15; R.N. Bassel, G.R. Satchler, R.M. Drisko and E. Rost, Phys. Rev. 128 (1962) 2693.

(Be81) F.E. Bertrand, E.E. Gross, D.J. Horen, J.R. Wu, J.R. Tinsley, C.K. McDaniels, L.W. Swenson and R. Liljestrand, Phys. Lett. 103B (1981) 326.

(Bl64) J.S. Blair in "Nuclear Spectroscopy with Direct Reactions", ANL-6878, (1964).

(Co81) E.D. Cooper, Ph.D. Thesis, University of Alberta (1981) unpublished.

(Co82) E.D. Cooper, H.S. Sherif and J. Johanson, private communication (1982).

(Fe58) H. Feshbach, Ann. Phys. 5 (1958) 357.

(Fr65) M.P. Fricke and G.R. Stachler, Phys. Rev. 139 (1955) B567.

(Fr67) M.P. Fricke, E.E. Gross and A. Zucker, Phys. Rev. 163 (1967) 1153.

(Fu36) W.H. Furry, Phys. Rev. 50 (1936) 784.

(FU68) S.A. Fulling and G.R. Satchler, Nucl. Phys. A111 (1968) 81.

(Gr72) G.R. Gruhn, T.Y.T. Kno, C.J. Maggiore, H. McManus, F. Petrovich and B.M. Preedom, Phys. Rev. C6 (1972) 915.

(Ha66) R.M. Haybron and H. McManus, Phys. Rev. 140 (1965) B638.

(Ho63) W.J. Hornyak, J.C. Jacqmart, M. Rou, J.P. Garron and M. Liu, J. Phys. 24 (1963) 1052.

(Hu59) M. Hull and G. Breit, Encyclopedia of Physics 41, edited by S. Flugge (Springer-Verlag, Berlin, 1959).

(In71) A. Ingemarsson and J. Kallne, Physica Scripta 2 (1971) 191.

(Ja70) D.F. Jackson, Nuclear Reactions, Methuen and Co. LTd. (1970).

(Ja79) M. Jaminon, C. Mahaux and P. Rochus, Phys. Rev. Lett. 43 (1979) 1097.

(Ja80) M. Jaminon, C. Mahaux and P. Rochus, Phys. Rev. C22 (1980) 2027.

(Me81) H.P. Meyer, P. Schwandt, G.L. Moake and P.P. Singh, Phys. Rev. C23 (1981) 616.

(Na81) A. Nadaseen, P. Schwandt, P.P. Singh, W.W. Jacobs, A.D. Bacher, P.T. Devevec, M.D. Kaitchuch and J.T. Meek, Phys. Rev. C23 (1981) 1023.

(Os79) F. Osterfeld, J. Wambach and H. Lenske, Nucl. Phys. A318 (1979) 45.

(Ra69) J. Rayanal, Magali (1969) private communication.

(Ro61) M.E. Rose, Elementary Theory of Angular Momentum, J. Wiley and Sons, Inc. (1961).

(Sa65) G.R. Satchler, Lectures in Theoretical Physics, University of Colorado Press (1965).

(Sa83) G.R. Satchler, Nucl. Phys. A394 (1983) 349.

(Se83) K. Seth, (1983) private communication.

(Sh69) H.S. Sherif, Ph.D. Thesis, University of Washington (1968) unpublished.

(Sh68a) H.S. Sherif and J.S. Blair, Phys. Lett. 26B (1968) 489.

(Sh69) H.S. Sherif, Nucl. Phys. A131 (1969) 532.

(Sh71) H.S. Sherif, Can. J. Phys. 49 (1971) 983.

(Va74) W.T.H. Van Oers, H. Haw, N.E. Davison, A. Ingemarsson, B. Fagerstrom and G. Tibell, Phys. Rev. C10 (1974) 307.

(Wi68) A. Willis, B. Geoffrion, N. Marty, M. Moret, C. Rolland and B. Tatischeff, Nucl. Phys. A112 (1968) 417.

(Wo68) L. Wolfenstein, Ann. Rev. Nucl. Sci. 6 (1956) 43.